

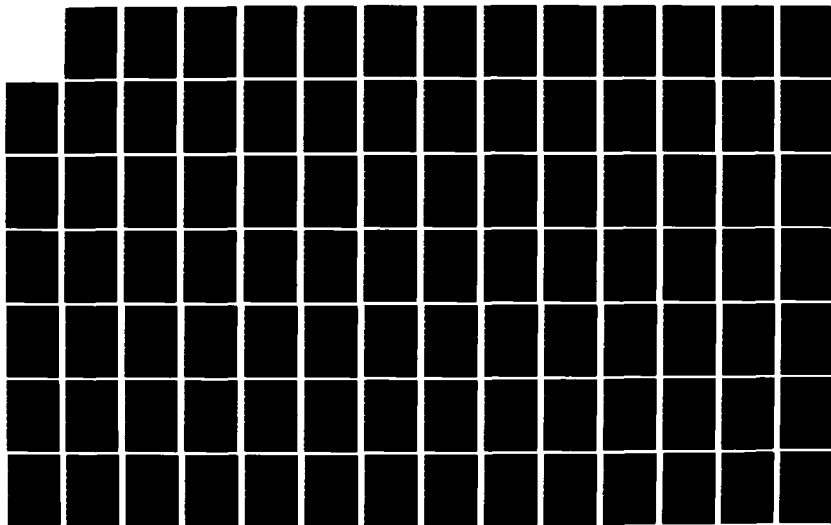
AD-A127 455

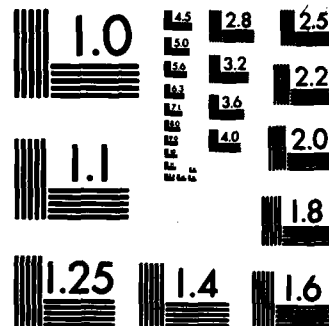
STATUS REPORT ON PREPARATION OF A REVISED LONGHAYE  
COMMUNICATION LINK VUL. (U) KAMAN TEMPO SANTA BARBARA  
CA R R RUTHERFORD ET AL. 01 OCT 81 KT-81-022(R)  
DNA-5879T DNA001-80-C-0098

1/2

UNCLASSIFIED

F/G 20/14 NL





MICROCOPY RESOLUTION TEST CHART  
NATIONAL BUREAU OF STANDARDS-1963-A

AD-E 301085

AD A127455

DNA 5879T

# STATUS REPORT ON PREPARATION OF A REVISED LONGWAVE COMMUNICATION LINK VULNERABILITY CODE

Kaman Tempo  
816 State Street  
Santa Barbara, California 93102

1 October 1981

Topical Report for Period 2 February 1981-31 January 1982

CONTRACT No. DNA 001-80-C-0098

APPROVED FOR PUBLIC RELEASE;  
DISTRIBUTION UNLIMITED.

THIS WORK WAS SPONSORED BY THE DEFENSE NUCLEAR AGENCY  
UNDER RDT&E RMSS CODE B322081466 S99QAXHC00025 H2590D.

Prepared for  
Director  
DEFENSE NUCLEAR AGENCY  
Washington, DC 20305

DTIC FILE COPY

88 03 11 004

Destroy this report when it is no longer  
needed. Do not return to sender.

PLEASE NOTIFY THE DEFENSE NUCLEAR AGENCY,  
ATTN: STTI, WASHINGTON, D.C. 20305, IF  
YOUR ADDRESS IS INCORRECT, IF YOU WISH TO  
BE DELETED FROM THE DISTRIBUTION LIST, OR  
IF THE ADDRESSEE IS NO LONGER EMPLOYED BY  
YOUR ORGANIZATION.



UNCLASSIFIED

SECURITY CLASSIFICATION OF THIS PAGE (When Data Entered)

REPORT DOCUMENTATION PAGE		READ INSTRUCTIONS BEFORE COMPLETING FORM
1. REPORT NUMBER DNA 5879T	2. GOVT ACCESSION NO. DA A127 455	3. RECIPIENT'S CATALOG NUMBER
4. TITLE (and Subtitle)  STATUS REPORT ON PREPARATION OF A REVISED LONGWAVE COMMUNICATION LINK VULNERABILITY CODE		5. TYPE OF REPORT & PERIOD COVERED Topical Report for Period 2 Feb 81 - 31 Jan 82
		6. PERFORMING ORG. REPORT NUMBER KT-81-022(R)
7. AUTHOR(s) R.R. Rutherford W.S. Knapp		8. CONTRACT OR GRANT NUMBER(s)  DNA 001-80-C-0098
9. PERFORMING ORGANIZATION NAME AND ADDRESS Kaman Tempo 816 State Street Santa Barbara, CA 93102		10. PROGRAM ELEMENT, PROJECT, TASK AREA & WORK UNIT NUMBERS  Subtask S99QAXHC000-25
11. CONTROLLING OFFICE NAME AND ADDRESS Director Defense Nuclear Agency Washington, DC 20305		12. REPORT DATE 1 October 1981
		13. NUMBER OF PAGES 98
14. MONITORING AGENCY NAME & ADDRESS (if different from Controlling Office)		15. SECURITY CLASS. (of this report)  UNCLASSIFIED
		15a. DECLASSIFICATION/DOWNGRADING SCHEDULE N/A since UNCLASSIFIED
16. DISTRIBUTION STATEMENT (of this Report)  Approved for public release; distribution unlimited.		
17. DISTRIBUTION STATEMENT (of the abstract entered in Block 20, if different from Report)		
18. SUPPLEMENTARY NOTES  This work was sponsored by the Defense Nuclear Agency under RDT&E RMSS Code B322081466 S99QAXHC00025 H2590D.		
19. KEY WORDS (Continue on reverse side if necessary and identify by block number) Longwave Propagation      Nuclear Weapon Effects ELF Propagation              Computer Codes VLF Propagation LF Propagation		
20. ABSTRACT (Continue on reverse side if necessary and identify by block number)  This report describes work on the WEDCOM IV code propagation models in order to reduce computation times. The work includes adaption of an ELF propagation model developed by H.G. Booker, revision of the reflection coefficient model used for VLF and LF propagation, and development of a revised mode search model for VLF propagation.		

DD FORM 1 JAN 73 1473

EDITION OF 1 NOV 65 IS OBSOLETE

UNCLASSIFIED

SECURITY CLASSIFICATION OF THIS PAGE (When Data Entered)

# TABLE OF CONTENTS

<u>Section</u>	<u>Page</u>
LIST OF ILLUSTRATIONS	3
LIST OF TABLES	6
1 INTRODUCTION	7
1.1 BACKGROUND INFORMATION AND HISTORY OF THE WEDCOM CODE	7
1.2 LIMITATIONS AND DEFICIENCIES OF WEDCOM IV	9
2 LF MODEL IMPROVEMENTS	11
2.1 INTRODUCTION	11
2.2 LF MODEL FORMULATION	12
2.3 WORLD SURFACE CONDUCTIVITY	14
2.4 SKYWAVE	15
2.5 GROUNDWAVE	20
2.6 EARTH SURFACE DIFFRACTION, REFLECTION	23
2.7 TROPOSPHERIC REFRACTION	30
2.8 CONVERGENCE FACTOR	31
3 IONOSPHERIC REFLECTION ALTITUDE AND REFLECTION COEFFICIENT MODELS	33
3.1 INTRODUCTION	33
3.2 REFLECTION ALTITUDE	35
3.3 COMPUTATION CRITERIA FOR ADJACENT VERTICAL IONOSPHERIC PROFILES	39
3.4 INTERPOLATION ALGORITHM	41
4 VLF MODEL IMPROVEMENTS	54
4.1 INTRODUCTION	54
4.2 PROCEDURE TO REDUCE THE NUMBER OF REFLECTION COEFFICIENT COMPUTATIONS	55
4.3 PRECOMPUTED EIGENANGLES	56
4.4 EIGENANGLE DETERMINATION USING ANALYTIC REFLECTION COEFFICIENT FORMULATION AND INITIAL EIGENANGLE ESTIMATES	57
4.4.1 Quasi-Flat Earth Modes	57
4.4.2 Earth-Grazing Modes	57
4.4.3 Whispering-Gallery Modes	58
5 ELF PROPAGATION MODEL	61
5.1 GENERAL	61
5.2 BOOKER MODEL	62



Accession No.	
NTIS Grant	
DTIC No.	
Author	
Editor	
Reviewer	
Special	

1

## TABLE OF CONTENTS (Concluded)

<u>Section</u>	<u>Page</u>
5.2.1 Evaluate the Heights of Reflection	62
5.2.2 Calculate the Complex Index of Refraction Indices at the Reflection Heights	64
5.2.3 Calculate the Complex Elliptical Polarization at the Reflection Heights	65
5.2.4 Calculate the Equivalent Complex Heights of Reflection	65
5.2.5 Calculate the Equivalent Complex Height of the Bottom of the Ionosphere	68
5.2.6 Calculate the Phase Velocity and Attenuation Rate	68
5.2.7 Interpolation and Calculation of Derivatives	69
5.3 EVALUATION OF BOOKER MODEL	71
5.3.1 Comparison with Results Presented by Booker and Behroozi-Toasi	71
5.3.2 Comparison with Selected NOSC Results	71
5.4 CALCULATION OF EXCITATION AND HEIGHT-GAIN FACTORS	71
6 CODE STRUCTURE	84
REFERENCES	89

## LIST OF ILLUSTRATIONS

<u>Figure</u>		<u>Page</u>
1	Illustration of LF ground and ionospheric path segmentation.	13
2	Conductivity prediction as a function of the parameter $\gamma$ for Subroutine CONMAP used in WEDCOM IV.	16
3	Illustrating the possible single ionospheric reflection ray-path geometry.	17
4	Range along propagation paths as a function of elevation angle (at XMTR) for XMTR and RCVR antenna altitudes at 6 km.	19
5	Illustration of Eckersley's procedure.	21
6	Illustrating how the geometric-optic region ray paths, a and b, converge in the diffraction region.	24
7	Comparison of geometric-optic and diffraction models of foreground factor in caustic region for ionosphere-to-ionosphere ( $H_R = 80$ km), sea water, and vertical polarization.	25
8	Comparison of geometric-optic and diffraction models of foreground factor in caustic region for ionosphere-to-ionosphere ( $H_R = 80$ km), sea water, and horizontal polarization.	26
9	Comparison of geometric-optic and diffraction models of foreground factor in caustic region for ionosphere-to-ionosphere ( $H_R = 80$ km), land, and horizontal polarization.	26
10	Comparison of geometric-optic and diffraction models of foreground factor in caustic region for ionosphere-to-ionosphere ( $H_R = 80$ km), land, and horizontal polarization.	27
11	Comparison of geometric-optics and diffraction models of foreground factor in caustic region for ionosphere-to-antenna case ( $H_R = 80$ km, antenna altitude = 0.0 km), land, and vertical polarization.	28
12	Comparison of geometric-optics and diffraction models of foreground factor in caustic region for ionosphere-to-antenna case ( $H_R = 80$ km, antenna altitude = 0.0 km), land, and horizontal polarization.	28
13	Comparison of geometric optics and diffraction models of foreground factor in caustic region for ionosphere-to-antenna case ( $H_R = 80$ km, antenna altitude = 10 km), land, and vertical polarization.	29



# LIST OF ILLUSTRATIONS (Continued)

<u>Figure</u>		<u>Page</u>
14	Comparison of geometric optics and diffraction models of foreground factor in caustic region for ionosphere-to-antenna case ( $H_p = 80$ km, antenna altitude = 10 km), land, and horizontal polarization.	29
15	Convergence coefficient sensitivity to reflection altitude.	32
16	H-field component magnitudes and Poynting vector components in vertical direction for normal nighttime conditions, for 40 kHz and $\theta_i = 80^\circ$ .	36
17	H-field component magnitudes and Poynting vector components in vertical direction for strong gamma nuclear disturbance, for 40 kHz and $\theta_i = 80^\circ$ .	37
18	Comparison of analytic reflection altitude ( $H_p$ ), corrected ( $H_{pc}$ ), and altitude region where effective altitude should be selected for 40 kHz, $\theta_i = 80^\circ$ , and for the range away from a high-altitude burst where gamma deposition is dominate.	38
19	Magnetic field and ionospheric profile sensitivities of $Im(q)$ for frequency = 40 kHz.	42
20	Magnitude of „R„ sensitivity to magnetic field for normal nighttime and frequency = 100 kHz.	43
21	Magnitude of „R„ sensitivity to magnetic field for moderate spread debris case for frequency = 100 kHz.	44
22	Reflection coefficients for normal nighttime as a function of $\theta_i$ .	46
23	Magnitude of „R„ and ${}_1R_1$ for a normal night, dip = $70^\circ$ , and frequency = 27 kHz.	47
24	Phase of „R„ and ${}_1R_1$ for normal night, dip = $70^\circ$ , and frequency = 27 kHz.	48
25	Magnitude of „R„ and ${}_1R_1$ for normal night, dip = $30^\circ$ , and frequency = 27 kHz.	49
26	Magnitude of „R„ and ${}_1R_1$ for normal night, dip = $70^\circ$ , and frequency = 40 kHz.	50
27	Magnitude of „R„ and ${}_1R_1$ for a moderate spread debris case for dip = $70^\circ$ , frequency = 40 kHz.	51
28	Comparison of new and WEDCOM IV procedures for determining $\theta$ -plane reflection coefficient computations.	56

# LIST OF ILLUSTRATIONS (Concluded)

<u>Figure</u>		<u>Page</u>
29	Loci of eigenangles for the approximate isotropic and exact anisotropic procedures.	59
30	Illustrating the variation of the velocity of phase propagation with latitude and frequency under daytime conditions.	72
31	Illustrating the variation of the rate of attenuation with latitude and frequency under daytime conditions.	73
32	Illustrating the variation of the velocity of phase propagation with latitude and frequency under nighttime conditions.	74
33	Illustrating the variation of the rate of attenuation with latitude and frequency under nighttime conditions.	75
34	Simplified ionospheric dependent propagation flow diagrams for LOS and ionospheric dependent propagation ionization models.	87

## LIST OF TABLES

<u>Table</u>		<u>Page</u>
1	Foreground factors for geometric optic ray-paths (nondiffracted).	18
2	Matrix of cases exercised by the geometric-optics and dif- fraction models.	25
3	Parameters varied in q and ionospheric reflection coefficient calculations to obtain $\delta_q$ .	41
4	Ionization and collision frequencies for WEDCOM quiet nighttime ionosphere.	76
5	Ionization and collision frequencies for NOSC quiet nighttime ionosphere.	77
6	Ionization and collision frequencies for WEDCOM quiet daytime ionosphere.	78
7	Ionization and collision frequencies for NOSC quiet daytime ionosphere.	79
8	Ionization and collision frequencies for moderate nuclear ionization.	80
9	Comparison of attenuation rate and phase velocity from NOSC and Booker models, 75 Hz.	81
10	Comparison of attenuation rate and phase velocity from NOSC and Booker models, 150 Hz.	81
11	Comparison of excitation and height gain factors from full wave (first entry) and approximate (second entry) models, 150 Hz.	83
12	Comparison of excitation and height-gain factors from full wave model (first entry) and approximate (second entry) models, 75 Hz.	83

## SECTION 1

### INTRODUCTION

The WEDCOM code (Weapon Effects on D-region COMmunications) is a digital computer program that provides calculations of ELF, VLF, and LF electric and magnetic field strengths in ambient and nuclear disturbed environments (Reference 1). The code is intended for use when a relatively detailed analysis of the propagation between two terminals is required in nuclear disturbed environments. The computational models (particularly the nuclear environment models) are intermediate between first principle and simplified simulation models. Most physical quantities are explicitly modeled. This report describes work on code structure and propagation models in order to reduce link evaluation times.

#### 1.1 BACKGROUND INFORMATION AND HISTORY OF THE WEDCOM CODE

Propagation at frequencies in the VLF (3 to 30 kHz) and LF (30 to 300 kHz) bands is essentially controlled by the D region of the ionosphere. Propagation in the ELF\* band can extend into the E and F regions. Nuclear weapon effects on propagation results from ionization produced by the detonation. Usually the effects are caused by free electrons, but significant absorption may result from ions produced in the lower part of the D region.

Computer codes have been developed by the Department of Commerce (Office of Telecommunications), the Department of the Navy (Naval Ocean Systems Center), and others to calculate ELF, VLF, and LF propagation for both natural and disturbed conditions. Generally, these codes require electron and ion density profiles as input and perform numerical solutions for either a mode or ray-hop sum to obtain the electric field strength. The several codes are characterized by whether or not they include the geomagnetic field, the method used to include earth's curvature, and the numerical methods used. An important assumption often used in the calculational models is that the ionosphere is horizontally stratified (or at most only slowly varying between transmitter and receiver terminals).

---

\* In this document the ELF band is defined as 3 to 300 Hz.

The WEDCOM code was originally developed to combine nuclear environments and VLF and LF propagation models in a single computer program. The first version was distributed in March 1969 and provided calculations for propagation between vertically polarized, ground-based antennas. Input requirements (weapon and propagation parameters) were those generally available for propagation studies, but were made sufficiently flexible so that the code could be used in nuclear test planning, data analysis, and sensitivity studies. In addition to outputs required to evaluate received field strengths, ionization and propagation details were provided as an option.

In 1970 a second version of the code (designated WEDCOM MB) was prepared for use in calculating effects of multiple bursts. In addition, ground conductivity was made an input and improvements in the reflection coefficient calculations were made. In 1972 a third version of the code (designated WEDCOM III) was prepared to include calculations of VLF horizontally polarized waves and to include VLF height-gain factors for elevated transmitter and receiver terminals. In addition, improvements in the ionization models and code structure were made.

The current version of the WEDCOM code, designated WEDCOM IV, was prepared in 1980 to incorporate improved environment models, improved VLF and LF propagation models, and to incorporate a model for ELF propagation. The major changes to environment models were:

1. Modification of D-region chemistry to include effect of cluster ions.
2. Modification of high-altitude burst phenomenology affecting early-time (minutes) debris location.
3. Addition of an atmospheric wind model affecting late-time (hours) debris location.
4. Addition of new prompt ionization sources affecting E- and lower F-region ionization.

The VLF and LF propagation models were improved as follows:

1. Replacement of the plane-slab isotropic ionosphere with an anisotropic ionosphere with earth curvature.
2. Provision for modeling ground conductivity and permittivity as a function of location.
3. Provision for elevated and arbitrarily oriented antennas in the LF band.

4. Addition of a new mode search model in the VLF band to insure obtaining important modes.
5. Addition of a mode conversion program in the VLF band.

## 1.2 LIMITATIONS AND DEFICIENCIES OF WEDCOM IV

The major limitations and deficiencies of WEDCOM IV identified by users include:

1. Link evaluation times are too long. While the propagation models used are faster running than the detailed models developed by NOSC, they still require too much evaluation time for typical user requirements.
2. Signal variance and statistics are not given.
3. Signal processing models that provide either bit error rates or message error rates are not given.
4. The ambient ionosphere models are not consistent with those used by NOSC or the Office of Telecommunications (which also differ).
5. Ambient noise models are not provided and procedures for determining the effect of nuclear environments on received noise are not included.
6. Signal-to-jamming analysis capability is not included.
7. Code structure and input and output design is not optimized for system analysis.

As noted above the WEDCOM IV link evaluation times are significantly longer than for previous versions of the code. The longer running times are due to including anisotropy, mode search and mode conversion models, and an improved reflection coefficient model. The longer running times limit use of the code in studies of environment, propagation, and system parameters. Methods for reducing link evaluation times are discussed in Sections 2 through 6. A new interpolation procedure for evaluating VLF and LF reflection coefficients is described that reduces computation time while still providing acceptable accuracy. A new VLF mode search model is described that is faster running than the current model and may provide significant improvements in running time for undisturbed or slightly disturbed conditions. Other model improvements that can be included in WEDCOM are also described in Sections 2 through 4.

A new ELF propagation model developed at the University of California, San Diego by H.G. Booker that requires much less computation time than the current WEDCOM model is described in Section 5.

Some reduction in computation time and improvements in input and output formats can be obtained by changes in code structure. Code structure considerations are discussed in Section 6.

The deficiencies described in items 2 through 4 have been studied by DNA contractors and models are available that can be included in a WEDCOM revision. The deficiencies in items 5 through 7 are largely due to WEDCOM being a single-link code and are best corrected in a multilink, multiburst simulation code (eg, SIMBAL).

## SECTION 2

### LF MODEL IMPROVEMENTS

#### 2.1 INTRODUCTION

The WEDCOM IV LF propagation model was revised for use in studies for the Naval Electronic Systems Command (Reference 2). The revision was necessitated by task requirements involving high (MF) system frequencies, and balloon borne antennas. The model improvements were concerned with:

- A more efficient and simpler program structure.
- Better treatment of tropospheric refraction.
- Improved convergence factor.
- Improved skywave definition, especially for elevated antennas.
- Elimination of redundant calculations.
- More accurate ionospheric reflection coefficient computations.
- Improved diffraction models.
- Better estimates of the reflection altitude.

Elimination of redundant computations in the WEDCOM IV model resulted in reduced computation time. However, the other model improvements required increased computation time. Thus, a computation time comparison of the revised model with WEDCOM IV would have mixed results. For example, low-altitude antenna, low-frequency cases with a uniform ionosphere over the propagation path would execute much faster with the revised model (ie, compared to WEDCOM IV), but increased computation times would probably be required for high-altitude antenna, high-frequency cases with a nonuniform ionosphere over the path. For the purposes of normal WEDCOM usage the high accuracy requirements, the MF cases, and high balloon altitude antennas are not important. Thus, a subset of the above improvements can be incorporated into a revised WEDCOM model that will increase accuracy while not requiring a significant increase in computational time.

Additional improvements to the LF models have been developed for the present effort that will further improve the prediction accuracy and computational efficiency. Also, several new and revised models were prepared for the SIMBAL code (Reference 3) developed for DNA and DCA that can be used in the WEDCOM code with minor revisions. The following model improvements indicate their source:



- Analytic reflection coefficient algorithm (new, SIMBAL).
- Revised LF model formulation which segments the propagation path such that fewer ionospheric reflection coefficient computations are required and improved logic implemented to eliminate repetitive computations (new).
- An improved world surface conductivity model (SIMBAL).
- An improved groundwave computation (SIMBAL).
- A more efficient (and accurate) diffraction computation (new, SIMBAL).

A major cause of the long WEDCOM IV computation times is the ionospheric reflection coefficient computation. Section 3 outlines a new analytic procedure to reduce this requirement. A summary of the remaining LF model improvements listed above is described below. Section 2.2 describes the new procedure for defining calculation increments along the propagation path. Section 2.3 describes the revised world surface conductivity model. Section 2.4 describes the revised skywave definition. An improved groundwave computation is described in Section 2.5. Sections 2.6 through 2.8 briefly describe the revised LF models for diffraction, tropospheric refraction, and ionospheric convergence.

## 2.2 LF MODEL FORMULATION

The WEDCOM LF model presently computes ionospheric electron-ion profiles separated by equal segments along the propagation path. A ground conductivity is specified for each segment. Adjacent ionospheric profiles are linearly interpolated at each skywave ionospheric reflection point followed by the reflection coefficient computation. Thus, the number of reflection coefficient computations can be large, and very repetitive for uniform profiles where anisotropic effects have not changed much. A second area of large computation time usage is the number of repetitive diffraction calculations that are made where the ground constants and ionospheric reflection characteristics have not changed from one skywave hop to the next or where they were computed for an earlier skywave hop.

Figure 1 illustrates the method of ground and ionospheric path segmentation. Ground segment endpoints are chosen so that the segments are of equal length and segment midpoints occur at the transmitter and receiver locations. Ground conductivity calculations are made at the ground segment midpoints. Ionospheric profiles (vertical profile of ionization and collision frequencies) are determined at locations chosen as described in Section 6. The spacing between ionospheric profiles

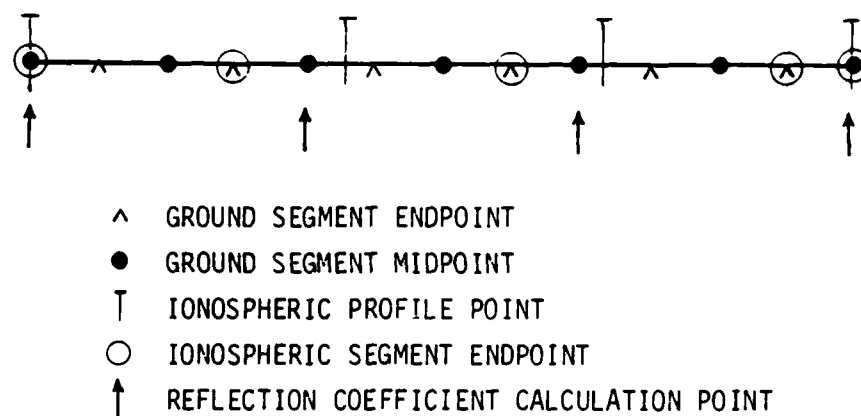


Figure 1. Illustration of LF ground and ionospheric path segmentation.

can differ and the ionospheric profile locations are independent of the ground segment locations. Ionospheric segments are chosen so that ionospheric segment endpoints occur at the transmitter and receiver and at the ground segment endpoint nearest the midpoint between ionospheric profile points.

Reflection coefficient computations are made at the first ground segment midpoint within an ionospheric segment, and thereafter where the anisotropic effects change significantly at a new ground segment midpoint. This criteria continues until the next ionospheric segment has been reached. The end result is a number ( $N_{RC}$ ) of reflection coefficient segments. The number of reflection coefficient segments can be large without a noticeably increased computation time, but will provide:

- Realistic ground conductivity changes along the propagation path.
- Convenient ionosphere segmentation where each segment represents a precomputed ionospheric profile.
- Anisotropic ionosphere sensitivities (tested at each ground segment midpoint) within an ionospheric segment.

Figure 1 illustrates this computation criterion where no additional computations occur due to ionospheric anisotropy ( $N_{RC}$  is equal to 4).

Reflection altitudes at the locations used to compute ionospheric profiles are computed as described in Section 3. Then the skywave geometry is computed by linearly interpolating the reflection altitudes. This procedure is not conceptually different than in WEDCOM IV or the LF model revised for the balloon studies. Now,

however, the number of ionospheric reflections and their incidence angles are kept track of for all skywaves within each reflection coefficient segment. The steepest and most oblique angle of incidence within any one of the segments is known. Thus, the number of reflection coefficient computations within a segment can be minimized by the analytical reflection coefficient representation described in Section 3. Normally within a reflection coefficient, one or two (between extreme oblique and steep incidence) computations need be performed for most cases. Possibly for some selected cases a few more computations are necessary (for example, at the higher LF frequencies where smaller incidence angle spacing is required for accurate interpolation). Nevertheless, the number of computations are significantly reduced from the WEDCOM IV version.

The revised LF model developed for the balloon studies addressed the repetitive nature of the ionospheric reflection coefficient and diffraction calculations. Logical tests were added that used the computations from a prior skywave-hop if the present skywave-hop has the same geometrical and/or ground characteristics. Section 3 describes an improved criteria for testing anisotropy sensitivity. The present effort identified additional internal repetitive computations within the diffraction model which were eliminated through logical tests. The diffraction model improvements are discussed in Section 2.5.

### 2.3 WORLD SURFACE CONDUCTIVITY

The ground conductivity,  $\sigma$ , and relative permittivity,  $\epsilon_r$ , strongly affect the amount of reflected electromagnetic wave losses from the earth's surface. A large range of values exist—typical values are:

<u>Location</u>	<u><math>\sigma</math> Conductivity mho/m</u>	<u><math>\epsilon_r</math> Relative Dielectric Constant</u>
Sea Water	4	81
Fresh Water	$10^{-3}$	81
Wet Earth	$10^{-3}$	18
Dry Earth	$10^{-5}$	5

The importance of the seasonal water content of the soil can be noted.

Fortunately, a detailed conductivity map is not required for ELF/VLF/LF propagation. Indeed, an exact map may lead to inaccuracies as small regions of conductivity, differing from conductivities of larger surrounding regions, should not significantly affect propagation and should not be modeled. Thus, useful

conductivity maps should be gross, with only a few—less than 10— $(\sigma, \epsilon_r)$  pairs representing the world conductivity.

The WEDCOM IV ground conductivity model (Subroutine CONMAP) is a modified version of the Institute of Telecommunication Sciences world conductivity map (Reference 4). Here a Fourier analysis/polynomial interpolation procedure was applied to a world conductivity map. The model uses the Fourier coefficient/polynomial representation to determine a parameter (here called  $\gamma$ ) at a given location. The conductivity ( $\sigma$ ) and relative dielectric constant ( $\epsilon_r$ ) values are determined from the value of  $\gamma$  (as seen in Figure 2 for  $\sigma$ ). Note the continuous variation of  $\sigma$  values. This part of the model is inconsistent with the "gross" requirement for low-frequency propagation, and is especially inaccurate near water-land transitions. Thus, not only is an inaccuracy introduced, but the increased number of possible  $(\sigma, \epsilon_r)$  values limits the effect of more efficient (faster computational) propagation modeling.

It is proposed to replace routine CONMAP with the model used in the SIMBAL code (routine RDCS, Reference 3). The SIMBAL model utilizes a worldwide tabulated data and provides the gross  $(\sigma, \epsilon_r)$  map desired. It is a simple "table lookup" with no computational elegance as done in CONMAP. The outputs are always discrete—not continuous. There are only six  $(\sigma, \epsilon_r)$  pairs output. The only disadvantage in using the SIMBAL model is the data storage (5.2 K versus the 1.5 K in CONMAP). However, this should be outweighed by the improved predictions. Although smaller longitudinal increments are possible the minimum latitudinal variation is 5 degrees or approximately 500 km. Thus it is difficult to justify ground segments less than approximately 250 to 300 km.

## 2.4 SKYWAVE

Figure 3 illustrates the ray-path geometry types found in the geometric-optic model revised for the balloon study. A description of the WEDCOM IV geometry will not be repeated here except to note that it is a subset of these geometries. While only a single ionospheric reflection is shown, extension to multiple hops is straightforward. Figure 3a illustrates four "Earth-Detached" ray paths (designated as "WG" for the classical "Whispering Gallery" phenomena). They are so termed as they never touch the earth's surface. Because it was awkward to draw, ray-path "2" is shown to coincide with ray-path "1." Actually, ray-path "1" is tangent to the earth's surface near each end, and these tangent points lie at lower altitudes than the antenna altitudes. A fifth ray-path could exist that (for a single hop) would also not touch the earth—except by the path extension beyond the RCVR or XMTR

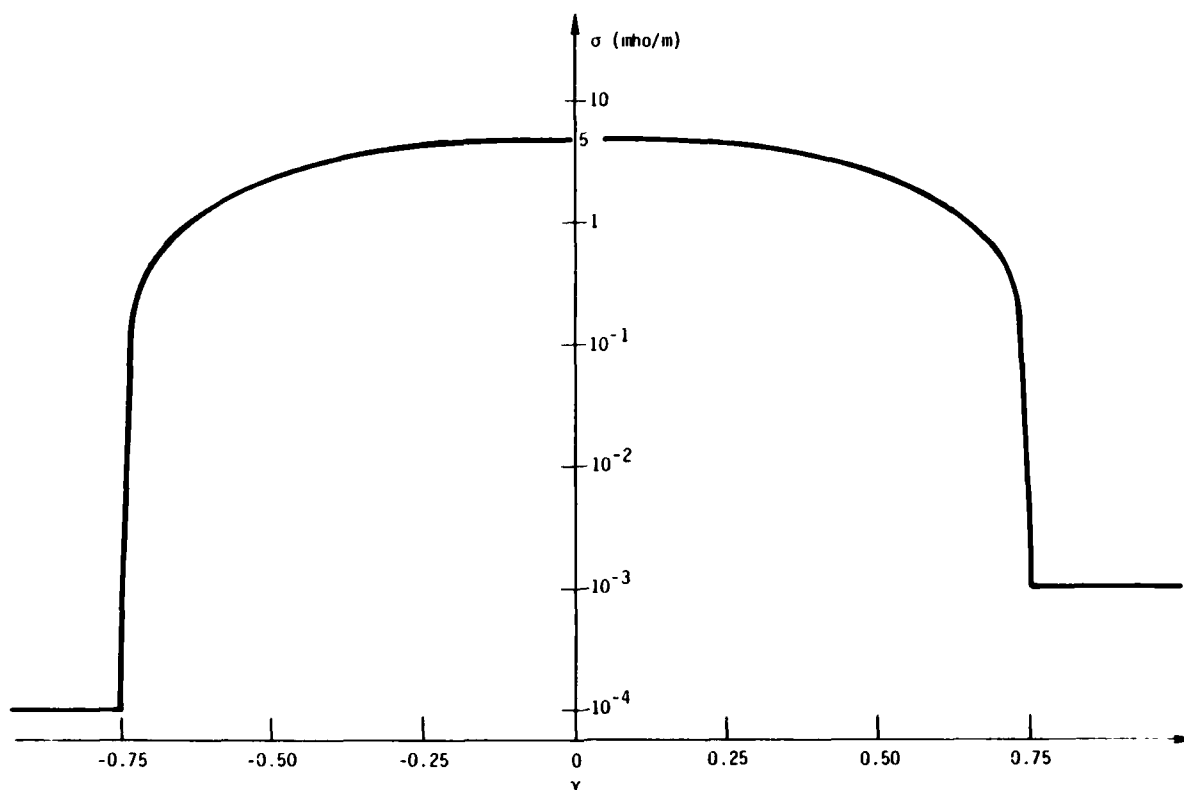
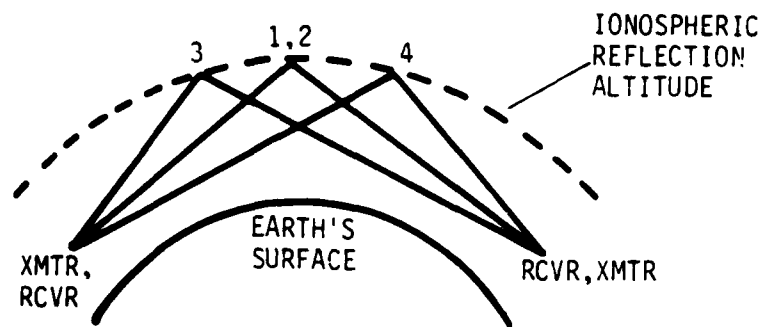


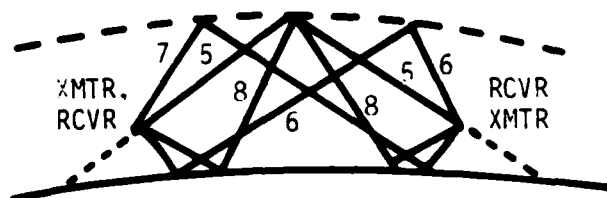
Figure 2. Conductivity prediction as a function of the parameter  $\gamma$  for Subroutine CONMAP used in WEDCOM IV.

locations. This path is shown in Figure 3b (ray-path "5") and is not a WG ray-path. All five types do not coexist for any given number of ionospheric reflections, but a combination of them can. Figure 3b also shows the remaining (E-E) ray-path types. These ray-paths will reflect off the earth's surface. The elevated antenna-to-ground antenna case (E-G) (Figure 3c) illustrates an earth-surface diffracted path and a single earth reflected ray. For the diffracted case the ray-path is tangent at the earth's surface where it diffracts the remaining range to the RCVR. The third geometry mode, ground antenna-to-ground antenna propagation paths, is illustrated in Figure 3d.

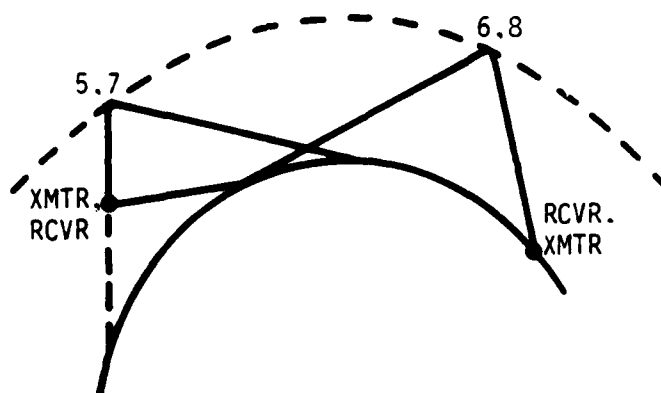
Figure 3b illustrates the 5, 6, 7, and 8 ray-paths types. Note in Figures 3c and 3d how these ray-path types coincide as one or both antennas are on the ground. Table 1 lists the optic-region foreground factors for all eight ray-path cases. For diffracted cases (here the WG ray-paths are not applicable) the foreground factors all correspond to the 1+R geometric-optic case, as the ray-path types 6, 7, and 8 coincide with ray-path type "5."



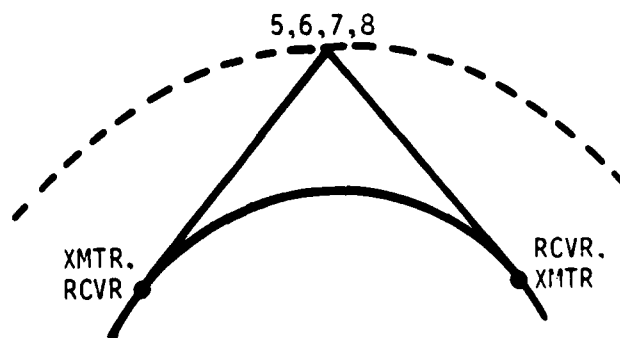
(a) BOTH ANTENNAS ELEVATED (WG)  
(Whispering Gallery or Earth-Detached)



(b) BOTH ANTENNAS ELEVATED (E-E)



(c) ONE ELEVATED AND ONE GROUND ANTENNA (E-G, G-E)



(d) BOTH GROUND ANTENNAS (G-G)

Figure 3. Illustrating the possible single ionospheric reflection ray-path geometry.

Table 1. Foreground factors for geometric optic ray-paths (nondiffracted).

Antenna Case	Ray-Path Type				
	1,2,3,4	5	6	7	8
WG XMTR RCVR	1 1	N.A.	N.A.	N.A.	N.A.
E-E XMTR RCVR	N.A.	1 1	R 1	1 R	R R
E-G XMTR RCVR	N.A.	1 1+R	R 1+R	1 1+R	R 1+R
G-E XMTR RCVR	N.A.	1+R 1	←	1+R R	←
G-G XMTR RCVR	N.A.	1+R 1+R	←	←	←
<ul style="list-style-type: none"> <li>● R is defined as the phase-corrected ground reflection coefficient.</li> <li>● Arrows show the coincidence of ray-path types.</li> </ul>					

Figure 4 illustrates typical daytime propagation ranges versus transmitter antenna elevation angle for ray-paths possessing 2,3--7 ionospheric reflections. The ray-path types defined in Figure 3 are indicated. The "peak" values correspond to where the ray-path is tangent to the earth's surface. The dotted lines denote approximate regions where diffraction modeling must be used, and the approximate Earth-Detached (WG) and geometric-optics regions. In the diffraction region, the ray-path types are grouped (6,4), (8,1), (7,3), and (5,2). The nine-Mm range is selected as an example of how this figure could be used to predict the significant ray-paths and how they are modeled. For this case there are no WG ray-paths as they are within the diffraction regions. The following lists the significant ray-paths (diffraction modeled ray-paths in parenthesis):

<u>Ionospheric Reflections</u>	<u>Ray-Path Type</u>
7	5,6,7,8
6	5,6,7,8
5	(5,2), (6,4), (7,3), (8,1)
4	(5,2)*, (6,4)*, (7,3)*, (8,1)

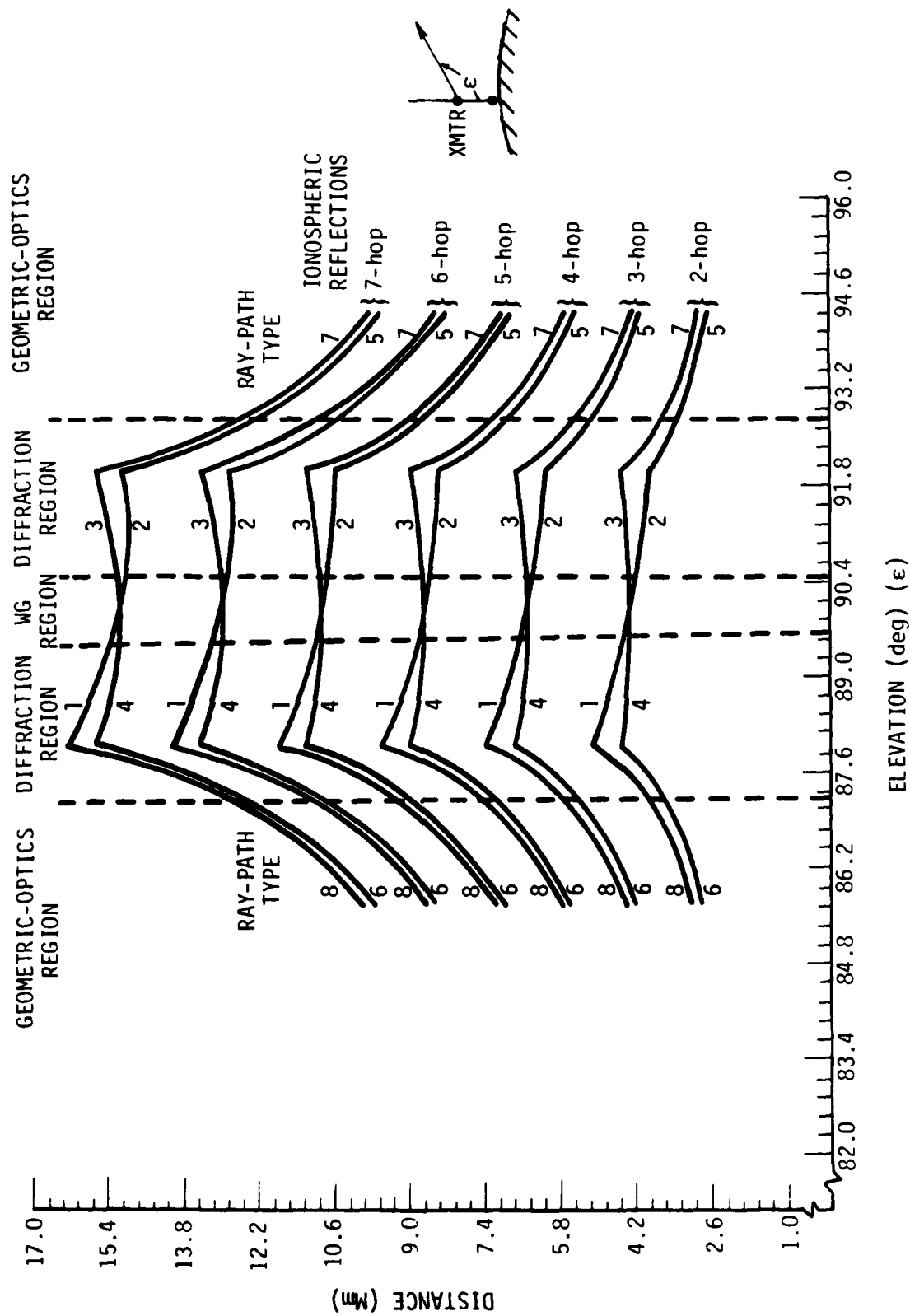


Figure 4. Range along propagation paths as a function of elevation angle (at XMTR) for XMTR and RCVR antenna altitudes at 6 km.



The asterik (\*) ray-paths diffract around the earth's surface to achieve the 9-Mm range.

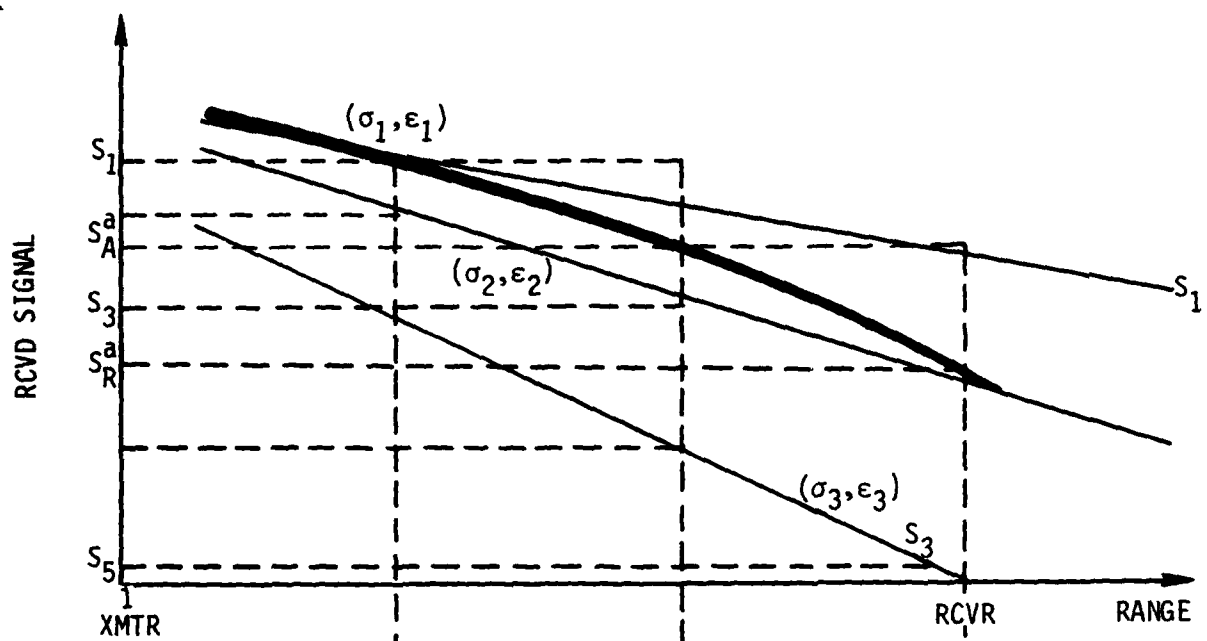
The ray-path characteristics are found in a manner similar to that used in WEDCOM IV. First, the ground elevation angle is set to zero for a given hop number. The range is computed. If this range is shorter than necessary, the hop number is increased until the range is equal to or exceeds the required range. A very fast Newton iteration algorithm is then used to find the ray-path geometry. At least one (ie, for the G-G mode) earth diffracted ray-path is defined, and several are defined for elevated antenna cases. At least two (G-G mode) additional ray-paths with increased ionospheric reflections are also defined. Here again, for elevated antennas (ie, for the E-G, G-E, and E-E modes) this results in a number of individual ray-paths.

## 2.5 GROUNDWAVE

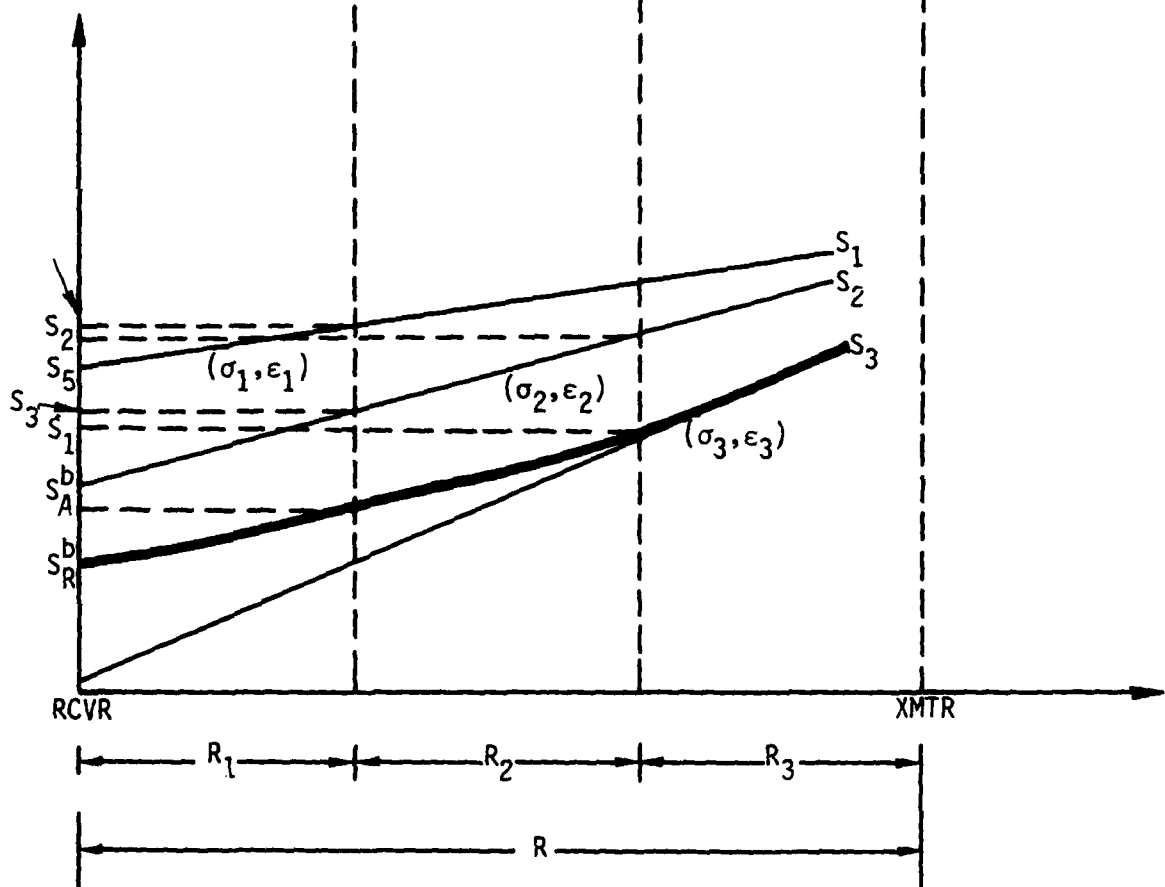
The WEDCOM IV groundwave field computation described in Reference 1 is strictly applicable to a uniform ground conductivity propagation path. For this case only a single computation using that procedure is required. For a variable ground conductivity, WEDCOM IV took an average value of path ground conductivity and again applied the same procedure. The inadequacy of this method is obvious for paths propagating partially over sea water with the remainder being low-ground conductivity.

A combination of physical reasoning and heuristic argument is described by Millington (Reference 5) whereby the computational procedure of Reference 1 is applied iteratively over the variable path conductivity segments. The Millington procedure has shown amazing agreement with more sophisticated computation procedures (References 6 and 7). For example the large field strength recovery crossing from land to sea is predicted by Millington's procedure. Moreover, the signal phase prediction is very accurate, a surprising phenomena as Millington made no consideration of the phase change at the boundary of a conductivity change.

Eckersley (Reference 8) is first credited with the procedure of utilizing uniform ground conductivity computations to piece together a variable conductivity path prediction. Figure 5 demonstrates the Eckersley procedure for a three-segment path. The segment including the transmitter has a ground conductivity pair  $(\sigma_1, \epsilon_1)$ , the center segment  $(\sigma_2, \epsilon_2)$ , and the segment including the receiver  $(\sigma_3, \epsilon_3)$ . The three  $(\sigma, \epsilon)$  pair curves,  $S_1$ ,  $S_2$ , and  $S_3$ , are calculated by the method of Reference 1. The fat solid line in Figure 5 represents the predicted received field strength using the relationships



(a)



(b)

Figure 5. Illustration of Eckersley's procedure.

$$S_A^a = S_1(R_1) \left( \frac{S_2(R_1 + R_2)}{S_2(R_1)} \right) \quad (1)$$

$$S_R^a = S_A \left( \frac{S_3(R_1 + R_2 + R_3)}{S_3(R_1 + R_2)} \right) \quad (2)$$

Eckersley's method does not obey the principle of reciprocity (except for a homogeneous path, a degenerate case).

Millington's method does satisfy the principle of reciprocity as the predicted received signal is the geometric mean of Eckersley's method in Figure 3a ( $S_R^a$ ) and Figure 3b ( $S_R^b$ ) where the transmitter and receiver locations have been interchanged. That is, the predicted received field strength by Millington's procedure is

$$S_R = (S_R^a S_R^b)^{1/2} \quad (3)$$

where  $S_R^a$  was defined above and

$$S_A^b = S_3(R_3) \left( \frac{S_2(R_2 + R_3)}{S_2(R_3)} \right) \quad (4)$$

$$S_R^b = S_A^b \left( \frac{S_1(R_1 + R_2 + R_3)}{S_1(R_2 + R_3)} \right) \quad (5)$$

This example had three segments. Millington generalized the procedure to include N segments:

$$S_R = \left\{ \left( S_1(R_1) \frac{S_1(R)}{S_1(R - R_1)} \right) \left( \frac{S_2(R_1 + R_2)}{S_2(R_1)} \cdot \frac{S_2(R - R_1)}{S_2(R - R_1 - R_2)} \right) \cdots \right. \\ \left. \cdots \left( \frac{S_m(R_1 + R_2 + \dots R_m)}{S_m(R_1 + R_2 + \dots R_{m-1})} \cdot \frac{S_m(R - R_1 - R_2 - \dots R_{m-1})}{S_m(R - R_1 - R_2 - \dots R_m)} \right) \cdots \right. \\ \left. \cdots \left( \frac{S_N(R)}{S_N(R - R_N)} \cdot S_N(R_N) \right) \right\}^{1/2} \quad (6)$$

The parenthesis groupings in Equation 6 correspond to  $(\sigma, \epsilon_r)$  pairs. The implementation of Equation 6 will incorporate the following items for computational efficiency:

- A single  $S_i$  computation will be used if the path is homogeneous.
- Where adjacent  $(\sigma, \epsilon_r)$  pairs are nearly identical they will be merged together so that only the minimum parenthetical groupings will be evaluated.
- The parenthetical computations are added together (rather than multiplied) as the  $\ln(S_i)$  is computed.

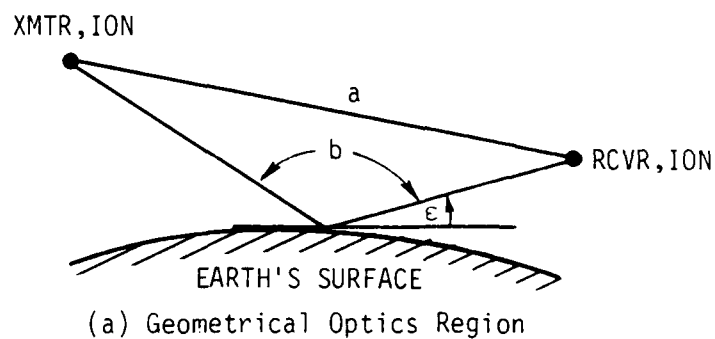
## 2.6 EARTH SURFACE DIFFRACTION, REFLECTION

Section 2.4 described the skywave geometry for the regions where geometric-optics is valid, where diffraction is the dominant characteristic, or in the intermediate (caustic) region (see Figure 6). The model for analyzing the effects due to the earth's surface is now examined. The detailed expressions used by WEDCOM IV for the ground Fresnel reflection coefficients and the diffraction are found in Reference 1 and won't be repeated here.

The caustic region (see Figure 6b) has been a source of model inconsistency. WEDCOM IV switched from the geometric optics model to the diffraction model when the ground elevation angle,  $\epsilon$ , became less than 0.03 radians. This switch point did not provide accurate predictions for many cases. An improved switch criteria is addressed here.

The WEDCOM IV diffraction model is a major user of computation time, second only to the ionospheric reflection coefficient model. There are many repetitive computations in the WEDCOM IV model, especially when the ground conductivity is unchanged for large parts of the propagation path, or when path segments had the same conductivity, but were separated by segments of differing conductivity. This repetition was eliminated in the newer diffraction models thereby reducing (for many cases) the computation times by several factors.

Table 2 lists the cases for which both the geometric-optic and diffraction models were exercised. The caustic region is illustrated in Figures 7 through 10 for an ionosphere-to-ionosphere case, and Figures 11 through 14 for ionosphere-to-antenna cases. A smooth transition from the diffraction to geometric optics models is not always possible. This is often true for the ionosphere-to-ionosphere cases and is shown in Figures 7 through 10. The new model logic will select the lowest magnitude value between the two models which minimizes the abrupt transition. The abrupt transition is due in part to the diffraction model effectively computing a "1+R" value while the geometric-optic model assumes only the Fresnel reflection coefficient "R" ray. Improved transition computation involves a refinement of the



XMTR-TRANSMITTER ANTENNA LOCATION  
 RCVR-RECEIVER ANTENNA LOCATION  
 ION-IONOSPHERIC REFLECTION LOCATION

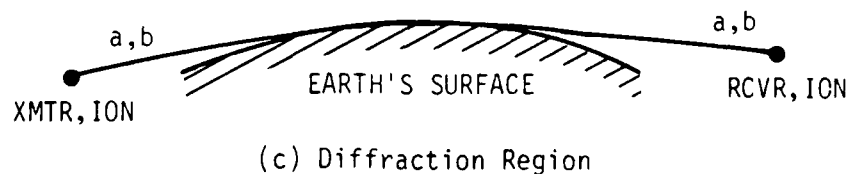
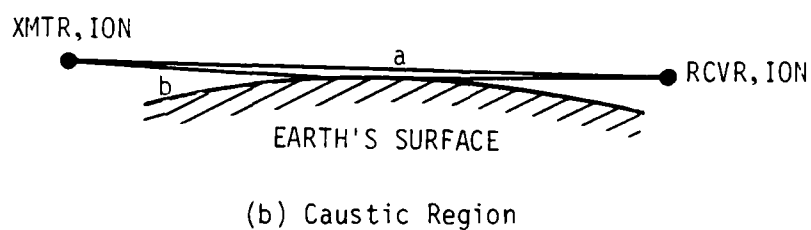


Figure 6. Illustrating how the geometric-optic region ray paths, a and b, converge in the diffraction region.

Table 2. Matrix of cases exercised by the geometric-optics and diffraction models.

Frequency (kHz)	Ground ( $\sigma, \epsilon$ ) (mhos/m)	Reference Altitude 1 (km)	Reference Altitude 2 (km)
$\begin{Bmatrix} 27 \\ 40 \\ 100 \end{Bmatrix}$	$\times \begin{Bmatrix} (0.001, 10) \\ (0.01, 15) \\ 5, 80 \end{Bmatrix}$	$\times \begin{Bmatrix} 80 \\ 60 \\ 40 \end{Bmatrix}$	$\times \begin{Bmatrix} 80 \\ 60 \\ 40 \\ 10 \\ 5 \\ 0 \end{Bmatrix}$

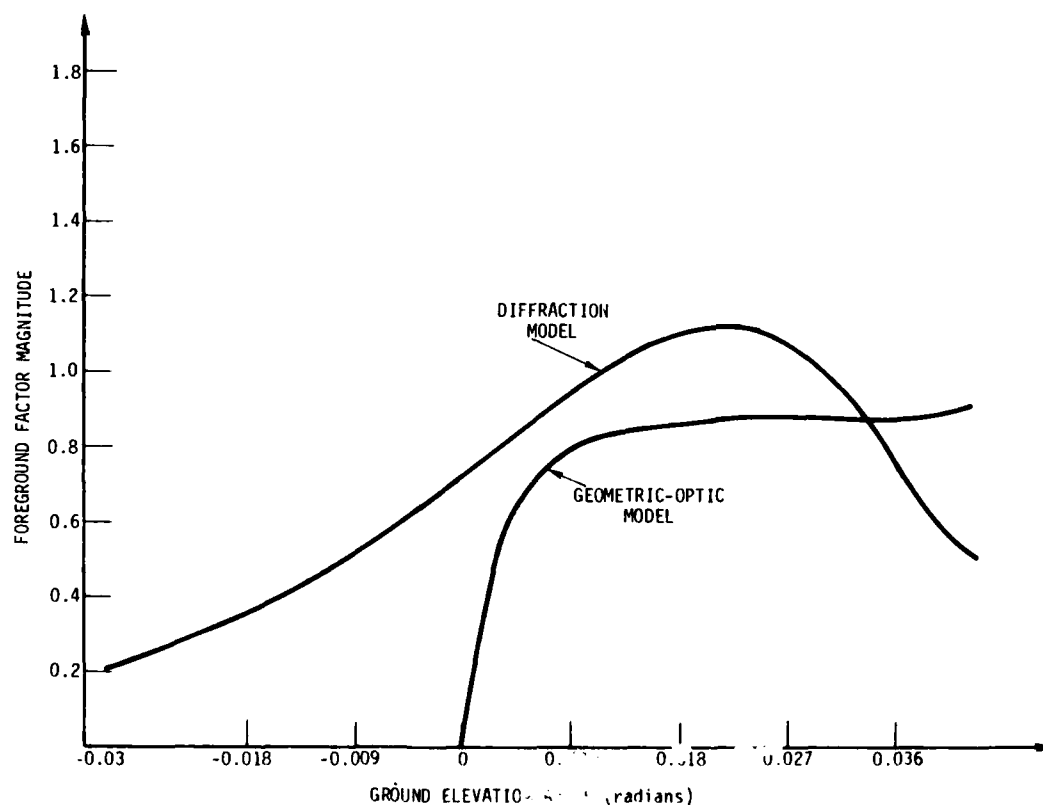


Figure 7. Comparison of geometric-optic and diffraction models of foreground factor in caustic region for ionosphere-to-ionosphere ( $H_p = 80$  km), sea water, and vertical polarization.

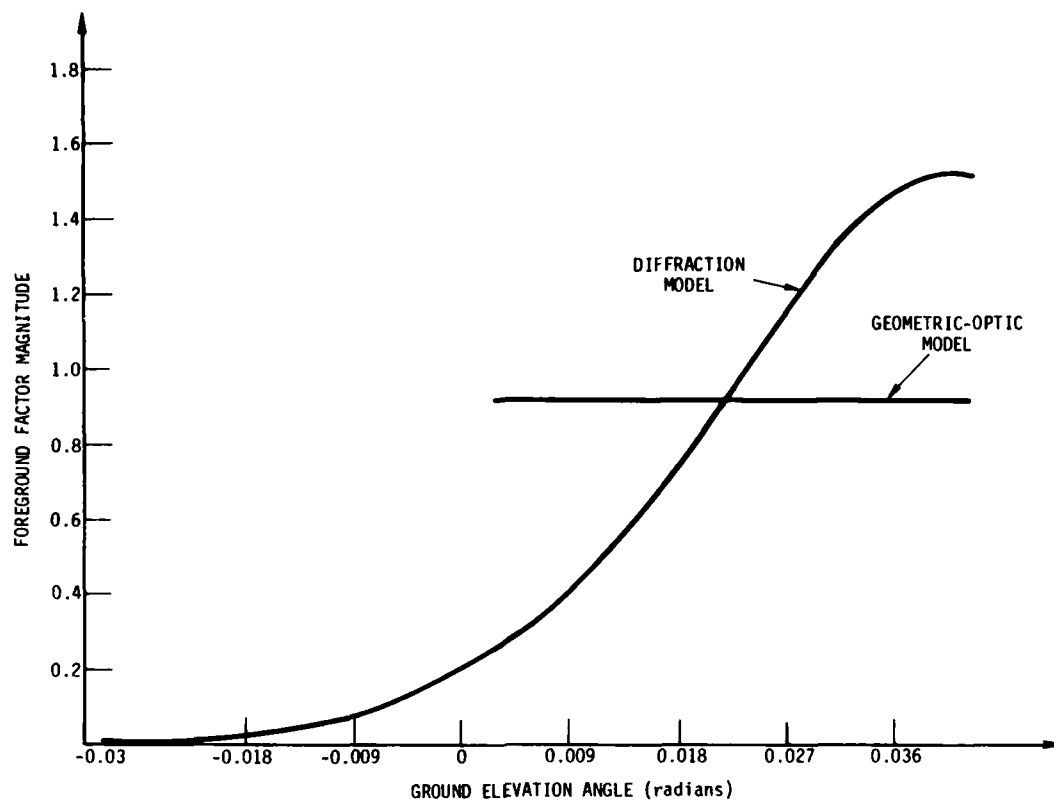


Figure 8. Comparison of geometric-optic and diffraction models of foreground factor in caustic region for ionosphere-to-ionosphere ( $H_R = 80$  km), sea water, and horizontal polarization.

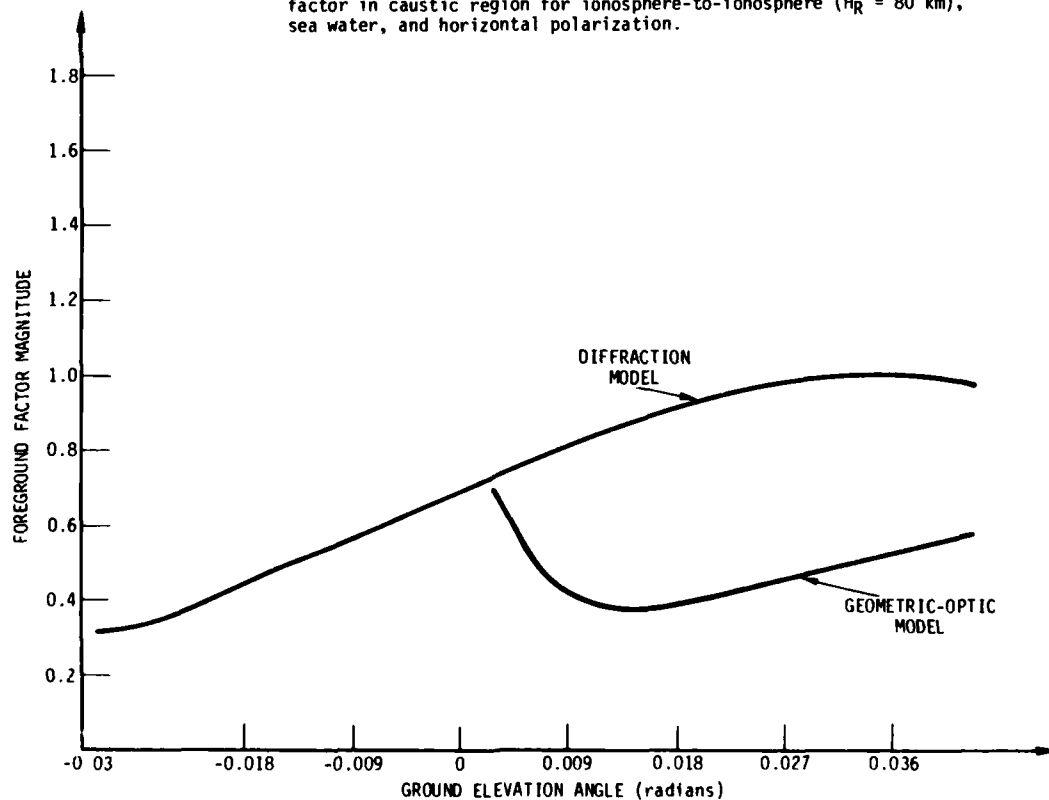


Figure 9. Comparison of geometric-optic and diffraction models of foreground factor in caustic region for ionosphere-to-ionosphere ( $H_R = 80$  km), land, and horizontal polarization.

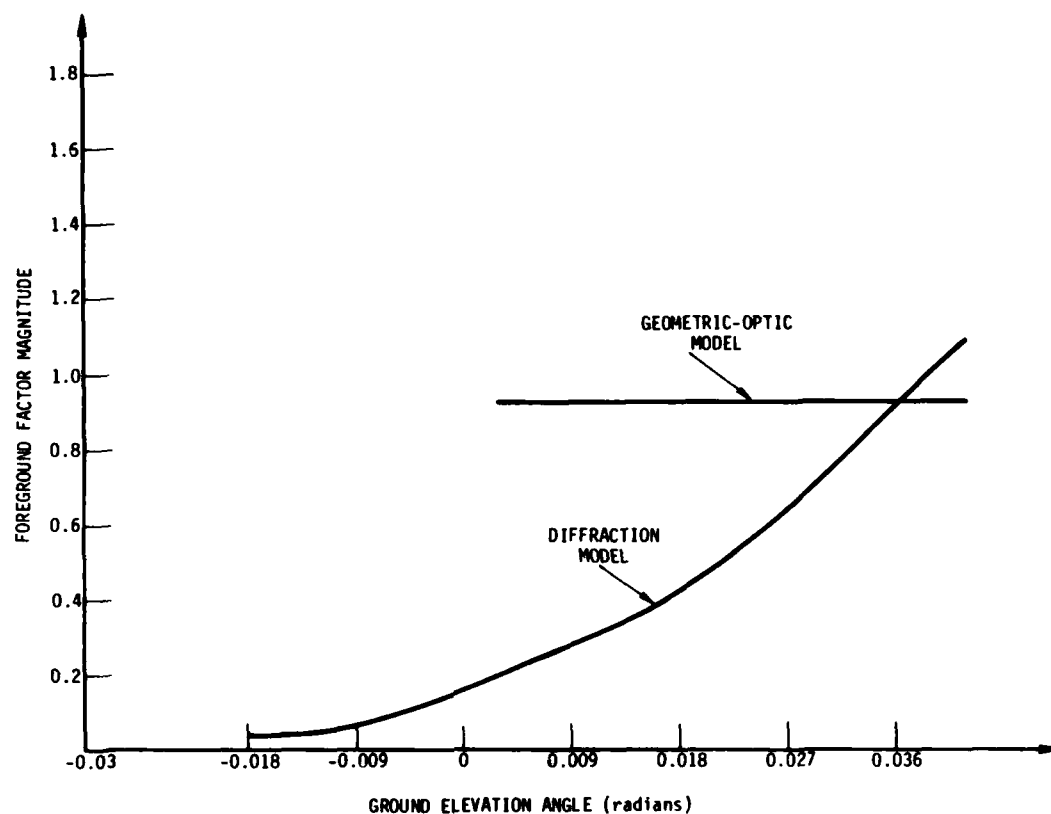


Figure 10. Comparison of geometric-optic and diffraction models of foreground factor in caustic region for ionosphere-to-ionosphere ( $H_r = 80$  km), land, and horizontal polarization.

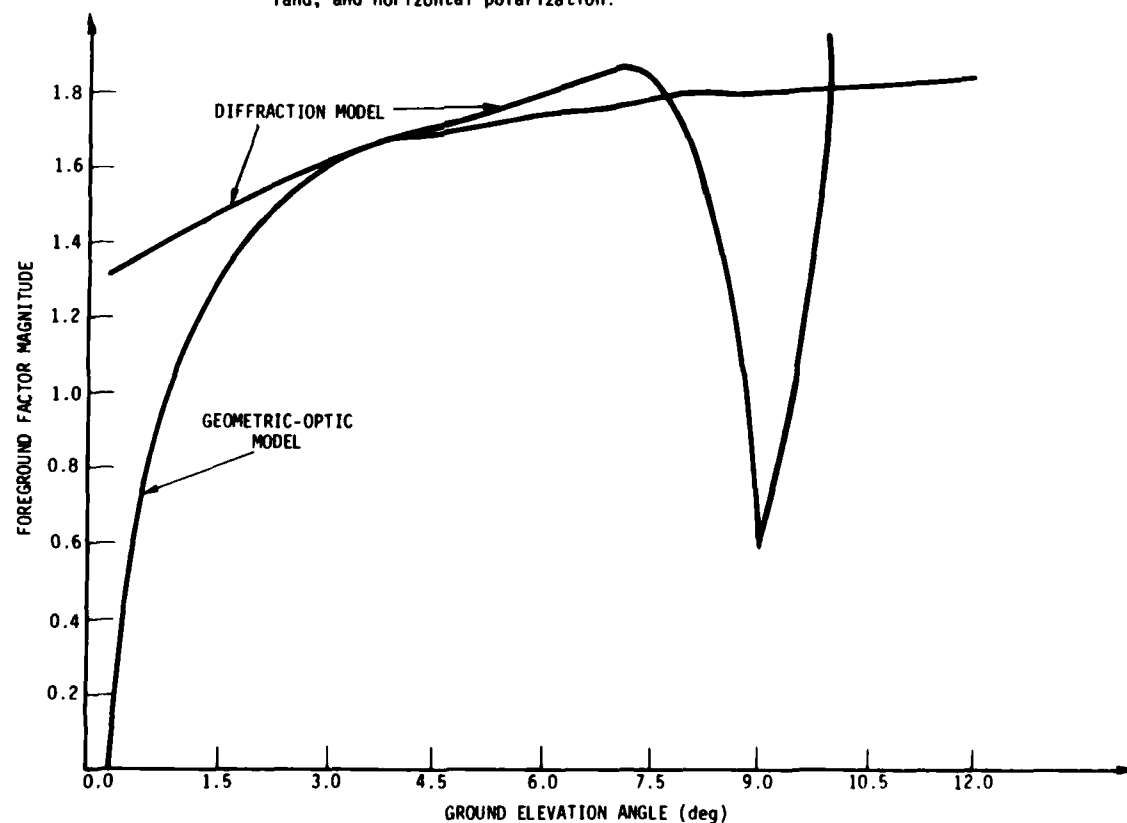


Figure 11. Comparison of geometric-optics and diffraction models of foreground factor in caustic region for ionosphere-to-antenna case ( $H_r = 80$  km, antenna altitude = 0.0 km), land, and vertical polarization.



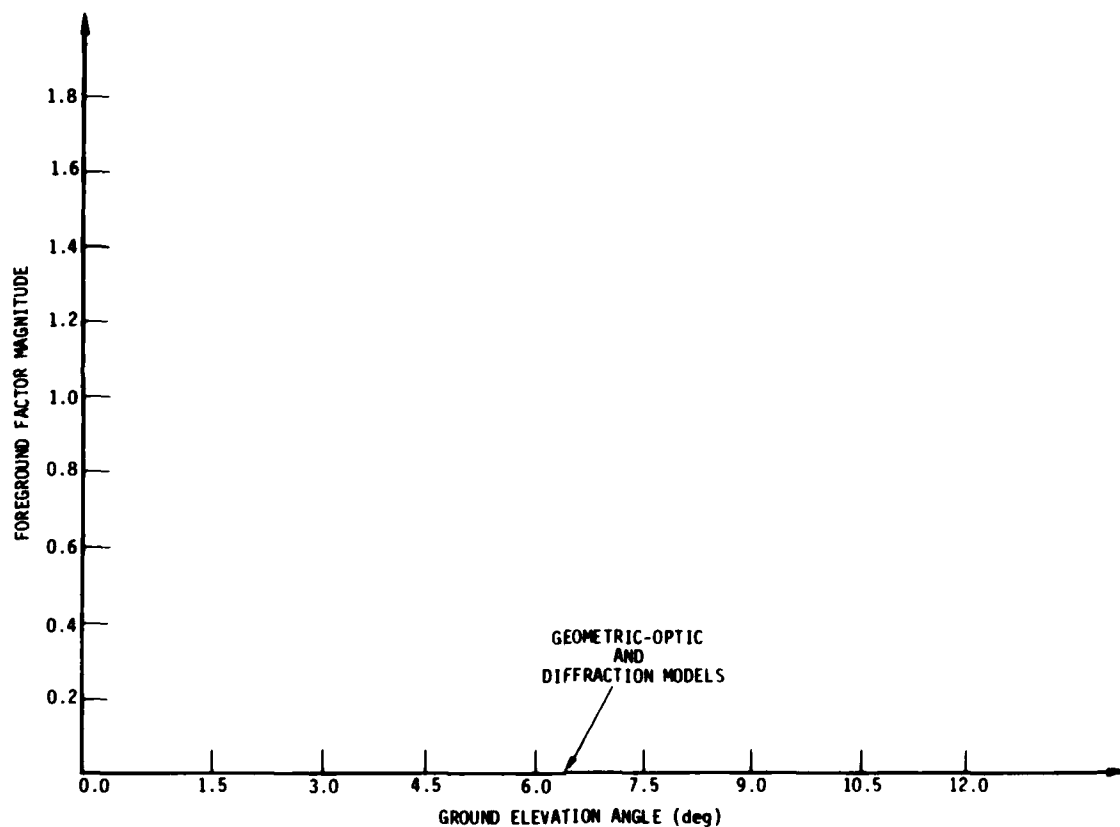


Figure 12. Comparison of geometric-optics and diffraction models of foreground factor in caustic region for ionosphere-to-antenna case ( $H_r = 80$  km, antenna altitude = 0.0 km), land, and horizontal polarization.

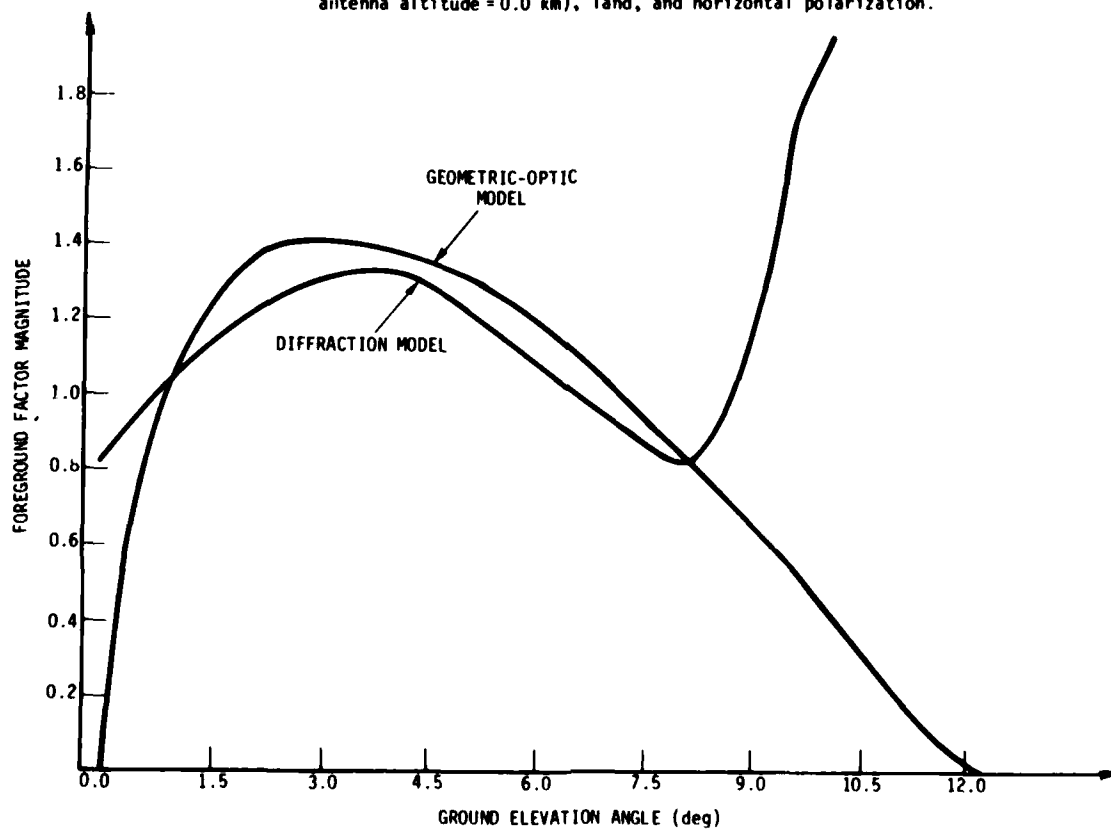


Figure 13. Comparison of geometric optics and diffraction models of foreground factor in caustic region for ionosphere-to-antenna case ( $H_r = 80$  km, antenna altitude = 10 km), land, and vertical polarization.

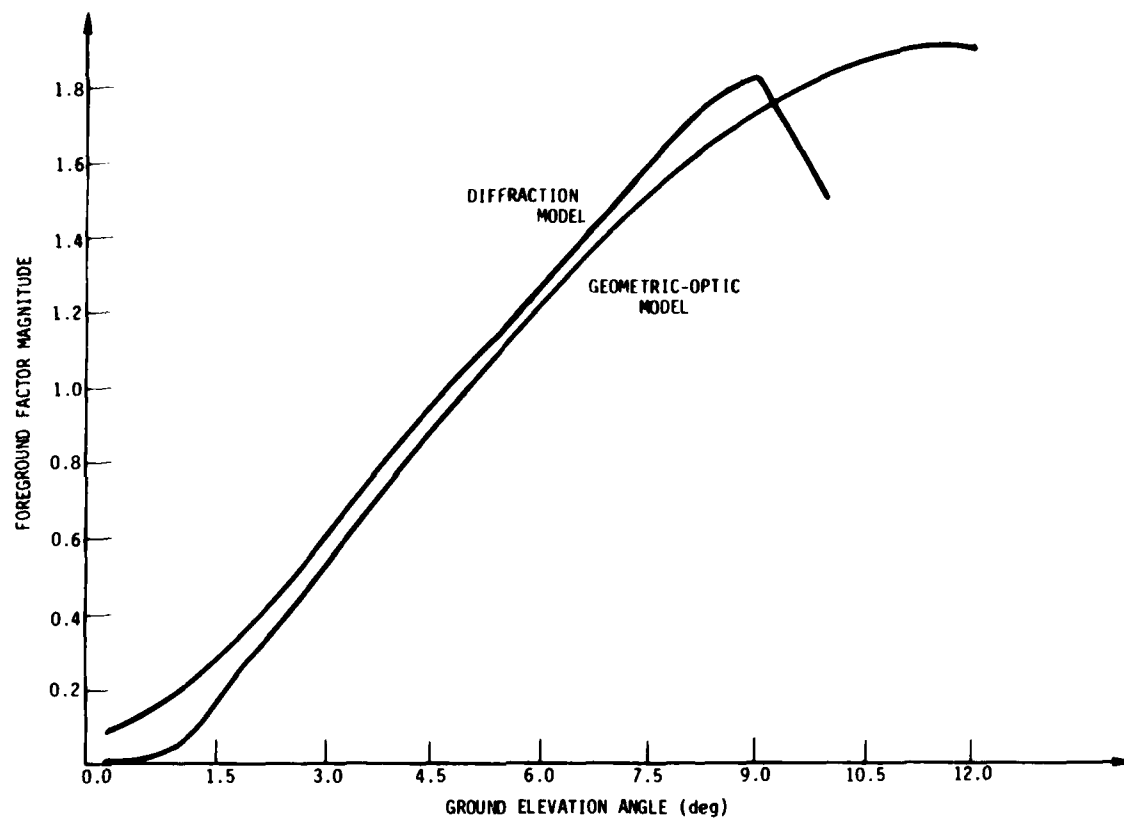


Figure 14. Comparison of geometric optics and diffraction models of foreground factor in caustic region for ionosphere-to-antenna case ( $h_p = 80$  km, antenna altitude = 10 km), land, and horizontal polarization.

skywave definitions (Section 2.4) which will be addressed when this model is implemented into WEDCOM. For the most part, however, the abruptness is due to the separate consideration of the direct "I," and reflected "R" rays in the geometric-optic region.

The transition between the two models is seen to be much smoother for the ionosphere-to-antenna cases (Figures 11 through 14). As mentioned above, the WEDCOM IV model presently switches at 1.72 degrees (0.03 radians). An improved value has been selected based on the Table 2 matrix of computations. This value is 5 degrees which will have a tendency to increase the signal strength from prior model versions.

## 2.7 TROPOSPHERIC REFRACTION

The troposphere has been long recognized as affecting radio waves launched at low elevation angles at VHF frequencies and above. Groundwave signals at LF frequencies (for example, Loran) are also affected by the troposphere refraction effects. Agreement between signal measurements and relatively simple analytic prediction techniques (for example, equivalent earth radius) have made this propagation phenomena well understood. Less clear are the effects of the troposphere on propagation when energy escapes the troposphere and is reflected by the ionospheric region. It is the latter case that is of interest in LF skywave propagation.

WEDCOM IV utilized an equivalent earth's radius in the LF model to account for tropospheric refraction. The VLF model had no refraction modeling and the comparison of LF and VLF model predictions were not favorable due in part to this reason. Tropospheric refraction at VLF and LF was addressed in Reference 2. A summary of results is presented here.

The troposphere had almost no effect at VLF, and little effect for the lower LF frequencies, especially when ionospheric reflection was strong. There was a noticeable effect for the higher LF cases, especially when the ionospheric reflection was weak where the differential reradiated field in the troposphere was comparable to the reradiated field at the ionospheric reflection altitudes. Even for the cases where tropospheric refraction is important, however, the equivalent earth's radius model (ie,  $4/3 a$ , where  $a$  is the actual earth's radius) grossly overestimated the effect on skywave propagation.

The convenience of a ray theory treatment (such as the equivalent earth's radius technique) of tropospheric refraction is obvious. An accurate ray-trace model is inconsistent with the objectives of WEDCOM. The new LF tropospheric refraction model retains an equivalent earth's radius, but with different values empirically

selected in Reference 2. The model characteristics are as follows:

1. An equivalent earth radius of  $4/3 a$  will be used for all diffracted rays and groundwaves for frequencies near 65 kHz and above. The equivalent earth's radius will decrease linearly with frequency from  $a_e = 8485$  km at 65 kHz to  $a_e = 6364$  km at 45 kHz.
2. The earth detached modes are not affected by the troposphere and will use normal earth curvature (ie,  $a = 6364$  km).
3. Skywaves that reflect from the earth's surface will use  $a_e = 7000$  km for 65 kHz and above. A linear decrease (with frequency) to  $a_e = 6364$  km at 45 kHz will be made.
4. Actual earth's radius will be used for all computations below 45 kHz.

## 2.8 CONVERGENCE FACTOR

The ionospheric convergence coefficient is a geometric factor that accounts for the convergence of rays reflected from an idealized spherical reflector. Two important approximations are made in the definition of the convergence coefficient. One is that the geometric optics assumption applies, and the other is that energy is reflected from a thin, well-defined region in the ionosphere. However, the reflection region is not always well defined (Reference 9 addressed this case). Also, when the ray approaches the caustic point the geometrically defined convergence factor becomes infinite since in the vicinity of the caustic the geometric optics assumption fails.

Wait (Reference 10) has developed a correction factor based on wave theory which cancels the infinity and, in general, limits the convergence coefficient in the vicinity of the caustic to about a factor of two. Reference 10 also contains an approximation to extend the definition of the convergence coefficient beyond the caustic point for surface antennas.

When the antennas are elevated, the geometric convergence factor can be very large and remains large even after applying the wave theory correction. Straightforward application of the geometric definition plus wave corrections leads to high peak field values at specific locations that depend critically on path distance and ionospheric reflection altitude. The sensitivity of the convergence coefficient to reflection altitude was addressed in Reference 9.

Figure 15 shows the corrected convergence coefficient as a function of path distance for transmitter and receiver altitudes of 25 km and for parametric reflection altitudes. Note that there is little sensitivity to reflection altitude at distances less than the distance to the caustic, but significant variation at greater distances. In particular, the distance to produce the peak in the convergence factor varies with the reflection altitude. Since the reflection region may be several kilometers thick, a weighted average over the reflection region is used to estimate the convergence coefficient.

The new LF convergence coefficient model in the region beyond but near the caustic limits the geometric convergence coefficient to be no greater than three. This removes the large peaks in the field strength that occur for particular distance-reflection altitude combinations, and causes the total field to vary relatively smoothly with distance as the receiver moves away from the caustic point and the geometric-optics assumption again applies.

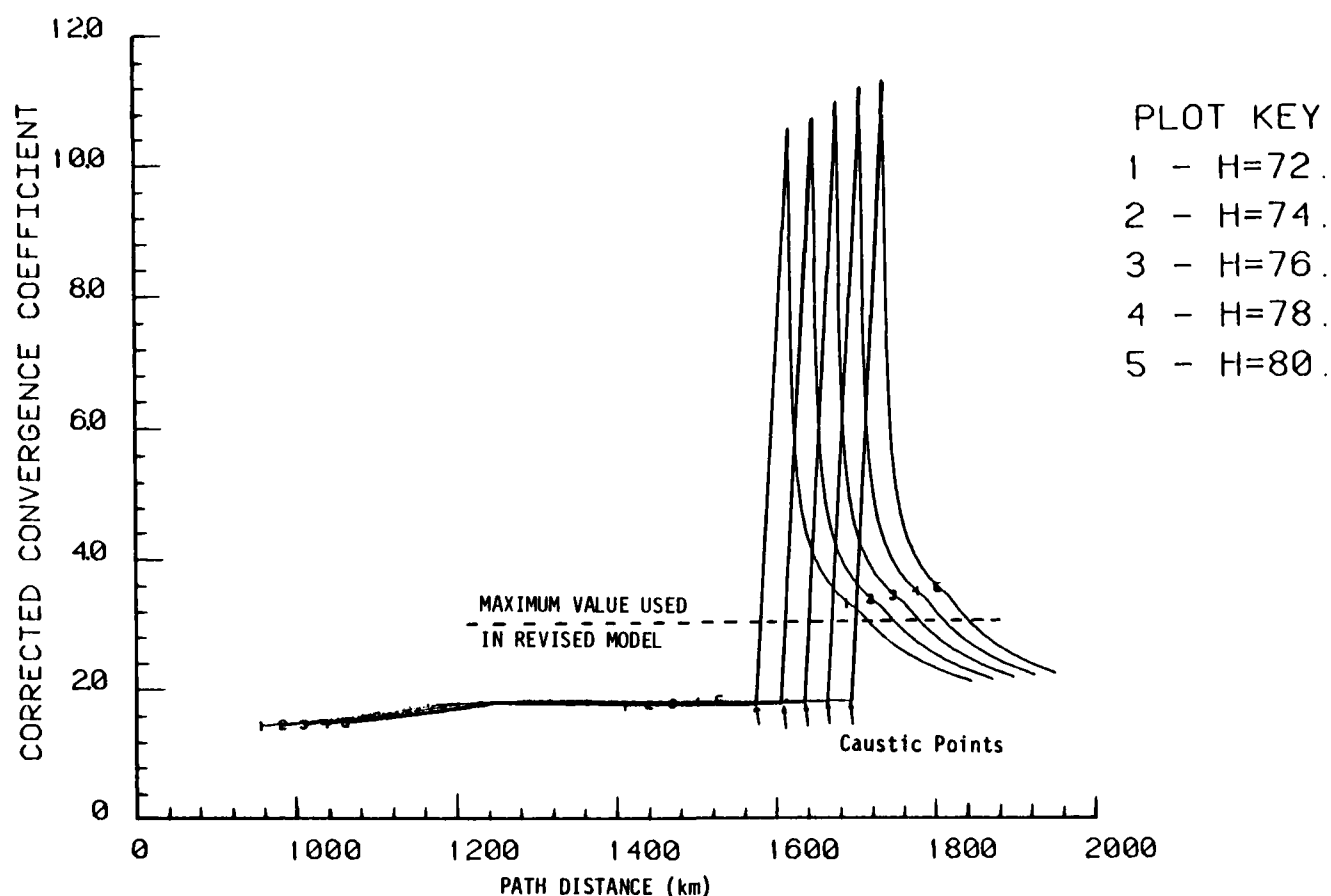


Figure 15. Convergence coefficient sensitivity to reflection altitude.

### SECTION 3

#### IONOSPHERIC REFLECTION ALTITUDE AND REFLECTION COEFFICIENT MODELS

##### 3.1 INTRODUCTION

A reflection altitude calculation is required in both the LF and VLF propagation models. A description of an improved procedure for determining a reflection altitude algorithm is described in Section 3.2. Reflection coefficient calculations are made at ground segment midpoints as described in Section 2.2. Section 3.3 describes improved criteria for determining when anisotropic effects change sufficiently to require reflection coefficient calculations.

The ionospheric reflection coefficient computation is the single largest user of computer time of all the WEDCOM models. Both the waveguide and geometric-optic solutions require this computation to be repeated numerous times. It is thus desirable to eliminate unnecessary computations or scale existing computations whenever possible. Analytic forms of the reflection coefficient are described here that will provide the proper balance between computing time and accuracy. Before proceeding, however, it is appropriate to review the background and nature of the ionospheric reflection coefficient computation.

The ionospheric reflection coefficients can be represented as a four-component matrix, ie,

$$\underline{R} = \begin{bmatrix} {}_{\parallel\parallel}R_{\parallel\parallel} & {}_{\perp\parallel}R_{\parallel\parallel} \\ {}_{\parallel\perp}R_{\perp\perp} & {}_{\perp\perp}R_{\perp\perp} \end{bmatrix}, \quad (7)$$

where

$\underline{R}$  = reflection coefficient matrix

$\parallel$  = polarization parallel to the plane of incidence

$\perp$  = polarization perpendicular to the plane of incidence.

The first subscript applies to the polarization of the incident wave, and the second subscript applies to the polarization of the reflected wave.

The coupling coefficients,  ${}_{\perp\parallel}R_{\parallel\parallel}$  and  ${}_{\parallel\perp}R_{\perp\perp}$ , may be as large or larger than the primary coefficients  ${}_{\parallel\parallel}R_{\parallel\parallel}$  and  ${}_{\perp\perp}R_{\perp\perp}$  for normal nighttime, but they are typically much smaller than the primary coefficients for daytime conditions. For a normal ionosphere, the coefficients are a function of propagation azimuth and the earth's magnetic

field. A nuclear disturbance results in lowering the reflection region. As a consequence of the increased electron-neutral collision frequency in the reflecting region, a strong disturbance can cause the coupling coefficients to be essentially zero.

LF and VLF waves are reflected from the D-region. Most of the reflected energy is returned from the 60- to 70-km altitude level for normal daytime ionospheres and from 80- to 90-km altitude level for normal nighttime ionospheres. In these altitude ranges, particularly for nighttime conditions, the electron-neutral collision frequency is comparable to the electron gyrofrequency, and the earth's magnetic field has a significant effect on the reflection coefficient.

Presently, the WEDCOM IV code (Reference 1) employs two calculation procedures for determining the ionospheric reflection coefficients. The first method is an iterative integration of a first-order differential equation. It is applicable to both isotropic and anisotropic ionospheres. The second procedure is an application of a simple recursive technique and is used only with isotropic ionospheres.

The iterative integration is a very complex calculation and its efficiency depends critically on well-defined starting (highest) altitudes and stopping (lowest) altitudes, numerical error criteria, and integration stepsize. In the past, this computation was economized by adjusting these constraints. While this technique did reduce the running time, it remained substantial. Moreover, for some applications the "adjustments" resulted in unacceptable integration accuracies.\* Setting the integration criteria to values that assure acceptable accuracy for all cases requires a more stringent criteria than now found in WEDCOM IV.

A significant reduction in computation time can be obtained if an analytic form for the reflection coefficient can be used where the coefficients are determined from only a few reflection coefficient calculations. This has been done in WEDCOM for isotropic conditions. Previous attempts to find useful analytic forms for anisotropic conditions have only been partially successful in that they resulted in poor modeling over part of the region of interest. Recent work described in Section 3.4 has lead to an applicable analytic form that can be used in WEDCOM for both isotropic and anisotropic conditions.

---

\* Inaccuracies tend to occur as the frequency is increased, for the more steep incident angles, and as the ionospheric profile becomes lossy over large regions.

### 3.2 REFLECTION ALTITUDE

WEDCOM IV presently uses a simple analytic formulation to determine the reflection altitude,  $H_R$ . It is a simplified derivative of the more accurate expression

$$\text{Re}(\cos^2 \theta_i) = 2.0 |\chi| / \left( (8 + \cos^2 \xi)^{1/2} - \cos \xi \right) \quad (8)$$

where  $\text{Re}$  means "real part of,"  $\chi$  is the isotropic susceptibility (defined in the next section) evaluated at  $H_R$

$$\xi = \tan^{-1} \left[ \text{Im}(\chi) / \text{Re}(\chi) \right] \quad (9)$$

and  $\theta_i$  is the angle of incidence at the ionosphere (see Reference 1). The relationship in Equation 8 is satisfied at a single altitude (ie,  $H_R$ ) and, thus the value of  $H_R$  is insensitive to signal propagation effects below or above this altitude. Actually, reflection occurs at every point in the medium and to compute the effective reflection altitude accurately, the contribution for each altitude needs to be summed for the effects on the signal seen below the reflection region.

Detailed studies were made in References 2 and 3 which indicated that  $H_R$ , while always high as derived from Equation 8, was reasonably accurate when the ionospheric reflection region was very sharp.  $H_R$  was found to be much too high for some disturbed profiles where the reflection region was large or when the reflection process was weak. This is illustrated in Figures 16 and 17 where the up and down-going H-field and Poynting vector components are shown. Note the sharp reflection gradient for the normal nighttime. For the studies in Reference 2 an effective reflection altitude,  $H_E$ , was selected at the point where the downgoing  $H_y$  component (HYD) is one-half the total reflected value. Thus, while  $H_R$  is high it is not too excessive for normal night. For the disturbed environment, however,  $H_E$  is considerably below  $H_R$ . Figure 18 shows the value of  $H_R$  and the altitude range from which an effective reflection altitude could be selected.

The determination of  $H_E$  as performed above is not computationally practical for the purposes of WEDCOM. An analytic form such as Equation 7 is still required. The value of  $H_R$  is high as it doesn't actually account for the signal absorption at lower altitudes. Also shown on Figure 18 is a corrected value of  $H_R$ ,  $H_{RC}$ , which was made by reducing  $H_R$  by  $H_\chi$ , ie

$$H_{RC} = H_R - H_\chi \quad (10)$$



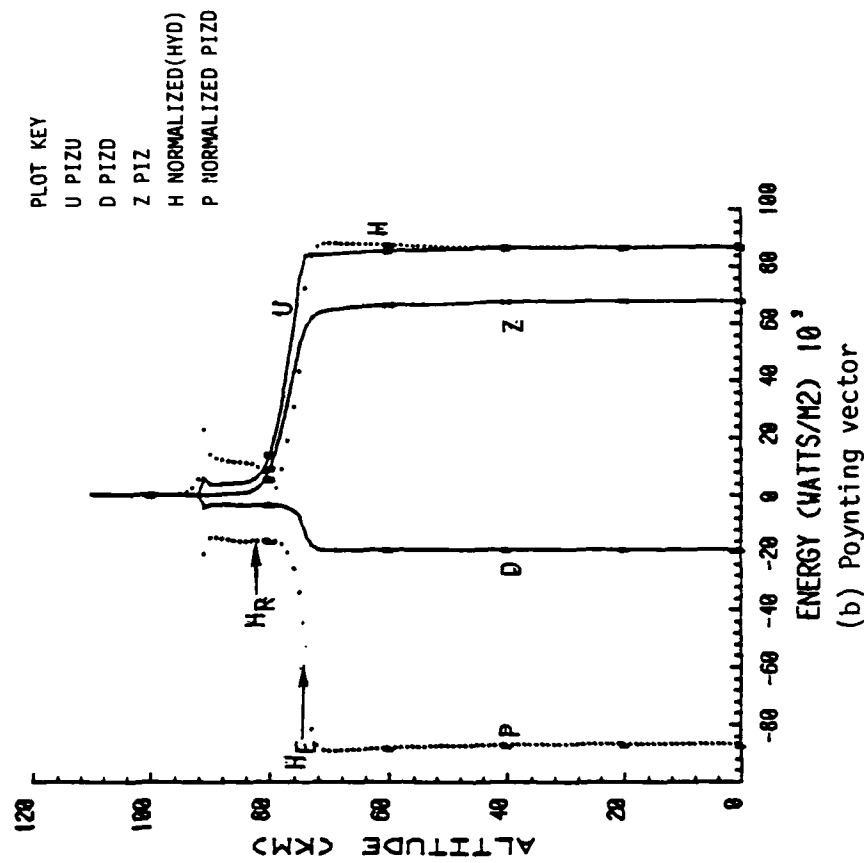
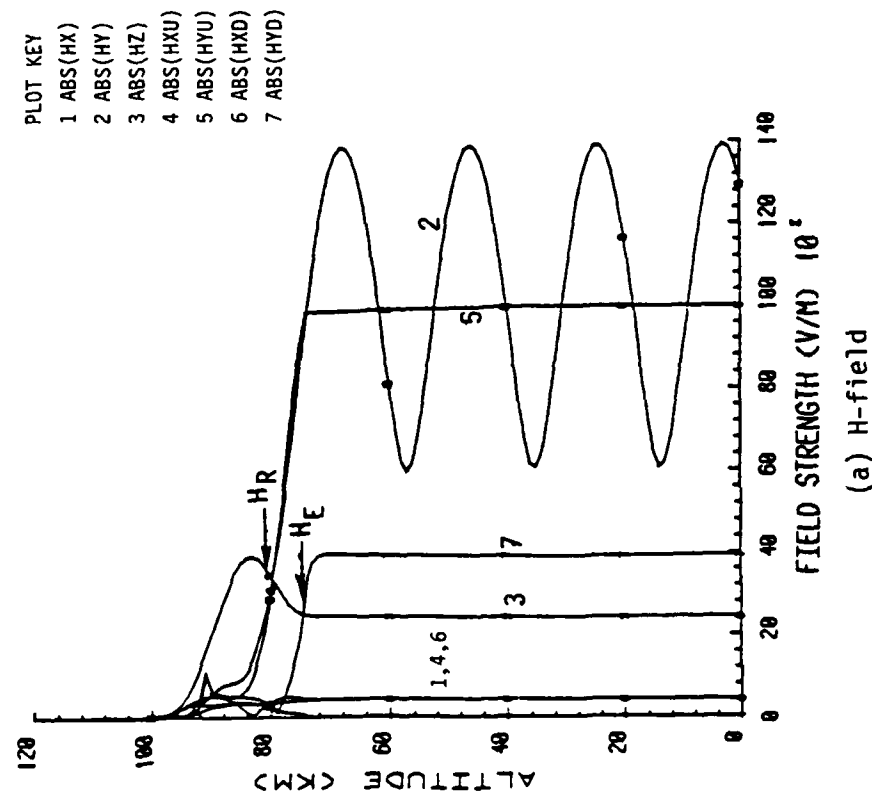


Figure 16. H-field component magnitudes and Poynting vector components in vertical direction (z) for normal nighttime conditions, for 40 kHz and  $\theta_i = 80^\circ$ . x is the direction of propagation and y is the direction orthogonal to x, z and perpendicular to the direction of propagation.

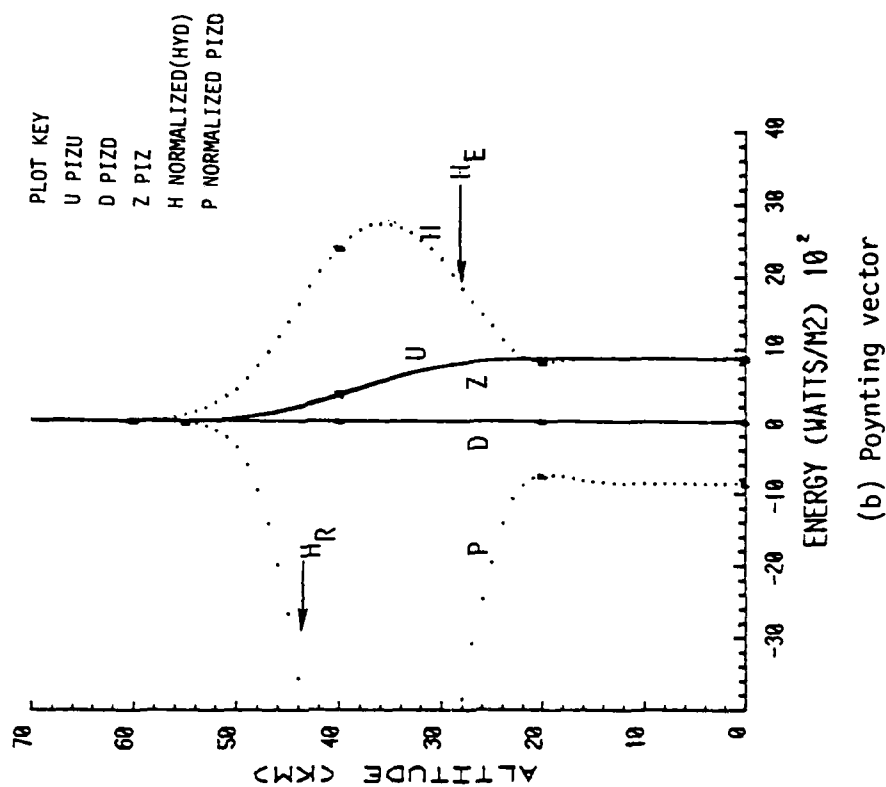
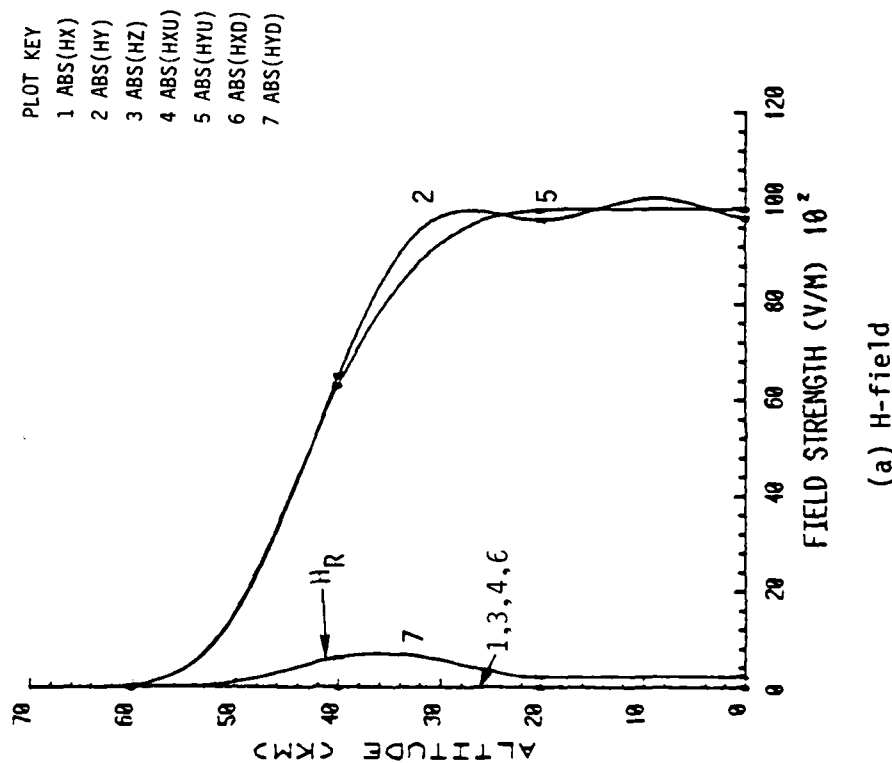


Figure 17. H-field component magnitudes and Poynting vector components in vertical direction (z) for strong gamma nuclear disturbance, for 40 kHz and  $\theta_i = 80^\circ$ . x is the direction of propagation and y is the direction orthogonal to x,z and perpendicular to the direction of propagation.

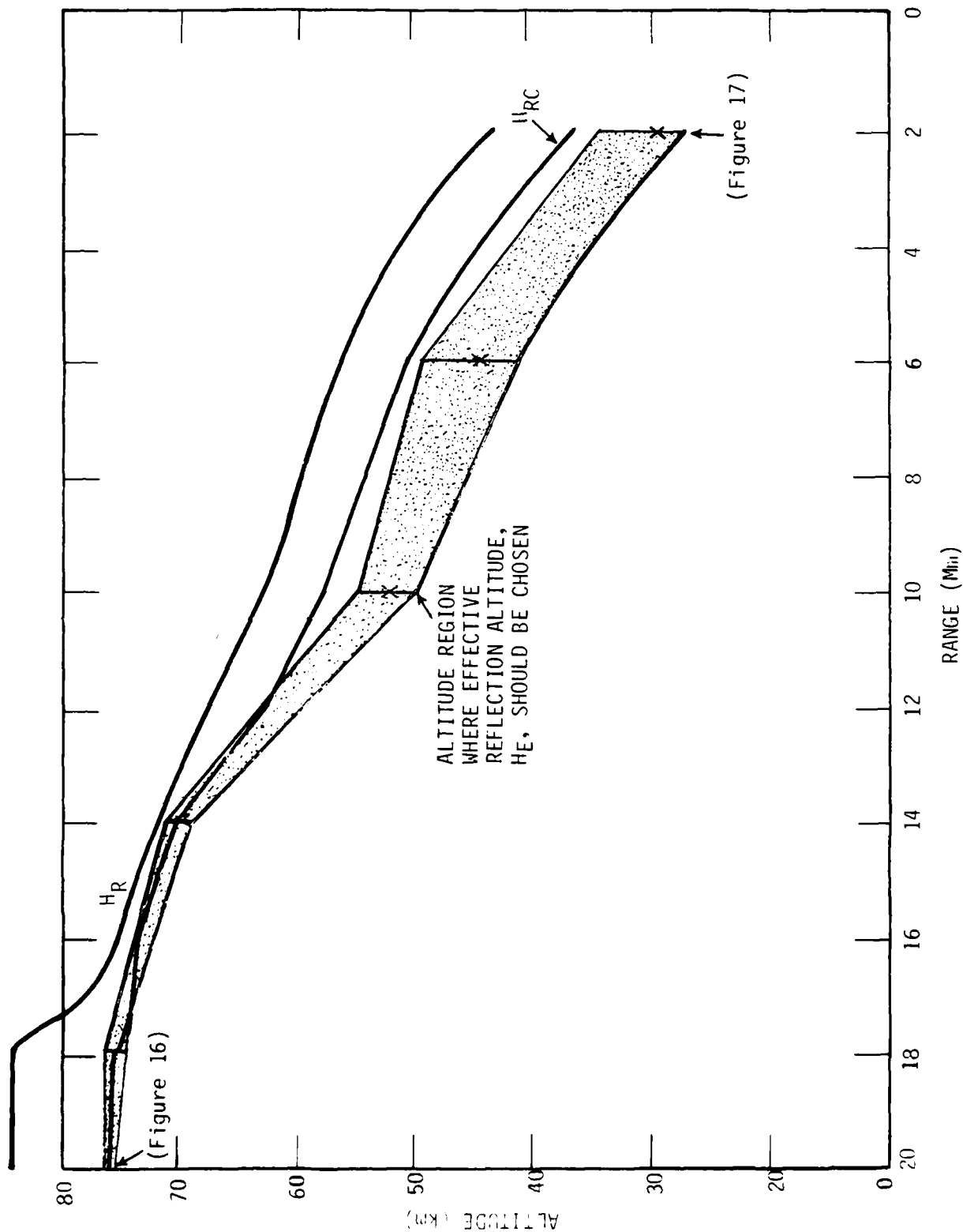


Figure 18. Comparison of analytic reflection altitude ( $H_R$ ), corrected ( $H_{RC}$ ), and altitude region where effective altitude should be selected for 40 kHz,  $\theta_i = 80^\circ$ , and for the range away from a high-altitude burst where gamma deposition is dominate.

where

$$H_X = \frac{d}{dz} \ln |X|^{-1} \Big|_{z=H_R} \quad (11)$$

The effective reflection region is still lower than  $H_{RC}$  for much of the disturbed region shown in Figure 18. However, for the overall set of computations performed to test Equation 10, it performed well.

### 3.3 COMPUTATION CRITERIA FOR ADJACENT VERTICAL IONOSPHERIC PROFILES

It has been long known that the reflection coefficient sensitivity to changes to the earth's magnetic field characteristics decreases as:

1. The ionosphere becomes more depressed due to increased solar activity (day versus night, PCA events) or to nuclear disturbances.
2. The distance from the magnetic equator (increasing magnetic dip angle).

Correspondingly, the reflection coefficient sensitivity to changes in the magnetic azimuth also decreases. In the past, WEDCOM IV used a broad criteria to reduce the number of computations resulting from a reduced magnetic field anisotropy. The criteria relied on practical experience with reflection coefficient computations where it was known that the magnetic field sensitivity was negligible. The difficulty with this criteria was the broadness of it—that it permitted repetition of many near identical reflection coefficient computations. Therefore, there was a need to develop a new criterion which would be sensitive to magnetic field changes as they affect the reflection coefficient computation. To be effective this new criterion must be computationally fast as was the old criterion.

A function used in the reflection coefficient computation is

$$q = \frac{\omega}{c} \left( \cos^2 \phi_i + \chi_{11} \right)^{1/2} \quad (12)$$

where  $\omega$  is the signal frequency (radians),  $c$  is the velocity of light, and  $\phi_i$  is the ionospheric incidence angle (assumed here to be  $80^\circ$ ). The parameter  $\chi_{11}$  is the first diagonal term of the susceptibility matrix defined as

$$\chi_{11} = - \frac{X}{U} \left( \frac{U^2 - \ell^2 Y^2}{U^2 - Y^2} \right) \quad (13)$$

where

$$j = \sqrt{-1}$$

$$X = (\omega_p/\omega)^2$$

$$U = 1.0 \cdot j(\nu/\omega)$$

$$Y = \mu_o \omega_m / \omega \text{ (henrys)}$$

$$\omega_m = \text{magnetic gyrofrequency (s}^{-1}\text{)}$$

$$\omega_p = \text{plasma frequency (s}^{-1}\text{)}$$

$$l = \cos \theta_D \cos \phi_a$$

$$\theta_D = \text{magnetic dip angle (deg), and}$$

$$\phi_a = \text{magnetic azimuth (deg).}$$

For an isotropic ionosphere  $q$  reduces to the vertical planewave propagation constant. The imaginary part of  $q$  is thus a measure of the signal attenuation at the altitude it was determined. The  $q$ 's computed in the reflection region have the sensitivity to the magnetic field strength important to the reflection coefficient computation.

The following procedure will be used to determine whether adjacent locations along the propagation path should have separate reflection coefficient computations:

1. Determine if the reflection altitude,  $H_R$ , has changed. If so, compute new reflection coefficients. If not,
2. Compute  $q$  for both vertical profiles. If the difference in  $Im(q)$  exceeds  $\delta_q$  where

$$\delta_q = \begin{cases} 0.03 & \text{for Normal Night} \\ 0.005 & \text{for all other cases} \end{cases} \quad (14)$$

then the computations for both locations should be made.

The values assigned to  $\delta_q$  are somewhat arbitrary and must be considered preliminary. They were obtained by comparing the value of  $q$  with the reflection coefficient behavior for the cases listed in Table 3. Figures 19 through 21 are a sample of the data generated. Figure 19 illustrates the general behavior of  $Im(q)$  for magnetic dip and azimuth and for normal and a moderately disturbed environment. Figures 20 and 21 are sample outputs of the reflection coefficient sensitivity to magnetic field effects and disturbed environments. Tables of representative azimuth

Table 3. Parameters varied in  $q$  and ionospheric reflection coefficient calculations to obtain  $\delta_q$ .

<u>PROFILE</u>	Normal Night and Normal Day Spread debris night = $10^{-12}$ , $10^{-11}$ , $10^{-10}$ , $10^{-9}$
<u>DIP ANGLE</u>	30, 50, 70 degrees
<u>MAGNETIC AZIMUTH</u>	-85, -65, -45, -25, -5, 15, 35 55, 75 degrees
<u>FREQUENCIES</u>	27, 40, 100 kHz

increments ( $\Delta$ ) were created where  $\Delta$  represented the azimuth change where the magnitude of  $_{\parallel}R_{\parallel}$  was always within 1 dB change. Note the sensitivity of  $\Delta$  with dip angle and with the disturbed environment. The proper choice of  $\delta_q$  will incorporate this sensitivity. The  $\delta_q$  values in Equation 14 are not stringent and will not have the needed sensitivity for some cases (especially light disturbed cases). A more conservative value  $\delta_q = 0.0001$  will assure that the same criterion is met in almost all cases.  $\delta_q$  tends to require a larger value for profiles nearer normal night and higher frequencies and a more sophisticated set of values will be selected.

### 3.4 INTERPOLATION ALGORITHM

In the past, an analytic form of the reflection coefficient

$$r_i(C_i) = - \exp(\alpha C_i)$$

$$C_i = \cos \theta_i \quad (15)$$

has been used (see, for example, Reference 11 where  $r_i$  represents  $_{\parallel}R_{\parallel}$ ,  $_{\perp}R_{\perp}$ ,  $_{\parallel}R_{\perp}$  or  $_{\perp}R_{\parallel}$ , and  $\theta_i$  is the angle of incidence at the ionosphere. Only a single reflection coefficient computation is needed to determine the complex valued  $\alpha$ . This form was accurate for lower VLF and for sharp gradient isotropic ionospheres. The isotropic formulation in WEDCOM (Reference 1) improved this form, ie,

$$r_i(C_i) = - \exp(\alpha C_i) \exp\{j\alpha_1 C_i^2\} \quad (16)$$

where the real valued  $\alpha_1$  better accounted for less sharply reflecting gradients. Neither of these forms did well in representing highly anisotropic profiles, however, especially where the reflection gradients were not simple.

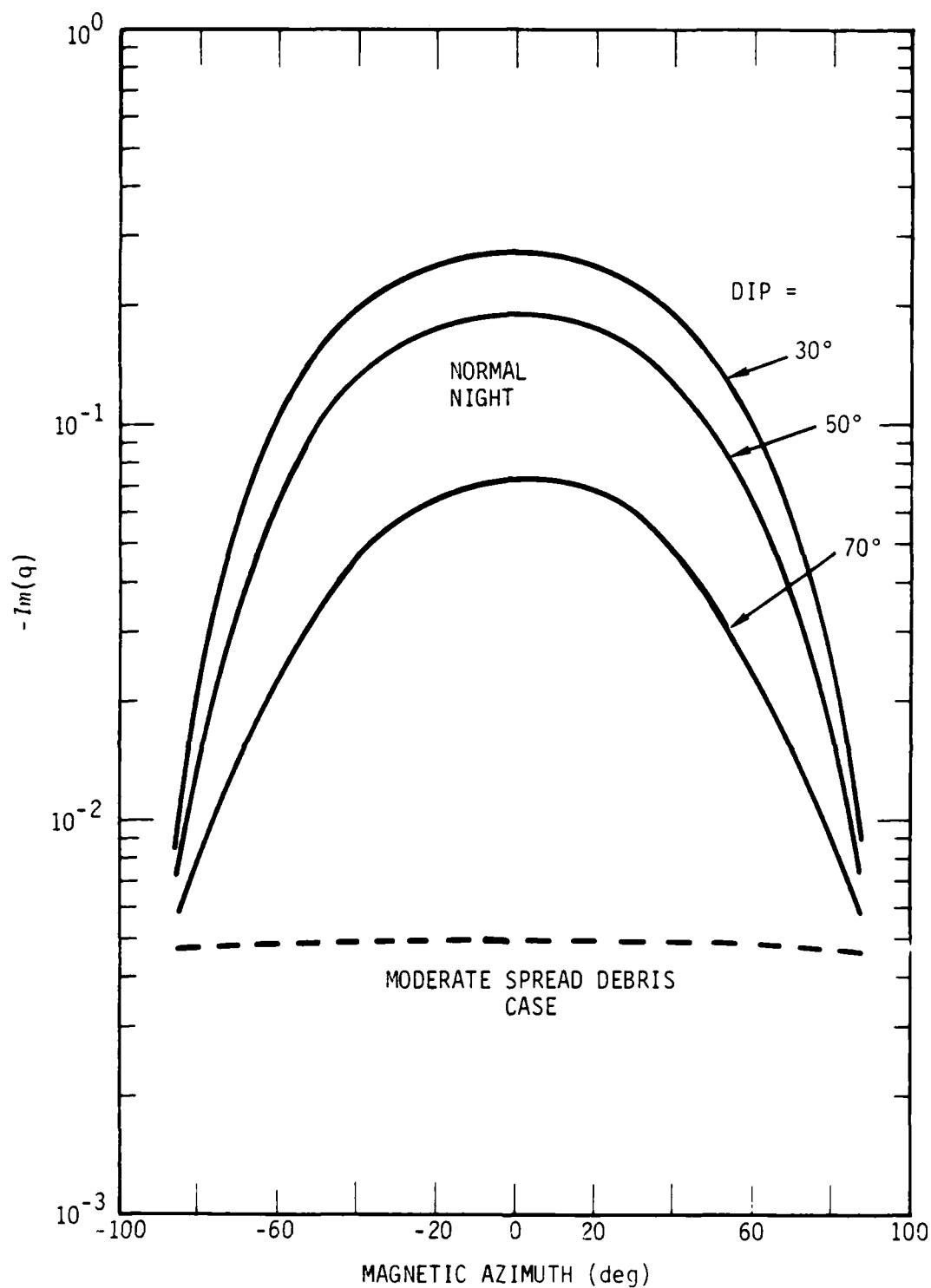
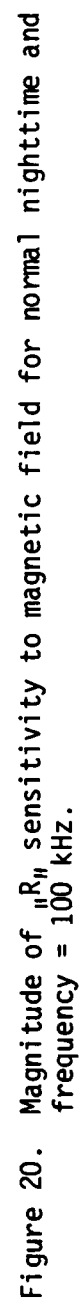


Figure 19. Magnetic field and ionospheric profile sensitivities of  $Im(q)$  for frequency = 40 kHz.





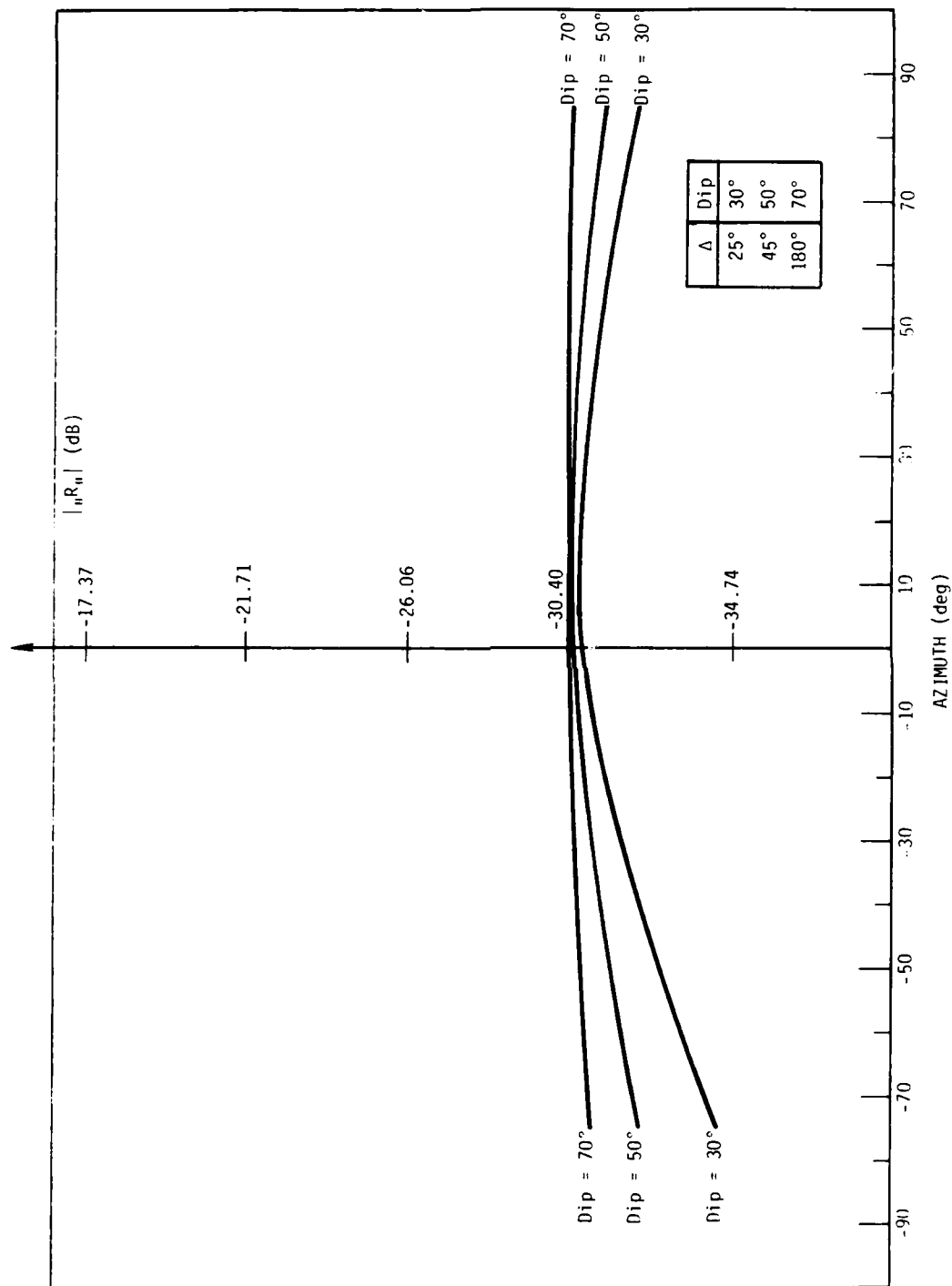


Figure 21. Magnitude of  $R_u$  sensitivity to magnetic field for moderate spread debris case for frequency = 100 kHz.

Two recent efforts have provided more information on representing the reflection coefficient in an analytic form and/or interpolating between values. The work described in Reference 2 utilized an analytic form of the reflection coefficient, but this form could only be used every 1/2 degree (or smaller) in  $\theta_i$  to retain the needed accuracy. Fortunately, this fine increment was needed only for the MF frequencies being analyzed, and it was shown that lower VLF/LF frequencies did not require as small an increment. Figure 22 provides examples of the  $\theta_i$  sensitivity for a normal nighttime ionosphere where computations were performed every 1 degree. For the MF case (350 kHz) the 1-degree increments used do not provide the needed sensitivity for  ${}_1R_1$ . For the LF case (100 kHz) the 1-degree increment is satisfactory. The structure noted in these figures become less apparent as the frequency is reduced and as the ionosphere becomes more depressed. It is interesting to note the relative values of the diagonal and cross terms of the reflection coefficient matrix. It is difficult to generalize the characteristics for anisotropic profiles such as this one. In any case it was determined that an analytic form

$$r_i(C_i) = \exp(A + BC_i) \quad (17)$$

would well represent the individual anisotropic reflection coefficients if the  $\theta_i$  increment was small enough.

The second work which required an analytic form of the reflection coefficient is described in Reference 3. A very large data base of reflection coefficients was generated parametrically with frequency (27 through 100 kHz),  $\theta_i$  (75 through 82 degrees), magnetic dip (30, 50, 70 degrees), and azimuth (-75 through 85 degrees), day and night, and spread debris and gamma source nuclear environments. The Equation 17 formulation was used with a least-means-squared measure (as a function of  $\theta_i$ ) to compute representative complex valued A and B. With few exceptions, the analytic form well represented the reflection coefficient, especially for the lower frequencies and for the more disturbed cases. The appropriateness of this form is seen in Figures 23 through 27. Here samples of the general linear behavior of  ${}_{11}R_{11}$  and  ${}_1R_1$  are demonstrated for normal and disturbed ionospheric profiles, frequencies of 27 and 40 kHz, and dip angles of 30 and 70 degrees. The phase behavior illustrated in Figure 24 is typical (note  $2\pi$  discontinuity). That is, it has a very linear behavior with  $\cos \theta_i$ . Note the change in the sign of the slope between  ${}_{11}R_{11}$  and  ${}_1R_1$ . This was often observed for the anisotropic profiles. Figure 27 shows how the anisotropic sensitivity disappears as the ionosphere becomes depressed.

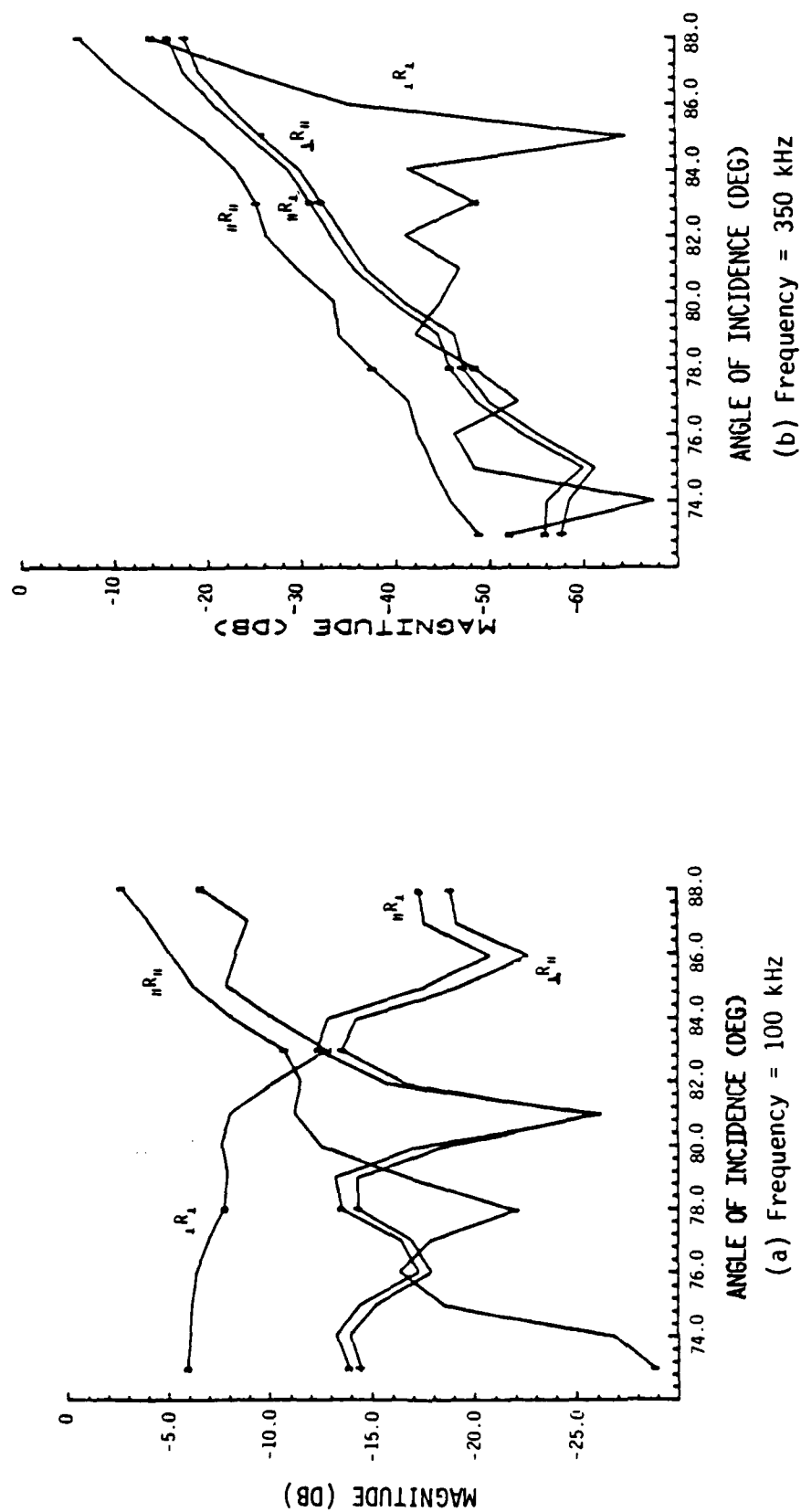


Figure 22. Reflection coefficients for normal nighttime as a function of  $\theta_i$ .

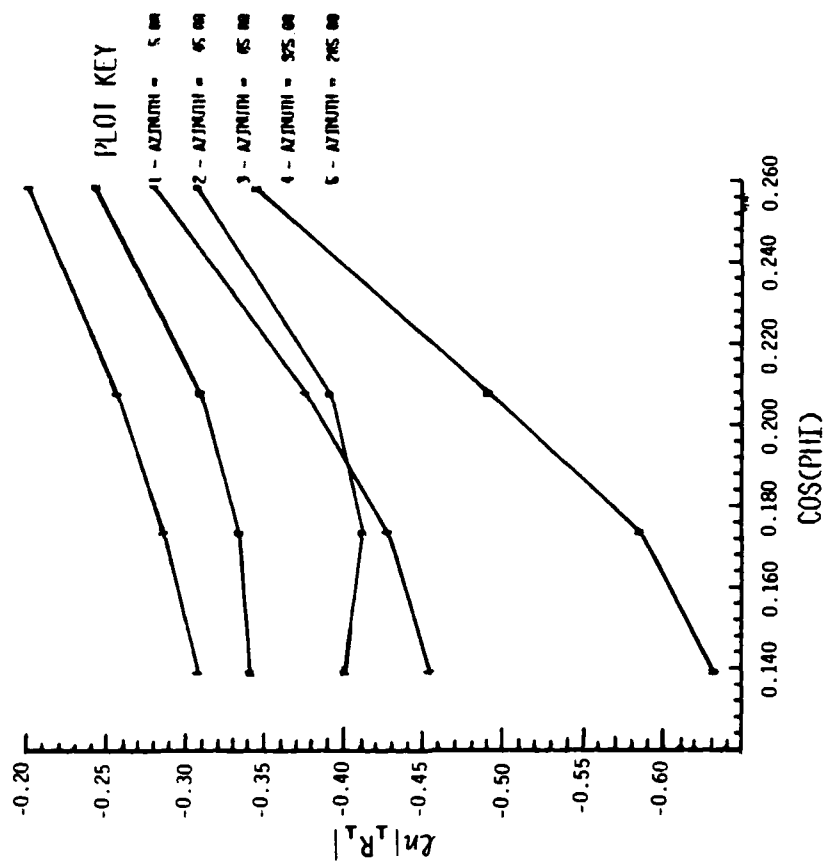
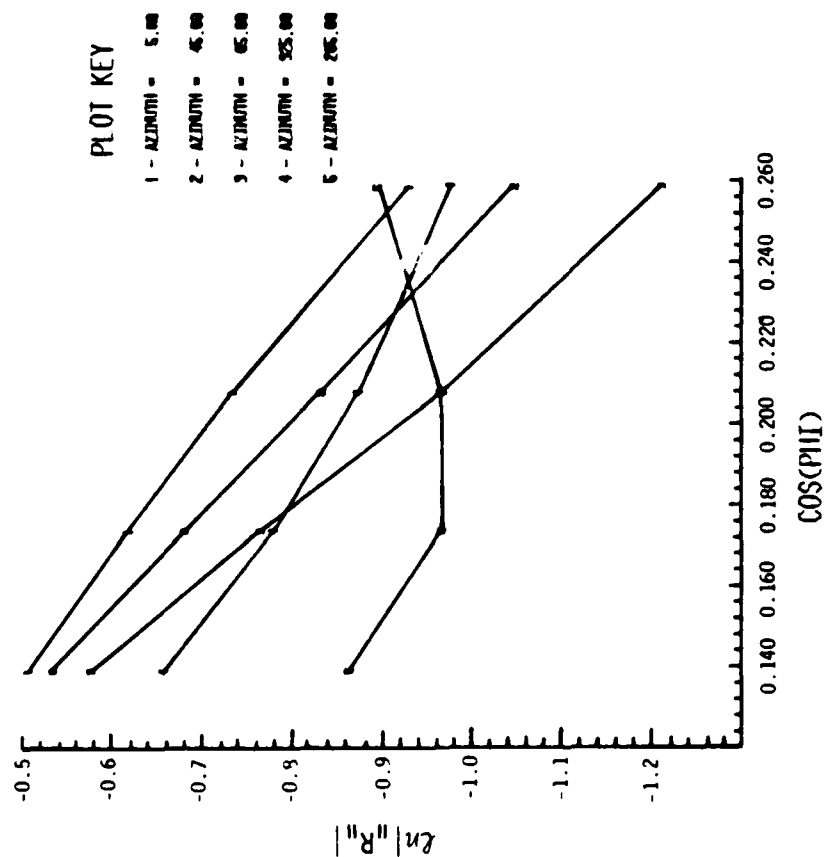


Figure 23. Magnitude of  $R_{\parallel}$  and  $R_{\perp}$  for a normal night, dip = 70°, and frequency = 27 kHz.

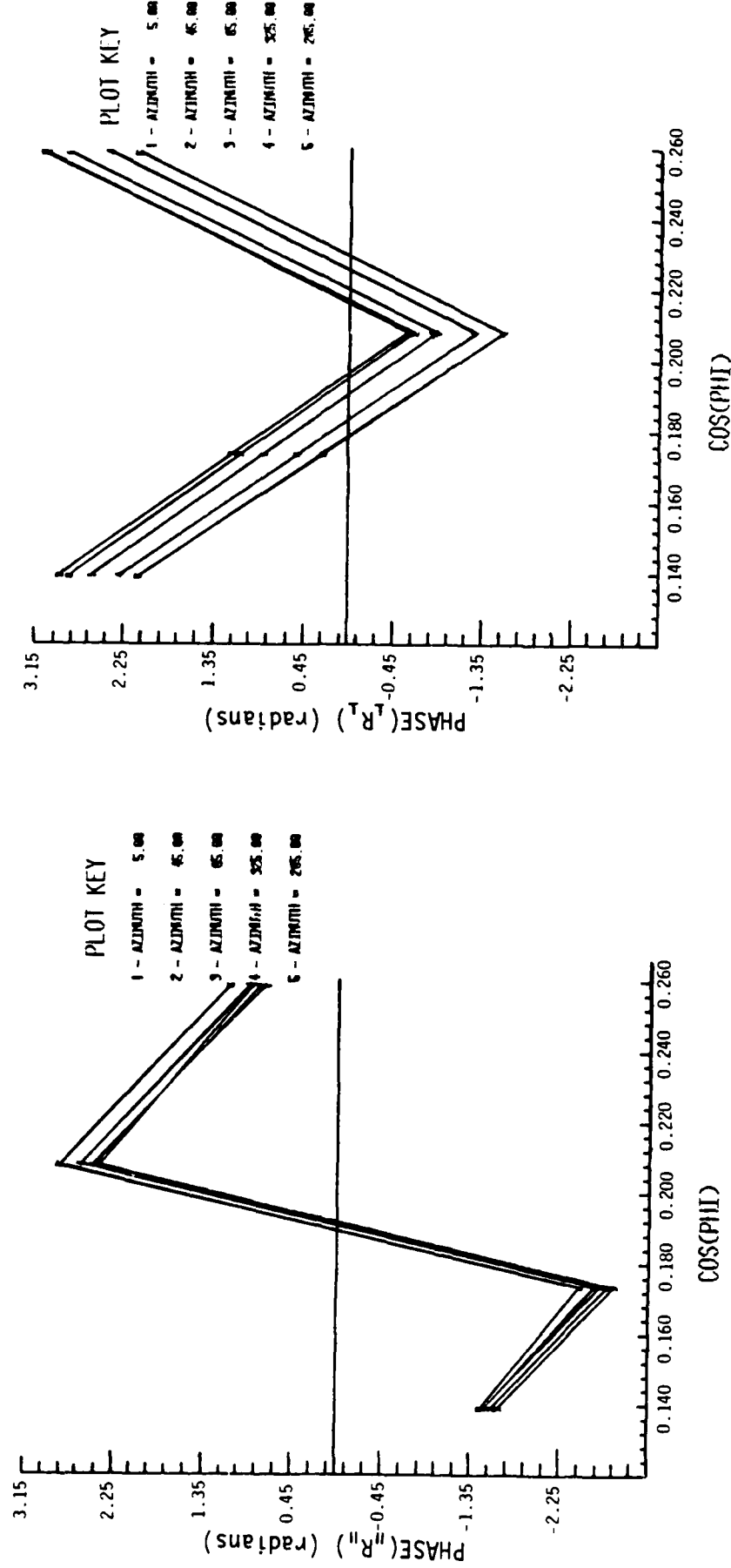


Figure 24. Phase of  $_{||}R_{||}$  and  $_{\perp}R_{\perp}$  for normal night, dip =  $70^{\circ}$ , and frequency = 27 kHz.

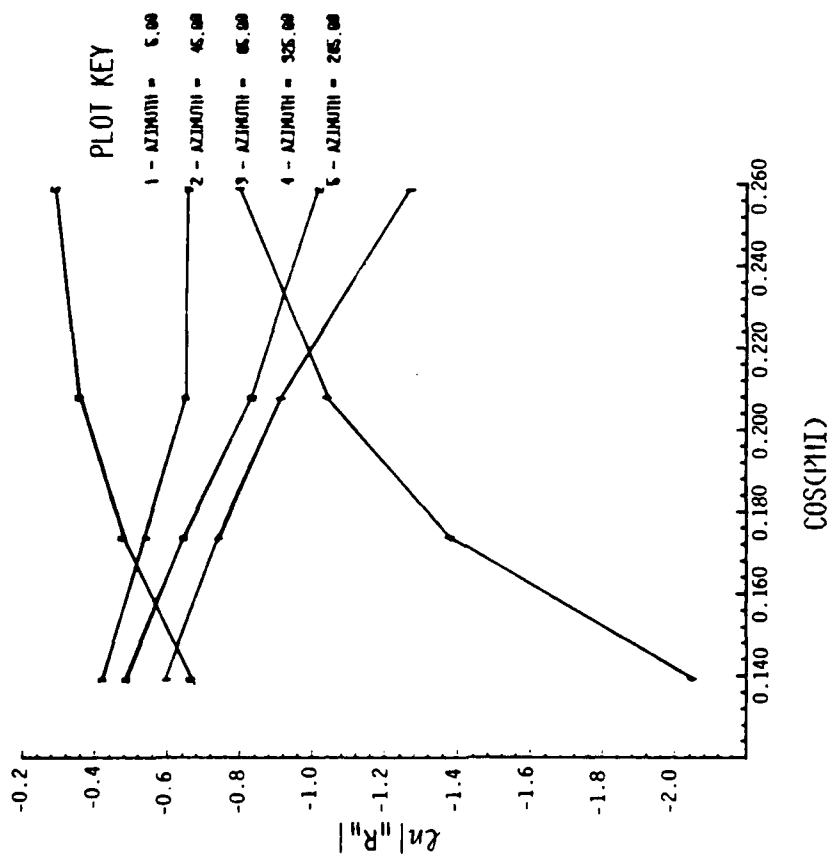
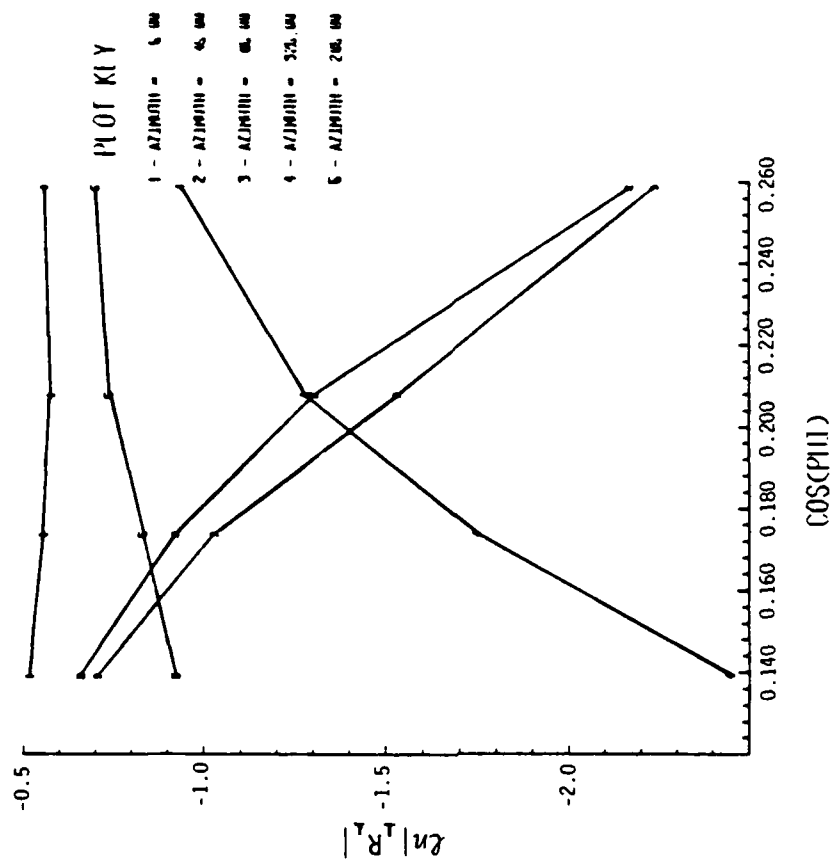


Figure 25. Magnitude of  ${}_{\parallel}R_{\parallel}$  and  ${}_{\perp}R_{\perp}$  for normal night, dip = 30°, and frequency = 27 kHz.

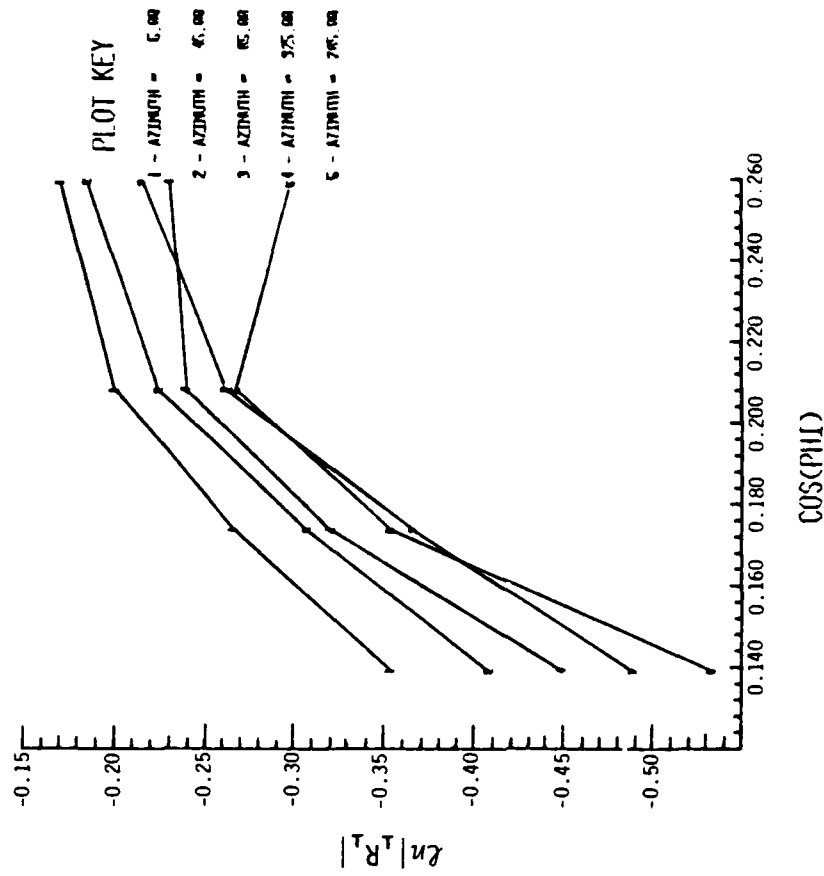
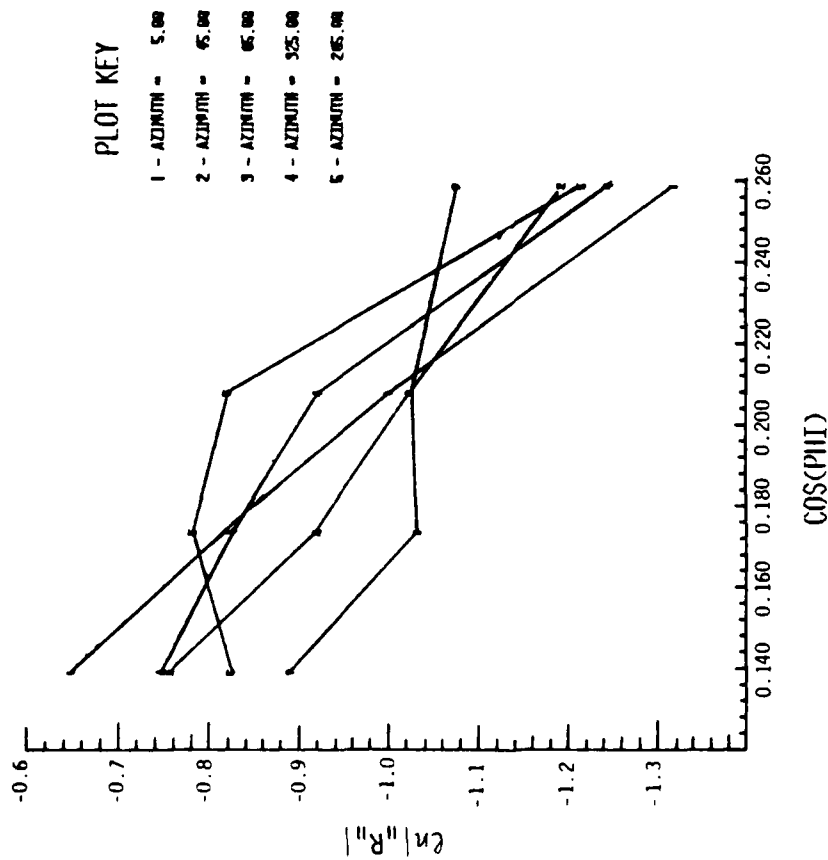


Figure 26. Magnitude of  $R_{||}$  and  $R_{\perp}$  for normal night, dip = 70°, and frequency = 40 kHz.

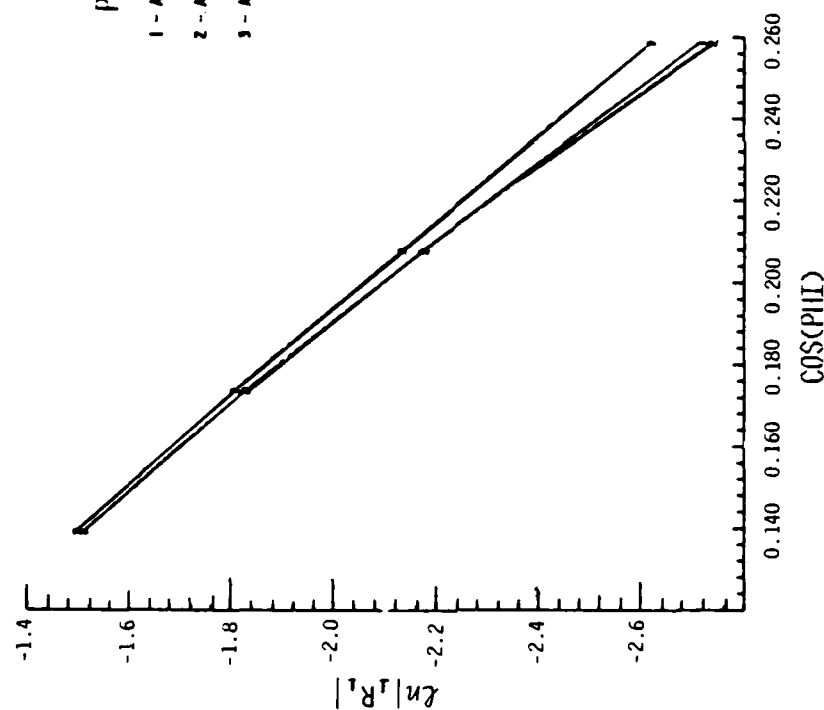
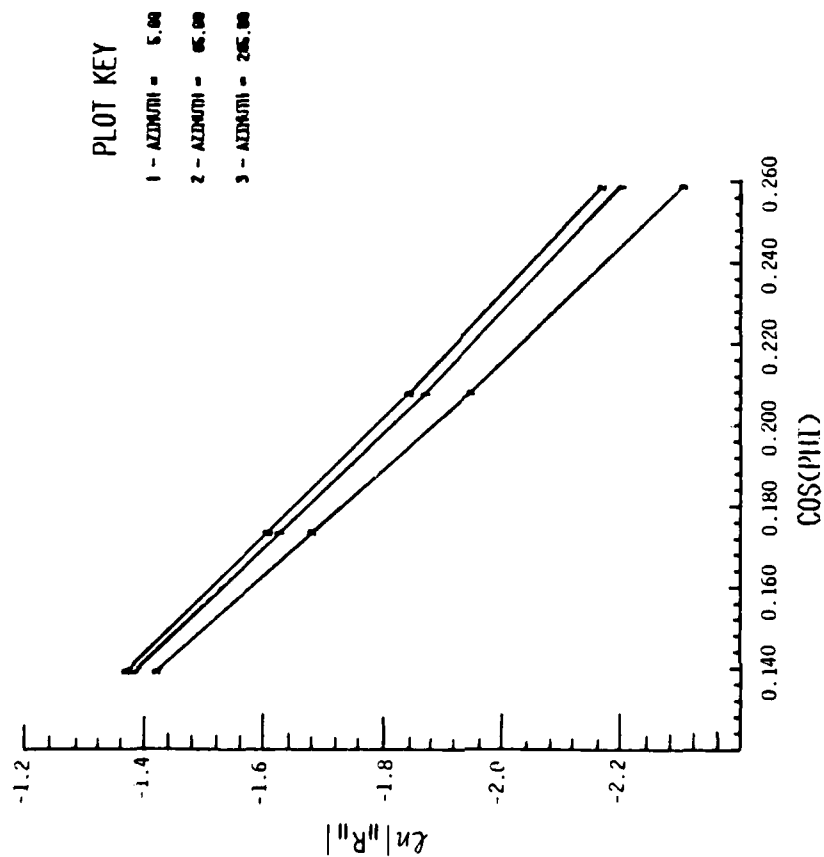


Figure 27. Magnitude of  ${}_{\parallel}R_{\parallel}$  and  ${}_{\perp}R_{\perp}$  for a moderate spread debris case for dip = 70°, frequency = 40 kHz.



The analytic form of the reflection coefficient, Equation 17, will be used in the revised WEDCOM. This permits a more efficient LF and VLF model simulation with little sacrifice in accuracy. Section 3.3 describes a procedure to eliminate unnecessary reflection coefficient computations if the ionospheric profile and anisotropy has changed negligibly. Reference 3 describes a reflection coefficient scaling procedure which is slightly modified here to account for anisotropic changes. When this scaling is used in conjunction with the analytic formulation just described, a first-order correction is made to the reflection coefficient for a slightly modified ionospheric profile. The simplicity of this scaling makes it desirable. However, as pointed out in Reference 3, this scaling works well only when the ionospheric profile to be scaled is very similar to the one for which the reflection coefficient was computed. This requirement should be satisfied by the Section 3.3 procedure. The susceptibility term, Equation 13, is assumed to behave exponentially in altitude with a scale-height  $H_x$  in the reflection region. The reflection coefficient for the new profile is scaled from the complex A and B of the present profile from

$$r_i(C_i) = \exp\left(A + B \frac{H_{xN}}{H_{xP}} C_i\right) \quad (18)$$

where

$H_{xN}$  = susceptibility scale-height for new profile

$H_{xP}$  = susceptibility scale-height for present profile.

This scaling procedure is empirical, but has its foundation in an analytic treatment of exponentially varying isotropic ionospheres described in Reference 12.

The analytic formulation (Equation 13) will not significantly reduce the computation time if a large number of iterative integration reflection coefficient computations (Section 3.1) are needed to determine the complex-valued A and B constants. Furthermore, the required number of computations vary as a function of the ionospheric environment and frequency. For this analysis the A and B constants were determined by first computing the reflection coefficients at two incidence angles and then solving for A and B. This procedure was noted to have several limitations, especially in accounting accurately for the  $2\pi$  ambiguities as noted in Figure 24. Also, the region of accuracy is unknown. These limitations were not important in the LF analysis, but became critical in the VLF study.

A more accurate procedure is to first determine the reflection coefficient (R) and its derivative ( $dR/dC_i$ ) at a specified incidence angle ( $C_i$ ). Then by noting that

$$B = \frac{dR/dC_i}{R} \quad (19)$$

after which A is easily evaluated, the phase ambiguity is eliminated. By computing B in this manner for one or two more  $C_i$ , the A's and B's can be compared to note the sensitivity. If needed, intermediate  $C_i$  computations are then made.

## SECTION 4

### VLF MODEL IMPROVEMENTS

#### 4.1 INTRODUCTION

The WEDCOM VLF model underwent a major revision from WEDCOM III to the present WEDCOM IV version. The most important improvement in WEDCOM IV was the addition of an anisotropic ionosphere capability, poorly approximated in the earlier model. This required a much larger computation time, however. For example, the older version computed only two (or three) ionospheric reflection coefficients for a normal nighttime case whereas the present version typically computes 36 to 50 values. The older version required only two or three values due to:

1. Use of an ionospheric reflection coefficient interpolation algorithm,
2. Fewer reflection coefficient segments.

The penalty of the older version was that the VLF predictions were not accurate for nighttime conditions. However, the older version provided accurate predictions for highly nuclear disturbed environments, and was not too much in error for normal daytime conditions.

In addition to the reflection coefficient computation, the WEDCOM IV procedure that determines the eigenangles is more sophisticated and also required more computation time than the earlier procedure. As the WEDCOM IV VLF model has been exercised, it has become apparent that the increased computation time is excessive for the objectives of WEDCOM, and at least a portion of this increased time is for a computational accuracy not needed for WEDCOM predictions. The alternative model modifications presented below suggest reductions in the computation time while retaining the needed accuracy and model capability.

Since WEDCOM IV, the VLF propagation model was revised for use in studies for the Naval Electronics System Command (Reference 2). The revision includes the addition of a more accurate computation for highly elevated antennas and a redefinition of the eigenangle search region. The first improvement is not necessary for the purposes of WEDCOM and will not be included. The second improvement which allows a reduction in the number of reflection coefficients needed is discussed in Section 4.2. Additional improvements were also made that provide the model increased capability.

For example, an improved mode convergence computation has been developed, and a variable path increment logic was added to reduce the number of computations.

There are two areas where large computation time requirements are needed for the VLF model:

1. The ionospheric reflection coefficient computation, and
2. The search for the eigenangles.

The reflection coefficient computation was addressed in Section 3, where an analytic formulation to reduce the time requirement was described. An improved criteria for when the computations are to be performed (also described in Section 3) will also reduce the computation time. The second area, the eigenangle search, becomes increasingly important as the number of eigenangles increase. Alternative procedures for eigenangle determinations are described in Sections 4.3 and 4.4.

The new path increment procedure outlined in Section 2.2 for the LF model will be utilized in the VLF model to determine the eigenangles.

#### 4.2      PROCEDURE TO REDUCE THE NUMBER OF REFLECTION COEFFICIENT COMPUTATIONS

WEDCOM IV used two techniques for determining the eigenvalues,  $\theta_n$  (see Reference 1). The search technique over the  $\theta$ -plane is the major user of computer time and is the one addressed here. It is an adaptation of the MODE SRCH algorithm (Reference 13). Figure 28 illustrates the WEDCOM IV method of search "boxes" where an ionospheric reflection coefficient computation is made at each corner (ie, for N boxes, there are 4N computations). This overlapping of the boxes assured that eigenvalues falling on the box edges would not be missed. Figure 28 illustrates the modified procedure which reduces the number of computations at least by 25 percent, but sometimes approaching 50 percent. In utilizing this procedure there were a few occasions when the eigenvalue did fall on a box edge and was not computed. For these few cases a special computation was made to determine the eigenangle, which worked satisfactorily for those exercises. For WEDCOM, a user interaction such as this is not practical and a simple procedure has been outlined (but not yet implemented) to eliminate this difficulty. In essence the search boxes will be slightly enlarged while retaining the same reflection coefficient locations. The duplication of an eigenvalue by this procedure will be automatically identified by the present WEDCOM IV algorithm.

An additional computation time-saving technique was implemented into the VLF model for the NESC studies. For cases where ionospheric conditions are identical

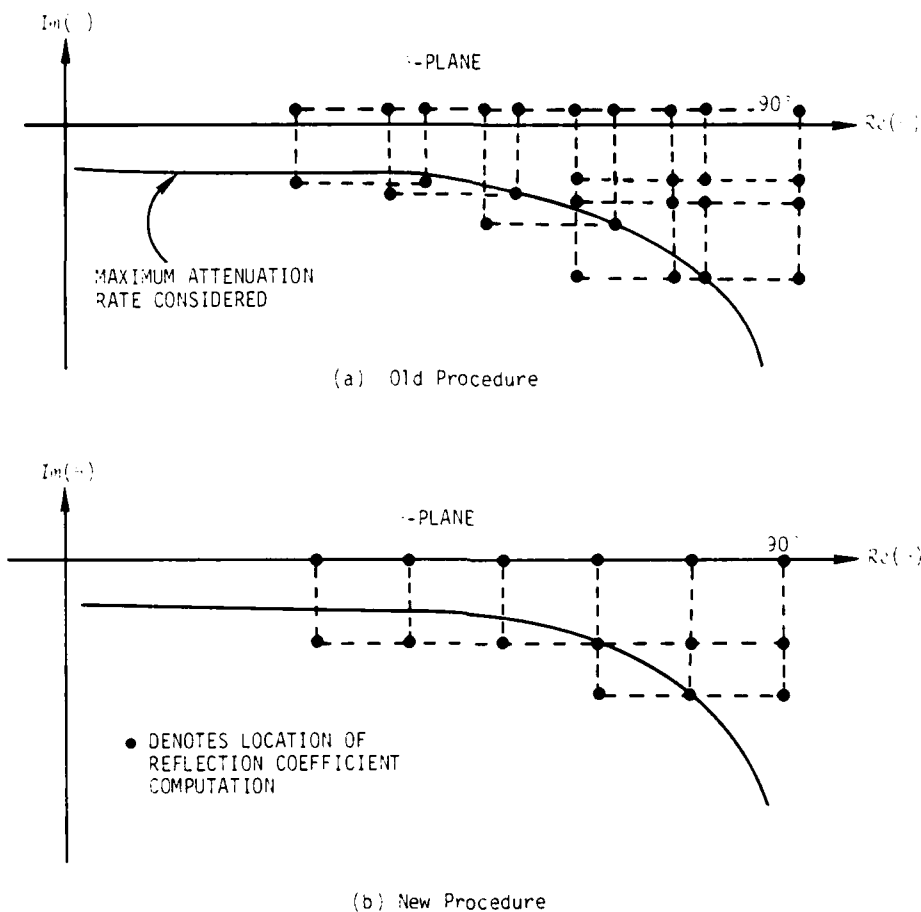


Figure 28. Comparison of new and WEDCOM IV procedures for determining  $\theta$ -plane reflection coefficient computations.

for adjacent path segments, but where the ground conductivity does change, the ionospheric reflection coefficients are not recomputed as was done in WEDCOM IV. The degree of computational time savings for this procedure is obviously case dependent.

#### 4.3 PRECOMPUTED EIGENANGLES

A recent effort (Reference 3) created an eigenangle data base for normal and disturbed environments from which needed eigenangles were obtained through interpolation and scaling algorithms. From this procedure, extremely fast evaluations (even compared to the WEDCOM III model) are possible. The amount of subroutine support is a very small fraction of WEDCOM IV. The price for this efficiency, however, is an immense data file and a computational accuracy below the WEDCOM standards.

The most difficult and time consuming eigenangle evaluations occur near normal nighttime. A proposed technique is to have a precomputed data file only for this case. Alternative methods would be used for all other cases. The data file

would still be very large but would be manageable. The data base could be generated by two procedures:

1. Precomputed and furnished with the WEDCOM Fortran tape.
2. A separate computation performed by the user.

Initially, the first procedure may seem the simpler. However, experience with this procedure has indicated frequent difficulty with the data tape and an inconvenience in generating a new tape when model modifications are required. The second procedure is favored at the present, where a separate driver would be furnished to the user. This would also allow the data to better conform to the user needs.

#### 4.4 EIGENANGLE DETERMINATION USING ANALYTIC REFLECTION COEFFICIENT FORMULATION AND INITIAL EIGENANGLE ESTIMATES

The mode search model used in WEDCOM IV to find an initial value for the eigenangle solution requires significant calculation time, particularly for lightly-disturbed, nighttime conditions. In WEDCOM III analytic approximations were used for the initial eigenangles. A preliminary study has been made to see if a similar procedure (using the analytic form for the reflection coefficient described in Section 3) can be used to replace the mode search model. A summary of the eigenangle approximations follow. Each approximation applies to one of three easily identifiable eigenvalue types. The eigenangle,  $\theta_N$ , is defined at altitude  $H_R$ .

##### 4.4.1 Quasi-Flat Earth Modes

$$C_i = \left[ (C_i)^2 + \frac{H_R}{a} \right]^{1/2} = \cos \theta_N \quad (20)$$

where

$$C'_i = R_N \left\{ 2.0kH_R - jB \left[ 1.0 + 4.0 H_R (kH_R)^2 / (aR_N^2) \right]^{1/2} \right\} / \left\{ 4.0(kH_R)^2 + B^2 \right\} \quad (21)$$

$$R_N = \begin{cases} 2.0\pi N - jA & \text{(vertical polarization)} \\ \pi(2.0N + 1.0) - jA & \text{(horizontal polarization)} \end{cases} \quad (22)$$

$N$  is the mode number, and  $k$ ,  $a$ ,  $H_R$ ,  $A$ , and  $B$  were defined in Section 3.

##### 4.4.2 Earth-Grazing Modes

$$C_i = \left[ C'_i + \chi_a \right]^{1/2} = \cos(\theta_N) \quad (23)$$

where

$$x_a = \left( \frac{2.0H_R}{a} \right)^{1/2}$$

$$C'_i = \left\{ R_N - (2.0ka/3.0)x_a^3 - jBx_a \right\} / \left\{ k_a x_a + j \frac{B/2.0}{x_a} \right\} \quad (24)$$

$$R_N = \begin{cases} \pi(12.0N + 1.0)/6.0 - jA & \text{(vertical polarization)} \\ \pi(12.0N + 6.0)/6.0 - jA & \text{(horizontal polarization)} \end{cases} \quad (25)$$

#### 4.4.3 Whispering-Gallery Modes

$$C_i = \left[ C'_i + x_a^2 \right]^{1/2} = \cos(\theta_N) \quad (26)$$

where

$$C'_i = x_2 \left\{ 1.0 - x_2 \left( j \frac{B/2.0}{x_a^2} - k_a \right) / \left( k_a x_a + j \frac{B/2.0}{x_a} \right) \right\} \quad (27)$$

$$x_2 = \left\{ R_N - (2.0k_a/3.0)x_a^3 - jBx_a \right\} / \left\{ k_a x_a + j \frac{B/2.0}{x_a} \right\} \quad (28)$$

$$R_N = \pi(4.0N + 1)/2.0 - jA \quad (29)$$

Note that the values of A and B will differ dependent on the polarization. Infinite earth conductivity is assumed in the above approximations. The best eigenvalue approximation is selected based on its type. Then an iteration procedure, using the isotropic definition of the model solution, is used to improve the approximation sensitivity to the actual earth conductivity. The resulting eigenvalue approximation is iterated to a final exact solution using the anisotropic model solution.

In WEDCOM IV the reflection coefficients for an isotropic ionosphere are used (earth-curvature and magnetic field effects are ignored). In the new model the approximate eigenangle formulations will retain the isotropic ionosphere assumption, but will use anisotropic reflection coefficients. Figure 29 is reproduced from Reference 1 and demonstrates how the approximate isotropic procedure is usually accurate for daytime and strong nuclear depressed ionospheres. As a normal nighttime

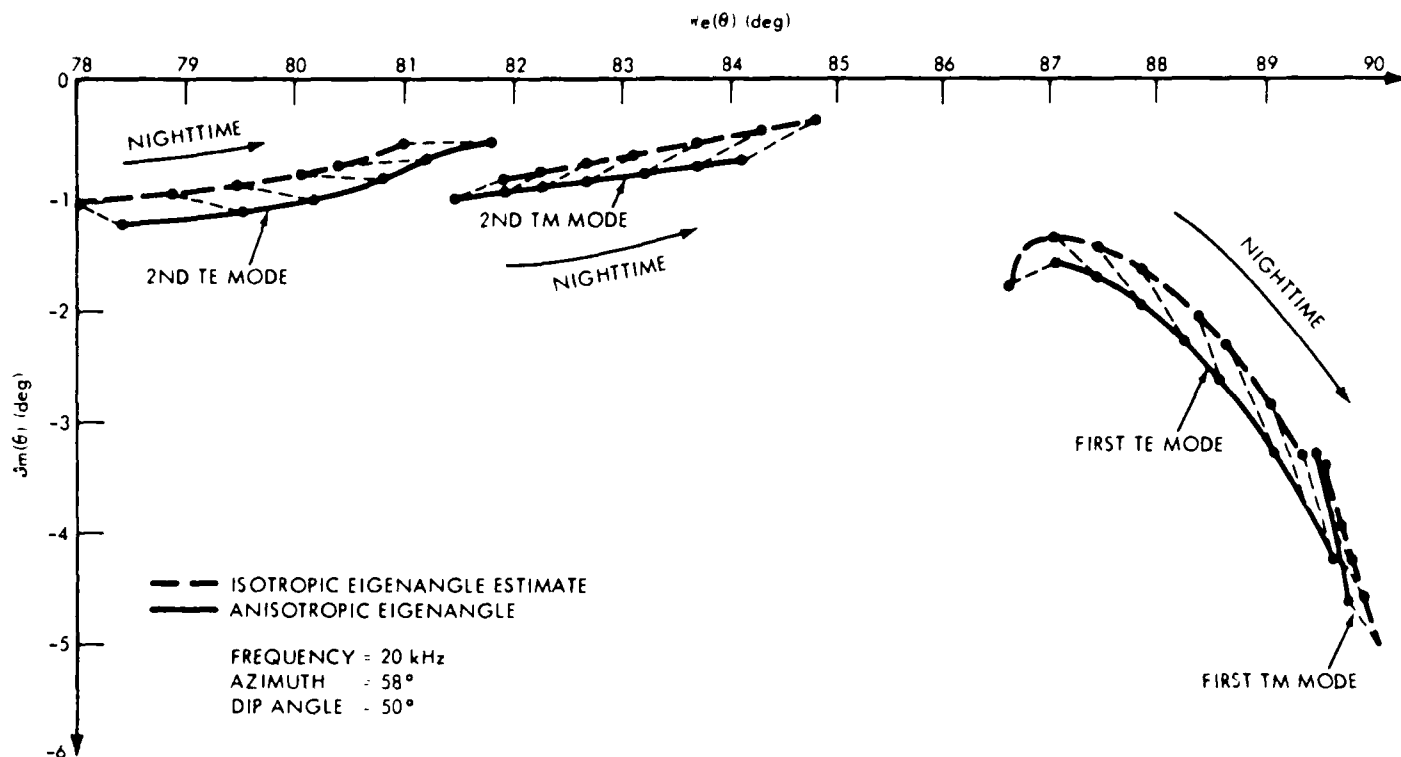


Figure 29. Loci of eigenangles for the approximate isotropic and exact anisotropic procedures.

is approached the first TE and TM modes converge. Figure 29 also shows why the older analytic formulation had a built-in distortion. The ionosphere reflection coefficients used as data points for the isotropic analytic formulation are computed along the real  $\theta$  axis (this is also the case for the LF model). Especially for the lower-ordered modes the eigenangles are not near the real-axis (and thus not near the data points). For the model effort described here, complex valued  $\theta$  were used as data points. The imaginary part of the  $\theta$  value was selected to correspond to 1 dB/Mm absorption.

The new formulation has had limited testing. A normal daytime case was executed and resulted in significant computation efficiency compared to WEDCOM IV, and had surprisingly good accuracy. A normal nighttime case (the more interesting and difficult case) was then exercised. For this case the approximate eigenangle did not always provide an accurate estimate for proper convergence in the anisotropic solution. Several factors contributed to this:

1. One or both first-order modes sometimes switch polarization.
2. The analytic formulation of the ionosphere were not correct.



3. The isotropic mode solution did not sufficiently approximate the anisotropic solution.

At this time the second item appears to be the most dominant problem. The reflection coefficient phase values were not always correct leading to erroneous approximations. An improved procedure to correct this has been outlined. An alternate procedure has also been outlined to address the other two difficulties. Briefly, this procedure "iterates" from the approximate value (with its model equation) to the actual eigenvalue (with the polarizations and anisotropy of the actual model equation). This requires additional calculation time, however, and must be evaluated in comparison to the precomputed eigenvalue procedure (Section 4.3).

## SECTION 5

### ELF PROPAGATION MODEL

#### 5.1 GENERAL

The ELF propagation model currently in the WEDCOM code is essentially the same as the Naval Ocean Systems Center (NOSC) model described by Pappert and Moler (Reference 14). In this model mode solutions for propagation in the earth-ionosphere waveguide are found. Waveguide variability along the great circle propagation path is accounted for (WKB approximation) but variability normal to the great circle path is neglected. Allowance is made for propagation over both the short and long great circle paths.

The iterative Newton-Raphson method is used to find the mode solution. The solution is started with a guess for the eigenangle. Only one mode propagates at ELF and it has been found that almost any reasonable initial guess for the eigenangle will result in convergence. A significant part of the mode solution in terms of computation time is the calculation of the reflection coefficient matrix. The matrix is found from a numerical integration of differential equations defined by Budden (Reference 15). For ELF the integration must start at fairly high altitudes (about 200 km for ambient nighttime conditions) and this increases the computation time over that for VLF and LF calculations where the integration can be started below 100 km.

Recently, Booker (Reference 16) has proposed an approximate model for ELF propagation that combines theoretical work of Booker and Lefeuvre (Reference 17) and Griefinger and Griefinger (References 18 and 19). The model is based on dividing the atmosphere into regions where the local vertical gradient is large in comparison to the local wavelength and regions where it is small in comparison to the local wavelength. In regions where the gradient is small the phase integral method is used to determine propagation. Regions where the gradient is high are replaced with a discontinuity equal to the difference in refractive indices at the top and bottom of the region. Up to five reflection regions can be defined to account for reflections from the D and E regions. Reflections from the discontinuities are combined using the phase change between the reflection regions (phase change in regions where phase integral method is applicable). As described by Booker phase and group propagation below the bottom of the ionosphere is practically horizontal while phase propagation

above the bottom of the ionosphere is practically vertical. The bottom of the ionosphere is defined by a complex height. The positive imaginary part is a measure of the absorption experienced in the lowest layer of the ionosphere.

The approximate model requires between 1/10 and 1/5 the computation time required by the detailed numerical model. This significant reduction in computation time will allow useful system analyses for conditions that are too expensive with the current WEDCOM code.

## 5.2 BOOKER MODEL

A detailed description of the model developed by Booker is given in Reference 16. The following summarizes the computational steps and principal equations. Calculations are made for both the ordinary (O) and extraordinary (X) waves. Subscripts identify quantities for the O and X waves when results for both waves are combined.

### 5.2.1 Evaluate the Heights of Reflection

The reflection heights are determined as the heights where

$$\frac{\lambda}{2\pi|n|h} = \gamma \quad (30)$$

where

$\lambda$  = free-space wavelength

$n$  = complex index of refraction for vertical propagation

$h = |1/n^2 - 1 \, d/dz \, (n^2 - 1)|^{-1}$

and  $\gamma$  is a quantity that is a function of the refractive index phase angle (given graphically in Reference 16). For most conditions  $\gamma$  can be taken as 2 for the O wave and 2.57 for the X wave. Up to five reflection heights can be computed for the O wave ( $h_{10}$ ,  $h_{20}$ ,  $h_{30}$ ,  $h_{40}$ , and  $h_{50}$ ) and the X wave ( $h_{1X}$ ,  $h_{2X}$ ,  $h_{3X}$ ,  $h_{4X}$ , and  $h_{5X}$ ).

The complex index of refraction indices are found from

$$\left. \begin{matrix} n_0^2 \\ n_X^2 \end{matrix} \right\} = (1 + \kappa_L) \frac{1 + \kappa_T - \kappa_H \left\{ \frac{1}{2} \tau \cos^2 I \mp \left( \frac{1}{4} \tau^2 \cos^4 I - \sin^2 I \right)^{1/2} \right\}}{(1 + \kappa_L) - (\kappa_L - \kappa_T) \cos^2 I} \quad (31)$$

where

$$\tau = \frac{(1 + \kappa_T)(\kappa_L - \kappa_T) - \kappa_H^2}{\kappa_H(1 + \kappa_L)}$$

$I$  = magnetic dip angle (negative in northern hemisphere).

The longitudinal, transverse, and Hall susceptibilities are given by

$$\kappa_L = -\frac{1}{\omega^2} \Sigma \Omega_N^2 \quad (32)$$

$$\kappa_T = \Sigma \frac{\Omega_N^2}{\Omega_M^2 - \omega^2} \quad (33)$$

$$\kappa_H = \frac{1}{j\omega} \Sigma \frac{\Omega_N^2 \Omega_M}{\Omega_M^2 - \omega^2} \quad (34)$$

where

$$\Omega_{Ne}^2 = \frac{\omega_{Ne}^2}{1 - j \frac{\nu_e}{\omega}}$$

$$\Omega_{Nm+}^2 = \frac{\omega_{Nm+}^2}{1 - j \frac{\nu_i}{\omega}}$$

$$\Omega_{Nm-}^2 = \frac{\omega_{Nm-}^2}{1 - j \frac{\nu_i}{\omega}}$$

$$\Omega_{Me} = \frac{\omega_{Me}}{1 - j \frac{\nu_e}{\omega}}$$

$$\Omega_{Mm+} = \frac{\omega_{Mm+}}{1 - j \frac{\nu_i}{\omega}}$$

$$\Omega_{Mm-} = \frac{\omega_{Mm-}}{1 - j \frac{\nu_i}{\omega}}$$

$$\omega_{Ne}^2 = 3.18 \times 10^9 N_e$$

$$\omega_{Nm+}^2 = 5.98 \times 10^4 N_+$$

$$\omega_{Nm-}^2 = 5.98 \times 10^4 N_-$$

$$\omega_{Me} = -1.76 \times 10^7 B$$

$$\omega_{Mm+} = 3.3 \times 10^2 B$$

$$\omega_{Mm-} = -3.3 \times 10^2 B$$

$$N_e = \text{electron density (cm}^{-3}\text{)}$$

$$N_+ = \text{positive ion density (cm}^{-3}\text{)}$$

$$N_- = \text{negative ion density (cm}^{-3}\text{)}$$

$$B = \text{magnetic field strength (gauss)}$$

$$\nu_e = \text{electron-neutral collision frequency (s}^{-1}\text{)}$$

$$\nu_i = \text{ion-neutral collision frequency (s}^{-1}\text{)}.$$

Positive and negative atomic ions can also be included in the susceptibility terms but are neglected in the ELF calculations. For computational purposes, Equation 31 is rewritten as (Reference 20)

$$\left. \begin{matrix} n_0^2 \\ n_x^2 \end{matrix} \right\} = \frac{-\gamma \mp S^{1/2}}{2\alpha} \quad (35)$$

where

$$\gamma = -2(1 + \kappa_L)(1 + \kappa_T) + \left( (1 + \kappa_T)(\kappa_L - \kappa_T) - \kappa_H^2 \right) \cos^2 I$$

$$S = \gamma^2 - 4\alpha\epsilon$$

$$\alpha = 1 + \kappa_L - (\kappa_L - \kappa_T) \cos^2 I$$

$$\epsilon = (1 + \kappa_L) \left( (1 + \kappa_T)^2 + \kappa_H^2 \right)$$

### 5.2.2 Calculate the Complex Index of Refraction Indices at the Reflection Heights

The equations given in Section 5.2.2 are used to compute the indices. The

electron and ion densities and collision frequencies at the reflection heights are found by interpretation (see Section 5.2.7).

### 5.2.3 Calculate the Complex Elliptical Polarization at the Reflection Heights

The polarization ratios are computed from

$$Q = \frac{\sin I \sin \Delta - Q_1 \cos \Delta - Q_2 \cos I \sin \Delta}{\sin I \cos \Delta + Q_1 \sin \Delta - Q_2 \cos I \cos \Delta} \quad (56)$$

where

$$Q_1 = \frac{\kappa_H}{n^2 - 1 - \kappa_T}$$

$$Q_2 = \frac{n^2 \cos I \sin I}{n^2 \cos^2 I - 1 - \kappa_L}$$

$\Delta$  = angle-of-propagation east of magnetic north.

The complex elliptical polarization ratios are essentially the same at each reflection altitude:

$$Q_0 = Q_{i0}, \quad i = 1, 5 \quad (57)$$

$$Q_X = Q_{iX}, \quad i = 1, 5 \quad (58)$$

### 5.2.4 Calculate the Equivalent Complex Heights of Reflection

The equivalent height of reflection is computed from

$$\tilde{Z}_R = Z_1 + \frac{\lambda}{2\pi} \frac{n_2 n_4}{n_1 n_3 n_5} \frac{B - jA}{D + jC} \quad (59)$$

where

$$\begin{aligned}
A = & \cos \phi_{12} \cos \phi_{23} \cos \phi_{34} \cos \phi_{45} \\
& - \frac{1}{n_4} \cos \phi_{12} \cos \phi_{23} \sin \phi_{34} \sin \phi_{45} \\
& - \frac{1}{n_2} \sin \phi_{12} \sin \phi_{23} \cos \phi_{34} \cos \phi_{45} \\
& + \frac{1}{n_2 n_4} \sin \phi_{12} \sin \phi_{23} \sin \phi_{34} \sin \phi_{45} \\
& - n_3 \cos \phi_{12} \sin \phi_{23} \sin \phi_{34} \cos \phi_{45} \\
& - \frac{n_3}{n_4} \cos \phi_{12} \sin \phi_{23} \cos \phi_{34} \sin \phi_{45} \\
& - \frac{n_3}{n_2} \sin \phi_{12} \cos \phi_{23} \sin \phi_{34} \cos \phi_{45} \\
& - \frac{n_3}{n_2 n_4} \sin \phi_{12} \cos \phi_{23} \cos \phi_{34} \sin \phi_{45}
\end{aligned}$$

$$\begin{aligned}
B = & n_5 \cos \phi_{12} \cos \phi_{23} \cos \phi_{34} \sin \phi_{45} \\
& + \frac{n_5}{n_4} \cos \phi_{12} \cos \phi_{23} \sin \phi_{34} \cos \phi_{45} \\
& - \frac{n_5}{n_2} \sin \phi_{12} \sin \phi_{23} \cos \phi_{34} \sin \phi_{45} \\
& - \frac{n_5}{n_2 n_4} \sin \phi_{12} \sin \phi_{23} \sin \phi_{34} \cos \phi_{45} \\
& - n_3 n_5 \cos \phi_{12} \sin \phi_{23} \sin \phi_{34} \sin \phi_{45} \\
& + \frac{n_3 n_5}{n_4} \cos \phi_{12} \sin \phi_{23} \cos \phi_{34} \cos \phi_{45} \\
& - \frac{n_3 n_5}{n_2} \sin \phi_{12} \cos \phi_{23} \sin \phi_{34} \sin \phi_{45} \\
& + \frac{n_3 n_5}{n_2 n_4} \sin \phi_{12} \cos \phi_{23} \cos \phi_{34} \cos \phi_{45}
\end{aligned}$$

$$\begin{aligned}
C = & \frac{n_2 n_4}{n_3 n_5} \sin \phi_{12} \cos \phi_{23} \cos \phi_{34} \cos \phi_{45} \\
& - \frac{n_2}{n_3 n_5} \sin \phi_{12} \cos \phi_{23} \sin \phi_{34} \sin \phi_{45} \\
& + \frac{n_4}{n_3 n_5} \cos \phi_{12} \sin \phi_{23} \cos \phi_{34} \cos \phi_{45} \\
& - \frac{1}{n_3 n_5} \cos \phi_{12} \sin \phi_{23} \sin \phi_{34} \sin \phi_{45} \\
& - \frac{n_2 n_4}{n_5} \sin \phi_{12} \sin \phi_{23} \sin \phi_{34} \cos \phi_{45} \\
& - \frac{n_2}{n_5} \sin \phi_{12} \sin \phi_{23} \cos \phi_{34} \sin \phi_{45} \\
& + \frac{n_4}{n_5} \cos \phi_{12} \cos \phi_{23} \sin \phi_{34} \cos \phi_{45} \\
& + \frac{1}{n_5} \cos \phi_{12} \cos \phi_{23} \cos \phi_{34} \sin \phi_{45}
\end{aligned}$$

$$\begin{aligned}
C = & - \frac{n_2 n_4}{n_3} \sin \phi_{12} \cos \phi_{23} \cos \phi_{34} \sin \phi_{45} \\
& - \frac{n_2}{n_3} \sin \phi_{12} \cos \phi_{23} \sin \phi_{34} \cos \phi_{45} \\
& - \frac{n_4}{n_3} \cos \phi_{12} \sin \phi_{23} \cos \phi_{34} \sin \phi_{45} \\
& - \frac{1}{n_3} \cos \phi_{12} \sin \phi_{23} \sin \phi_{34} \cos \phi_{45} \\
& + n_2 n_4 \sin \phi_{12} \sin \phi_{23} \sin \phi_{34} \sin \phi_{45} \\
& - n_2 \sin \phi_{12} \sin \phi_{23} \cos \phi_{34} \cos \phi_{45} \\
& - n_4 \cos \phi_{12} \cos \phi_{23} \sin \phi_{34} \sin \phi_{45} \\
& - \cos \phi_{12} \cos \phi_{23} \cos \phi_{34} \cos \phi_{45}
\end{aligned}$$



The complex phase changes are given by:

$$\Phi_{12} = (2\pi/\lambda) \int_{z_1}^{z_2} n dz \quad , \quad (40)$$

$$\Phi_{23} = (2\pi/\lambda) (z_3 - z_2) \quad (41)$$

$$\Phi_{34} = (2\pi/\lambda) \int_{z_3}^{z_4} n dz \quad (42)$$

$$\Phi_{45} = (2\pi/\lambda) (z_5 - z_4) \quad . \quad (43)$$

#### 5.2.5 Calculate the Equivalent Complex Height of the Bottom of the Ionosphere

The equivalent height of the bottom of the ionosphere is computed from

$$\tilde{z}_B = \int_0^{z_1} \frac{dz}{n^2} \quad . \quad (44)$$

#### 5.2.6 Calculate the Phase Velocity and Attenuation Rate

The phase velocity and attenuation rate are computed from

$$\frac{c}{v} = R(S) \quad (45)$$

$$\alpha = - \frac{2\pi}{\lambda} I(S) \quad (46)$$

where  $R(S)$  and  $I(S)$  are the real and imaginary parts of  $S$  and  $S$  is given by

$$S = \left[ \frac{Q_0^{-1} - Q_X^{-1}}{Q_0^{-1} \frac{\tilde{z}_{BO}}{\tilde{z}_{RO}} - Q_X^{-1} \frac{\tilde{z}_{BX}}{\tilde{z}_{RX}}} \right] \quad . \quad (47)$$

### 5.2.7 Interpolation and Calculation of Derivatives

In computing the reflection heights it is necessary to determine the magnitude and height-derivatives of electron and ion densities, collision frequencies, and magnetic field strength. As pointed out by Booker, confusion results if there are discontinuities in the magnitude or derivatives of any of the quantities. In choosing the electron and ion density profiles Booker used a method he developed (Reference 21) of fitting the profile with exponential fits between selected altitudes (transition altitudes) and then using smoothing functions at the transition altitudes that smooth the profile over a prescribed scale length. The relation for electron and ion density presented by Booker is

$$\ln N(z) = \ln N_r + A_{0,1}(z - z_r) + \sum_{n=1}^m (A_{n,n+1} - A_{n-1,n}) * \left\{ f(z - z_r, B_n) - f(z_r - z_n, B_n) \right\} \quad (48)$$

where

$$\begin{aligned} z &= \text{altitude} \\ z_n &= \text{transition altitudes used to describe electron density} \\ A_{n,n+1} &= \text{slope of } \ln N(z) \text{ versus } z \text{ for } z_n < z < z_{n+1} \\ B_n &= \text{reciprocal of smoothing scale used at transition altitudes} \\ f(z, B) &= \begin{cases} B^{-1} \ln \{ 1 + \exp(Bz) \} & zB < 100 \\ z & zB \geq 100 \end{cases} \\ N_r &= N(z_r) \\ z_r &= \text{reference altitude.} \end{aligned}$$

For use in the WEDCOM code where electron and ion densities profiles are computed as a function of nuclear radiation it is convenient to use Booker's formula-tion as an interpolation procedure. This can be done by choosing the smoothing scales so that the effects of fitting outside the interpolation region are negligible within the interpolation region. A 4-point interpolation is used by choosing the smoothing scale so that the profile within each altitude interval is determined by the exponential fits for the interval and for the adjacent altitude intervals. Thus for,

$$B_n \geq \frac{3}{z_{n+1} - z_n} \quad (49)$$

$N(z)$  between  $z_2$  and  $z_3$  is given by

$$\begin{aligned} \ln[N(z)] &= \ln[N_r] + A_1(z - z_r) \\ &+ (A_2 - A_1) \left\{ f(z - z_2, B_2) - f(z_r - z_2, B_2) \right\} \\ &+ (A_3 - A_2) \left\{ f(z - z_3, B_3) - f(z_r - z_3, B_3) \right\} \quad z_2 \leq z \leq z_3 \quad (50) \end{aligned}$$

where

$$A_1 = \frac{\ln \left[ \frac{N(z_2)}{N(z_1)} \right]}{z_2 - z_1}$$

$$A_2 = \frac{\ln \left[ \frac{N(z_3)}{N(z_2)} \right]}{z_3 - z_2}$$

$$A_3 = \frac{\ln \left[ \frac{N(z_4)}{N(z_3)} \right]}{z_4 - z_3}$$

$$N_r = N(z_1)$$

$$z_r = z_1$$

The derivative of  $N(z)$  can be obtained from

$$\begin{aligned} \frac{dN(z)}{dz} &= N(z) \left\{ A_1 + \frac{A_2 - A_1}{1 + \exp[-(z - z_2)B_2]} \right. \\ &\quad \left. + \frac{A_3 - A_2}{1 + \exp[-(z - z_3)B_3]} \right\} \quad (51) \end{aligned}$$

### 5.3 EVALUATION OF BOOKER MODEL

#### 5.3.1 Comparison with Results Presented by Booker and Behrooz-Toasi

Selected comparisons were made with model results presented in Reference 16 to verify that the implementation of the Booker model was correct. Figures 30 through 33 show comparisons of results for phase velocity and attenuation rate for quiet ionosphere profiles. The small differences are due to the different methods used for interpolation and to compute derivatives. Comparison of the results at 75 degrees north latitude with detailed calculations by NOSC are given in Reference 16. The results are in excellent agreement.

#### 5.3.2 Comparison with Selected NOSC Results

Calculations with the Booker model were also made for selected profiles where detailed NOSC results were available. The profiles selected include day and night quiet ionosphere profiles currently used in the WEDCOM IV code, day and night quiet ionosphere profiles used by NOSC in Reference 14, and a profile representative of moderate nuclear ionization. Tables 4 through 8 show the electron and positive ion densities and collision frequencies used.

Tables 9 and 10 show a comparison of the phase velocity and attenuation rate obtained with the Booker model and with the detailed NOSC model. Calculations were made at 70-degrees magnetic north latitude (80-degrees magnetic dip angle). There is good agreement between the models except for nighttime conditions where the Booker model overestimates the attenuation rate. The cause of this difference is still under investigation.

### 5.4 CALCULATION OF EXCITATION AND HEIGHT-GAIN FACTORS

In order to compute electric and magnetic field strengths it is necessary to specify excitation and height-gain factors. The height-gain factors for a vertical dipole launch, end-on launch, and broadside launch from a horizontal dipole are (Reference 14)

$$e_V = 2 \quad (52)$$

$$e_B = \frac{2C}{N_g} \quad (53)$$

$$e_E = \frac{2}{N_g} \quad (54)$$

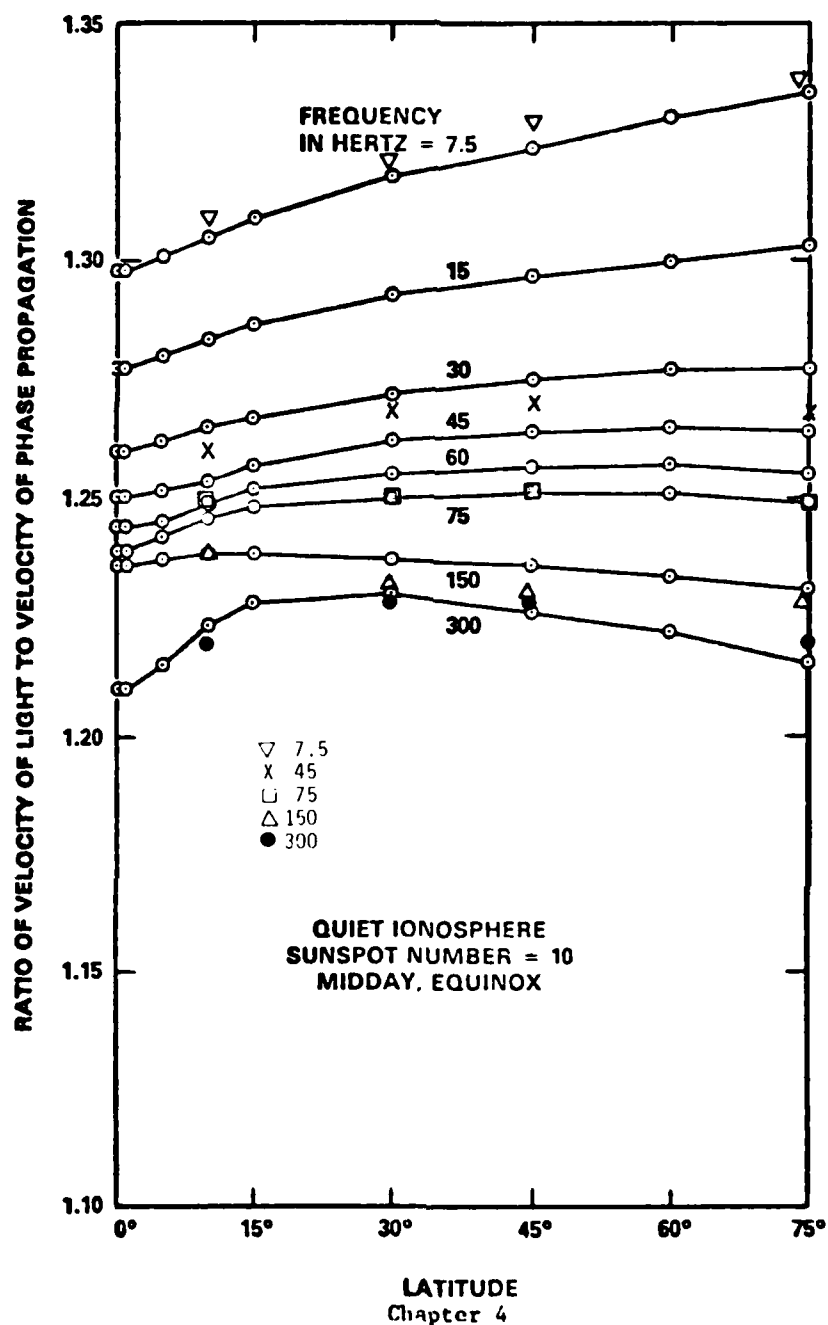


Figure 30. Illustrating the variation of the velocity of phase propagation with latitude and frequency under daytime conditions. Solid curves reproduced from Reference 16. Symbols indicate values obtained with Booker's model at Tempo.

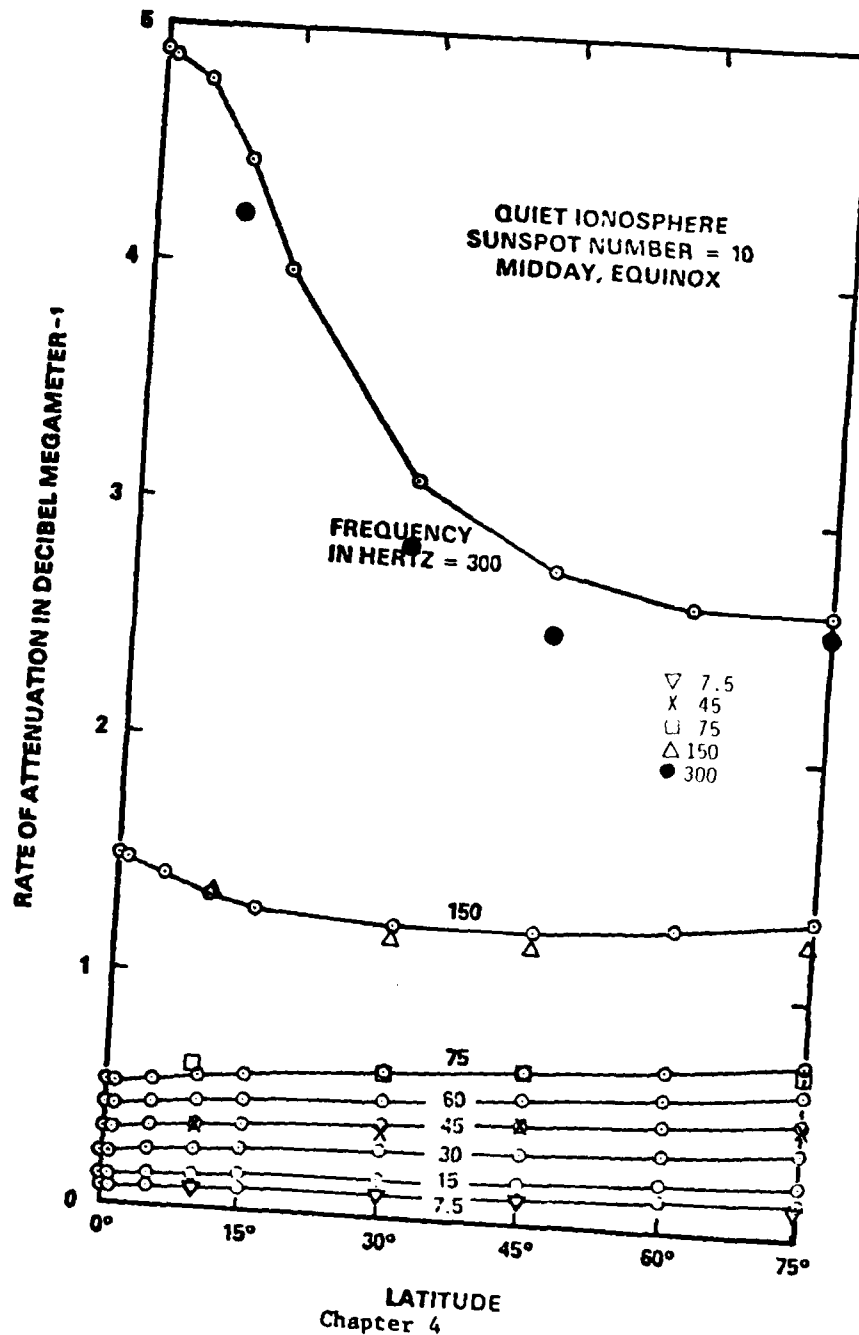


Figure 31. Illustrating the variation of the rate of attenuation with latitude and frequency under daytime conditions. Solid curves reproduced from Reference 16. Symbols indicate values obtained with Booker's model at Tempo.

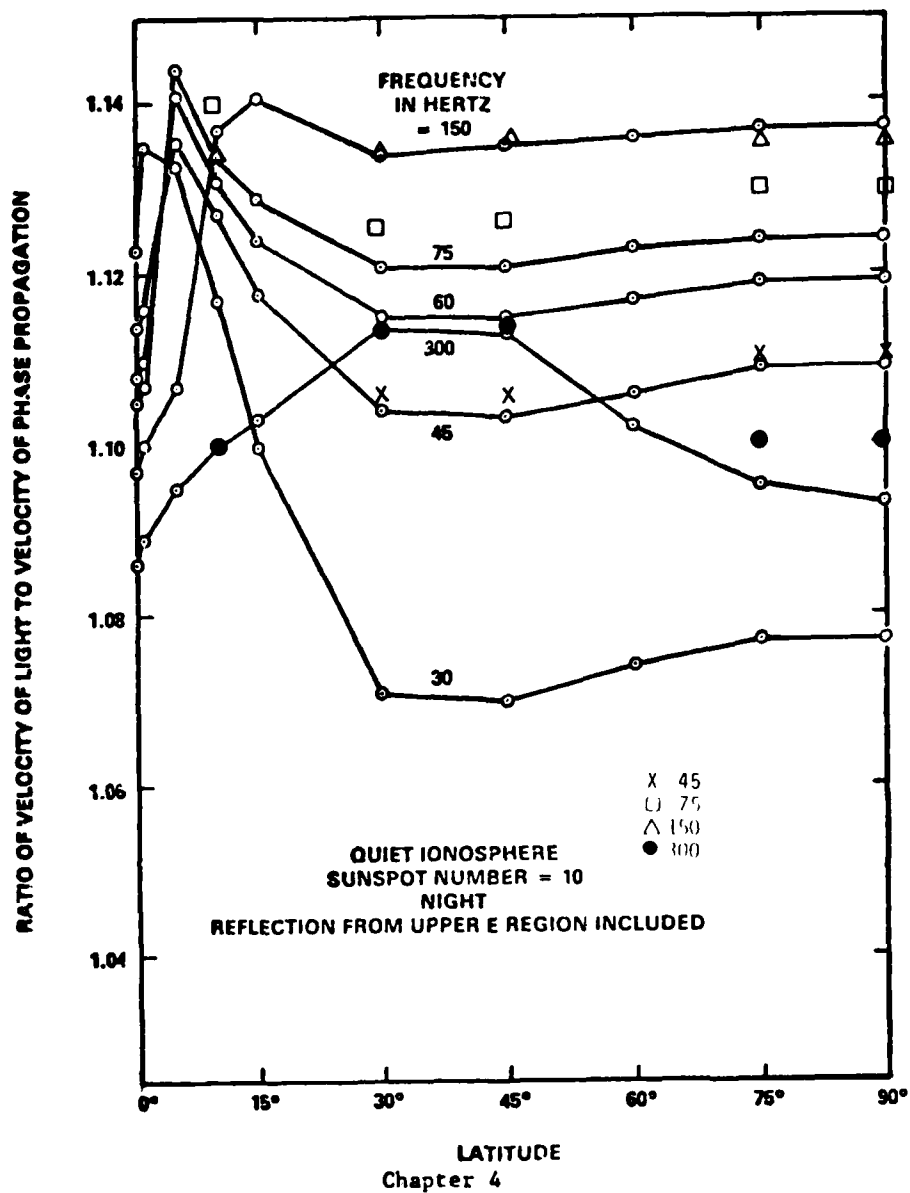


Figure 32. Illustrating the variation of the velocity of phase propagation with latitude and frequency under night-time conditions. Solid curves reproduced from Reference 16. Symbols indicate values obtained with Booker's model at Tempo.

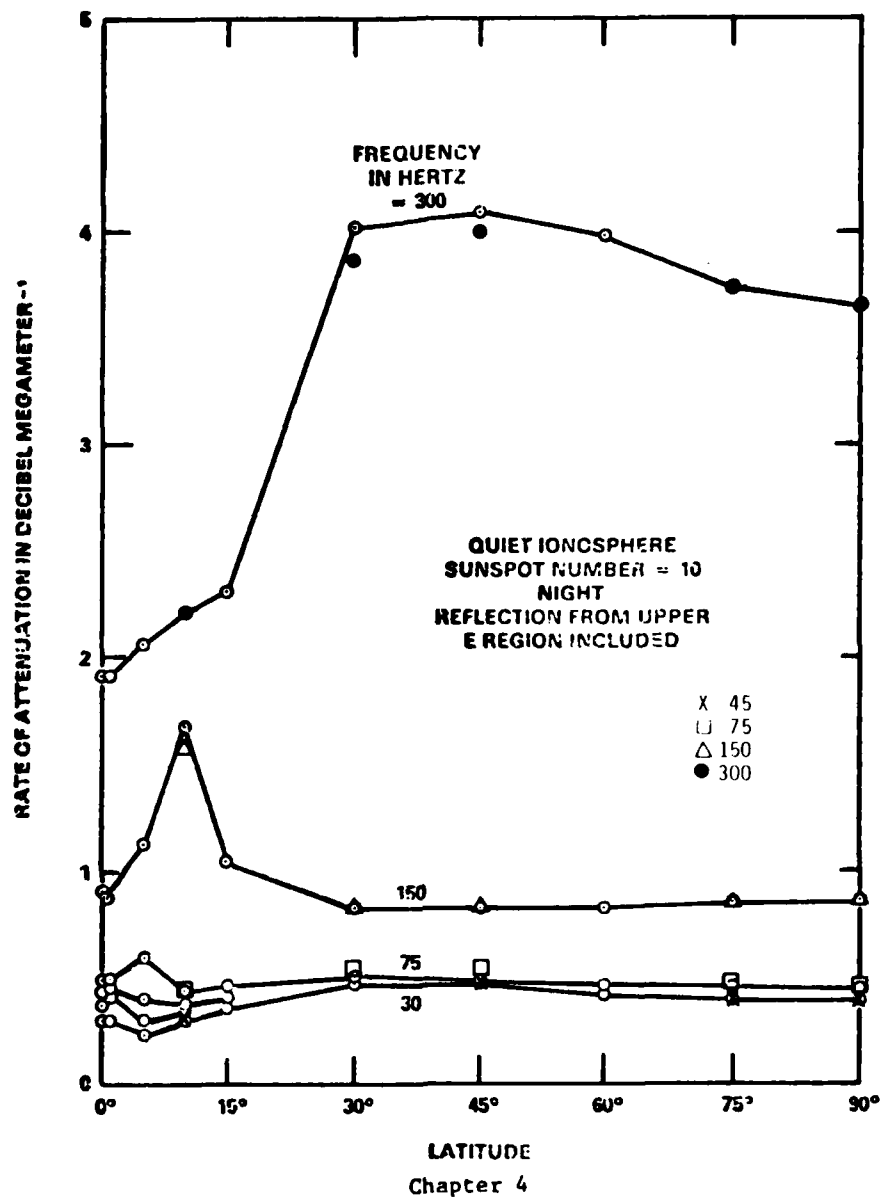


Figure 33. Illustrating the variation of the rate of attenuation with latitude and frequency under nighttime conditions. Solid curves reproduced from Reference 16. Symbols indicate values obtained with Booker's model at Tempo.



Table 4. Ionization and collision frequencies for  
WEDCOM quiet nighttime ionosphere.

z	$N_e$ (cm <sup>-3</sup> )	$N_+$ (cm <sup>-3</sup> )	$\nu_e$ (s <sup>-1</sup> )	$\nu_i$ (s <sup>-1</sup> )
ALT(KM)	ENE(CM-3)	ENP(CM-3)	XNUE(S-1)	XNUI(S-1)
0.00	9.18E-09	5.37E+02	1.53E+11	6.00E+09
5.00	3.89E-07	1.93E+03	8.22E+10	3.39E+09
10.00	4.20E-06	3.73E+03	4.11E+10	1.80E+09
15.00	2.20E-05	5.25E+03	1.91E+10	8.62E+08
20.00	7.12E-05	6.20E+03	8.72E+09	3.93E+08
25.00	1.77E-04	6.33E+03	4.03E+09	1.80E+08
30.00	3.68E-04	5.64E+03	1.90E+09	8.36E+07
35.00	7.80E-04	4.80E+03	9.19E+08	3.95E+07
40.00	1.56E-03	3.75E+03	4.62E+08	1.94E+07
45.00	2.99E-03	2.80E+03	2.41E+08	9.87E+06
50.00	5.58E-03	2.08E+03	1.29E+08	5.23E+06
55.00	1.04E-02	1.56E+03	6.96E+07	3.26E+06
60.00	2.12E-02	1.21E+03	3.65E+07	2.01E+06
65.00	1.62E-01	1.78E+03	1.86E+07	1.21E+06
70.00	2.55E+00	3.59E+03	9.02E+06	7.01E+05
75.00	1.72E+01	2.57E+03	4.12E+06	3.84E+05
80.00	5.36E+01	7.29E+01	1.75E+06	1.96E+05
85.00	6.76E+01	7.50E+01	6.99E+05	9.21E+04
90.00	9.77E+01	1.02E+02	2.73E+05	4.13E+04
95.00	6.05E+02	6.07E+02	1.10E+05	1.87E+04
100.00	1.14E+03	1.14E+03	4.65E+04	8.95E+03
105.00	1.43E+03	1.43E+03	2.14E+04	3.95E+03
110.00	1.81E+03	1.81E+03	1.10E+04	1.92E+03
115.00	2.04E+03	2.04E+03	6.22E+03	1.02E+03
120.00	1.88E+03	1.88E+03	3.87E+03	5.89E+02
130.00	1.32E+03	1.32E+03	1.86E+03	2.48E+02
140.00	1.10E+03	1.10E+03	1.06E+03	1.33E+02
160.00	1.40E+03	1.40E+03	4.32E+02	5.27E+01
180.00	2.18E+03	2.18E+03	2.04E+02	2.57E+01
200.00	3.45E+03	3.45E+03	1.04E+02	1.40E+01

Table 5. Ionization and collision frequencies for NOSC quiet nighttime ionosphere.

z	$N_e$ ( $\text{cm}^{-3}$ )	$N_+$ ( $\text{cm}^{-3}$ )	$\nu_e$ ( $\text{s}^{-1}$ )	$\nu_i$ ( $\text{s}^{-1}$ )
ALT(KM)	ENE(CM-3)	ENP(CM-3)	XNUE(S-1)	XNUI(S-1)
0.00	1.99E-06	5.50E+03	4.30E+11	1.07E+10
5.00	3.35E-06	4.00E+03	1.90E+11	5.30E+09
10.00	6.83E-06	3.50E+03	8.50E+10	2.60E+09
15.00	1.55E-05	3.30E+03	3.77E+10	1.29E+09
20.00	3.54E-05	3.40E+03	1.68E+10	6.37E+08
25.00	8.45E-05	3.70E+03	7.45E+09	3.15E+08
30.00	1.95E-04	3.30E+03	3.30E+09	1.55E+08
35.00	4.00E-04	3.00E+03	1.47E+09	7.70E+07
40.00	7.67E-04	2.50E+03	6.50E+08	3.80E+07
45.00	2.05E-03	2.00E+03	2.70E+08	1.90E+07
50.00	4.98E-03	1.50E+03	1.30E+08	9.30E+06
55.00	1.23E-02	1.00E+03	5.70E+07	4.60E+06
60.00	3.21E-02	8.00E+02	2.60E+07	2.30E+06
65.00	5.57E-02	5.00E+02	1.13E+07	1.10E+06
70.00	8.95E-02	4.00E+02	5.00E+06	5.50E+05
75.00	5.00E+00	4.00E+02	2.20E+06	2.70E+05
80.00	7.50E+01	3.70E+02	9.96E+05	1.34E+05
85.00	1.60E+02	4.00E+02	4.40E+05	6.64E+04
90.00	3.30E+02	4.50E+02	1.97E+05	3.28E+04
95.00	6.00E+02	6.00E+02	8.70E+04	1.60E+04
100.00	2.00E+03	2.00E+03	3.90E+04	8.00E+03
105.00	1.80E+03	1.80E+03	2.60E+04	4.00E+03
110.00	1.40E+03	1.40E+03	1.80E+04	2.00E+03
115.00	8.00E+02	8.00E+02	1.04E+04	1.00E+03
120.00	6.00E+02	6.00E+02	1.00E+04	3.00E+02
130.00	3.70E+02	3.70E+02	4.00E+03	1.50E+02
140.00	2.80E+02	2.80E+02	2.50E+03	8.00E+01
160.00	2.70E+02	2.70E+02	6.00E+02	1.80E+01
180.00	4.50E+02	4.50E+02	1.70E+02	6.00E+00
200.00	1.00E+03	1.00E+03	4.50E+01	2.00E+00

Table 6. Ionization and collision frequencies for WEDCOM  
quiet daytime ionosphere.

z	$N_e$ ( $\text{cm}^{-3}$ )	$N_+$ ( $\text{cm}^{-3}$ )	$\nu_e$ ( $\text{s}^{-1}$ )	$\nu_i$ ( $\text{s}^{-1}$ )
ALT(KM)	ENE(CM-3)	ENP(CM-3)	XNUE(S-1)	XNUI(S-1)
0.00	1.71E-07	3.51E+02	1.53E+11	6.00E+09
5.00	2.00E-06	1.26E+03	8.22E+10	3.39E+09
10.00	1.37E-05	2.44E+03	4.11E+10	1.80E+09
15.00	8.26E-05	3.43E+03	1.91E+10	8.62E+08
20.00	4.56E-04	4.05E+03	8.72E+09	3.93E+08
25.00	2.18E-03	4.13E+03	4.03E+09	1.80E+08
30.00	8.80E-03	3.69E+03	1.90E+09	8.36E+07
35.00	3.12E-03	3.13E+03	9.19E+08	3.95E+07
40.00	8.14E-02	2.45E+03	4.62E+08	1.94E+07
45.00	1.94E-01	1.82E+03	2.41E+08	9.87E+06
50.00	2.53E+00	1.27E+03	1.29E+08	5.23E+06
55.00	1.79E+01	6.11E+02	6.96E+07	3.26E+06
60.00	5.59E+01	2.04E+02	3.65E+07	2.01E+06
65.00	4.49E+02	6.03E+02	1.86E+07	1.21E+06
70.00	1.76E+03	1.85E+03	9.02E+06	7.01E+05
75.00	4.08E+03	4.11E+03	4.12E+06	3.84E+05
80.00	4.86E+03	4.86E+03	1.75E+06	1.96E+05
85.00	5.64E+03	5.64E+03	6.99E+05	9.21E+04
90.00	9.27E+03	9.27E+03	2.73E+05	4.13E+04
95.00	4.55E+04	4.55E+04	1.10E+05	1.87E+04
100.00	8.39E+04	8.39E+04	4.65E+04	8.95E+03
105.00	1.21E+05	1.21E+05	2.14E+04	3.95E+03
110.00	1.54E+05	1.54E+05	1.10E+04	1.92E+03
115.00	1.85E+05	1.85E+05	6.22E+03	1.02E+03
120.00	2.01E+05	2.01E+05	3.87E+03	5.89E+02
130.00	2.10E+05	2.10E+05	1.86E+03	2.48E+02
140.00	2.30E+05	2.30E+05	1.06E+03	1.33E+02
160.00	2.97E+05	2.97E+05	4.32E+02	5.27E+01
180.00	3.39E+05	3.39E+05	2.04E+02	2.57E+01
200.00	3.61E+05	3.61E+05	1.04E+02	1.40E+01

Table 7. Ionization and collision frequencies for NOSC quiet daytime ionosphere.

z	$N_e$ ( $\text{cm}^{-3}$ )	$N_+$ ( $\text{cm}^{-3}$ )	$\nu_e$ ( $\text{s}^{-1}$ )	$\nu_i$ ( $\text{s}^{-1}$ )
ALT(KM)	ENE(CM-3)	ENP(CM-3)	XNUE(S-1)	XNUI(S-1)
0.00	1.99E-06	5.50E+03	4.30E+11	2.14E+10
5.00	3.35E-06	4.00E+03	1.90E+11	1.06E+10
10.00	6.83E-06	3.50E+03	8.50E+10	5.20E+09
15.00	1.55E-05	3.30E+03	3.77E+10	2.58E+09
20.00	3.54E-05	3.40E+03	1.68E+10	1.27E+09
25.00	8.45E-05	3.70E+03	7.45E+09	6.30E+08
30.00	1.95E-04	3.30E+03	3.30E+09	3.10E+08
35.00	4.00E-04	3.00E+03	1.47E+09	1.54E+08
40.00	1.00E-03	2.50E+03	6.50E+08	7.60E+07
45.00	1.00E-02	2.00E+03	2.70E+08	3.80E+07
50.00	1.00E-01	1.50E+03	1.30E+08	1.86E+07
55.00	1.00E+00	1.00E+03	5.70E+07	9.20E+06
60.00	1.00E+01	8.00E+02	2.60E+07	4.60E+06
65.00	2.25E+02	5.00E+02	1.13E+07	2.20E+06
70.00	7.00E+02	9.00E+02	5.00E+06	1.10E+06
75.00	1.50E+03	1.50E+03	2.20E+06	5.40E+05
80.00	3.00E+03	3.00E+03	9.96E+05	2.68E+05
85.00	6.00E+03	6.00E+03	4.40E+05	1.33E+05
90.00	1.20E+04	1.20E+04	1.97E+05	6.56E+04
95.00	3.00E+04	3.00E+04	8.70E+04	3.20E+04
100.00	6.00E+04	6.00E+04	3.90E+04	1.60E+04
105.00	1.00E+05	1.00E+05	2.60E+04	8.00E+03
110.00	1.20E+05	1.20E+05	1.80E+04	4.00E+03
115.00	1.30E+05	1.30E+05	1.04E+04	2.00E+03
120.00	1.40E+05	1.40E+05	1.00E+04	6.00E+02
130.00	1.60E+05	1.60E+05	4.00E+03	3.00E+02
140.00	2.00E+05	2.00E+05	2.50E+03	1.60E+02
160.00	4.00E+05	4.00E+05	6.00E+02	3.60E+01
180.00	6.00E+05	6.00E+05	1.70E+02	1.20E+01
200.00	8.00E+05	8.00E+05	4.50E+01	4.00E+00

Table 8. Ionization and collision frequencies for moderate nuclear ionization.

z	$N_e$ (cm <sup>-3</sup> )	$N_+$ (cm <sup>-3</sup> )	$\nu_e$ (s <sup>-1</sup> )	$\nu_i$ (s <sup>-1</sup> )
ALT(KM)	ENE(CM-3)	ENP(CM-3)	XNUE(S-1)	XNUI(S-1)
0.00	7.55E-06	8.41E+03	1.53E+11	6.00E+09
5.00	1.83E-05	7.66E+03	8.22E+10	3.39E+09
10.00	4.69E-05	7.25E+03	4.11E+10	1.80E+09
15.00	5.62E-04	1.99E+04	1.91E+10	8.62E+08
20.00	1.57E-02	8.24E+04	8.72E+09	3.93E+08
25.00	1.57E-01	1.51E+05	4.03E+09	1.80E+08
30.00	7.21E-01	1.61E+05	1.90E+09	8.36E+07
35.00	3.13E+00	1.33E+05	9.19E+08	3.95E+07
40.00	2.43E+01	1.00E+05	4.62E+08	1.94E+07
45.00	7.77E+01	7.39E+04	2.41E+08	9.87E+06
50.00	1.60E+02	5.00E+04	1.29E+08	5.23E+06
55.00	8.00E+02	2.23E+04	6.96E+07	3.26E+06
60.00	1.69E+03	7.93E+03	3.65E+07	2.01E+06
65.00	2.48E+03	3.46E+03	1.86E+07	1.21E+06
70.00	2.51E+03	2.62E+03	9.02E+06	7.01E+05
75.00	2.49E+03	2.49E+03	4.12E+06	3.84E+05
80.00	3.07E+03	3.07E+03	1.75E+06	1.96E+05
85.00	8.07E+03	8.07E+03	6.99E+05	9.21E+04
90.00	1.36E+04	1.36E+04	2.73E+05	4.13E+04
95.00	3.77E+04	3.77E+04	1.10E+05	1.87E+04
100.00	1.00E+05	1.00E+05	4.65E+04	8.95E+03
105.00	1.95E+05	1.95E+05	2.14E+04	3.95E+03
110.00	2.40E+05	2.40E+05	1.10E+04	1.92E+03
115.00	2.20E+05	2.20E+05	6.22E+03	1.02E+03
120.00	2.40E+05	2.40E+05	3.87E+03	5.89E+02
130.00	3.06E+05	3.06E+05	1.86E+03	2.48E+02
140.00	2.48E+05	2.48E+05	1.06E+03	1.33E+02
160.00	2.98E+05	2.98E+05	4.32E+02	5.27E+01
180.00	4.80E+05	4.80E+05	2.04E+02	2.57E+01
200.00	1.09E+07	1.09E+07	1.04E+02	1.40E+01

Table 9. Comparison of attenuation rate and phase velocity from NOSC and Booker models, 75 Hz.

Profile	Booker Model		NOSC Model	
	$\alpha$	c/v	$\alpha$	c/v
WEDCOM Night	2.1	1.28	1.5	1.26
NOSC Night	1.8	1.21	0.9	1.17
WEDCOM Day	1.6	1.24	1.7	1.19
NOSC Day	1.3	1.22	1.3	1.20
Nuclear	4.3	1.46	3.8	1.39

Table 10. Comparison of attenuation rate and phase velocity from NOSC and Booker models, 150 Hz.

Profile	Booker Model		NOSC Model	
	$\alpha$	c/v	$\alpha$	c/v
WEDCOM Night	3.1	1.24	2.5	1.24
NOSC Night	2.9	1.21	1.3	1.18
WEDCOM Day	2.7	1.20	2.2	1.16
NOSC Day	2.5	1.19	2.2	1.16
Nuclear	6.7	1.34	6.0	1.29

where

$$N_g^2 = \frac{\epsilon}{\epsilon_0} - j \frac{\sigma}{\omega \epsilon_0}$$

C = cosine of eigenangle

$\sigma$  = ground conductivity

$\epsilon$  = ground dielectric constant (farad m<sup>-1</sup>)

$\epsilon_0$  = free space dielectric constant (8.854 m<sup>-12</sup> farad m<sup>-1</sup>)

$\sigma$  = ground conductivity (mho m<sup>-1</sup>).

The excitation factors can be approximated from relations given in References 14 and 11:

$$\lambda_V \approx \frac{j^{1/2} s^{3/2}}{4(\omega/c)H_R} \quad (55)$$

$$\lambda_B \approx 0 \quad (56)$$

$$\lambda_E \approx \frac{-j}{s} \lambda_V = \frac{-j^{3/2} s}{4(\omega/c)H_R} \quad (57)$$

where  $H_R$  is an effective reflection height. Use of the real part of  $\tilde{Z}_B$  gives good results and is consistent with approximations used in Reference 22.

Tables 11 and 12 show comparisons of height gain and excitation factor calculations obtained from the above equations (approximate model) and the full wave model described in Reference 14.

Table 11. Comparison of excitation and height gain factors from full wave (first entry) and approximate (second entry) models, 150 Hz.

Profile	$ \lambda_V $	$ \lambda_E $	$ \lambda_B $	$ e_V $	$ e_E $	$ e_B $
WEDCOM Night	1.3	1.6	0.1	2	8.2(-5)	6.2(-5)
	1.3	1.7	0	2	8.2(-5)	6.3(-5)
NOSC Night	1.2	1.4	0.1	2	8.2(-5)	5.3(-5)
	1.3	1.6	0	2	8.2(-5)	5.8(-5)
WEDCOM Day	1.6	1.8	0.2	2	8.2(-5)	5.2(-5)
	1.6	1.9	0	2	8.2(-5)	5.7(-5)
NOSC Day	1.5	1.7	0.2	2	8.2(-5)	5.1(-5)
	1.5	1.8	0	2	8.2(-5)	5.5(-5)
Nuclear	2.2	2.9	0.1	2	8.2(-5)	7.5(-5)
	2.3	3.2	0	2	8.2(-5)	8.2(-5)

Table 12. Comparison of excitation and height-gain factors from full wave model (first entry) and approximate (second entry) models, 75 Hz.

Profile	$ \lambda_V $	$ \lambda_E $	$ \lambda_B $	$ e_V $	$ e_E $	$ e_B $
WEDCOM Night	2.7	3.4	0.3	2	5.8(-5)	4.7(-5)
	2.6	3.4	0	2	5.8(-5)	4.9(-5)
NOSC Nigh <sup>+</sup>	2.4	2.8	0.6	2	5.8(-5)	3.6(-5)
	2.5	3.1	0	2	5.8(-5)	4.2(-5)
WEDCOM Day	3.7	3.9	0.4	2	5.8(-5)	4.1(-5)
	3.4	4.2	0	2	5.8(-5)	4.5(-5)
NOSC Day	3.3	3.9	0.5	2	5.8(-5)	4.1(-5)
	3.1	3.8	0	2	5.8(-5)	4.2(-5)
Nuclear	5.1	7.2	0.4	2	5.8(-5)	6.2(-5)
	5.5	8.1	0	2	5.8(-5)	6.8(-5)



## SECTION 6

### CODE STRUCTURE

Major computational elements used in link vulnerability and simulation codes include:

- Environment
- Propagation
- Signal processing
- Network status.

The network status calculation can be included in simulation codes where circuit performance for many circuits is evaluated or performed separately using results from simulation codes.

A desirable goal is to have common environment calculations for communication codes. Environment includes descriptions of the natural and disturbed atmospheres. This includes electron and ion densities and collision frequencies and can include dust, water vapor, other molecular species, and possibly terrain modifications (cratering). Link vulnerability codes generally use engineering models for environment calculations. These models describe specific physical processes but use engineering approximations for part or all of the phenomena. The models require much less computational time than first principle models (eg, detailed MHD calculations) but still provide sufficient detail and accuracy for systems applications. Multiburst, multilink simulation codes require even faster running models in order to handle the large spatial and temporal regions required. This is accomplished through the use of simplified algorithms or a precomputed data base that can be interpolated. By developing the simulation environment models from those developed for link vulnerability codes the desired consistency between the communication code environment models can be maintained.

The engineering ionization calculations for link vulnerability codes can be conveniently divided into the following models:

- Natural (undisturbed) atmosphere
- Natural ionosphere
- Fireball/debris geometry
- D-region ionization

- E- and F-region ionization
- Fireball ionization.

In performing these calculations the spatial region requirements and the ionization modeling are significantly different for ionospheric dependent propagation (ELF through HF) and line-of-sight (LOS) propagation in and above the VHF band. In the latter case ionization calculations are needed along LOS paths. In general the LOS paths can move with time and calculations must either be made along each path of interest or a three-dimensional grid and interpolation procedure must be used. If D-region ionization is to be included, the grid size must be relatively small or calculations are required along the LOS path in the D region and the grid only used in the E and F regions (method used in ROSCOE). Generally, equilibrium ionization calculations can be used for ionization levels affecting propagation in and above the VHF band. Finally, it is generally efficient to combine ionization and propagation calculations for LOS paths.

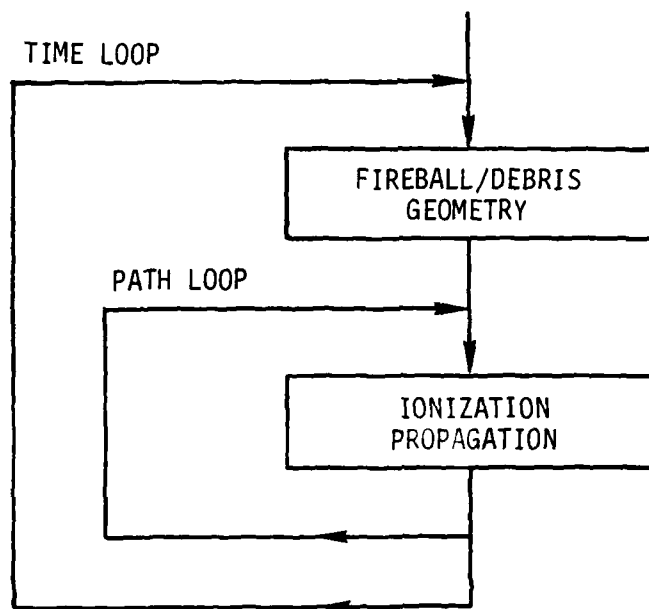
For ionospheric dependent propagation, calculations are required in a vertical plane defined by the great circle path between transmitter and receiver (this neglects off-great circle paths). For ELF and VLF propagation, ionization along vertical profiles is required for mode solutions. For LF and HF propagation ionization calculations are required along skywave paths. Since a relatively large number of skywaves can propagate, it is generally efficient to determine the ionization along vertical profiles and then use these to determine ionization along the skywaves. The ionization levels that can affect ionospheric dependent propagation are small enough that nonequilibrium conditions can be important. These include the buildup of ionization after a debris region has moved into an area and the decay of ionization after a debris region has moved away. For ionospheric dependent propagation it is generally not efficient to combine ionization and propagation calculations.

For both LOS propagation and ionospheric dependent propagation the fireball and debris geometry can be calculated from the same model. For LOS propagation fireball ionization along those paths that intersect the fireball can be computed from fireball geometry and ionization models. For ionospheric dependent propagation fireball ionization along the vertical paths used to define the plane between terminals can be determined but ionization affecting off-great circle paths is difficult to determine in an efficient manner. Use of simplified spatial distributions may be adequate for estimates or propagation flags.

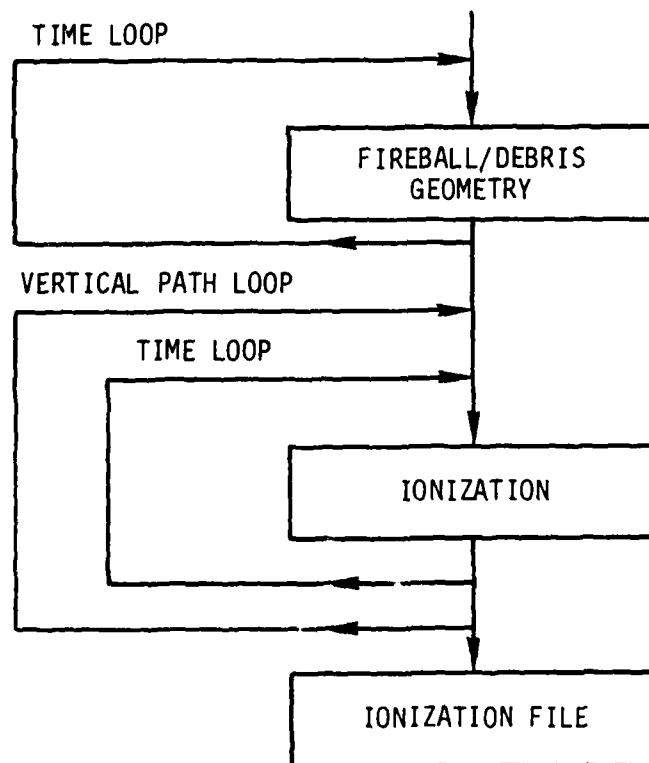
Figure 34 shows simplified flow diagrams for the ionization models required for LOS and ionospheric dependent propagation calculations. The time loop could be placed outside the path loop for ionospheric dependent propagation but this requires considerable storage in order to perform nonequilibrium ionization calculations.

The selection of the vertical path locations for ionospheric dependent ionization calculations will affect both accuracy and computation time. For most natural ionospheric conditions vertical path spacings of several thousands of kilometers are adequate. Smaller spacings are generally required for disturbed conditions. A reasonably efficient method for determining the vertical path locations appears to be to first select locations based on the natural ionosphere. Then for each interval between vertical paths tests could be made to see if nuclear ionization is important. If it is, the interval could be divided into smaller intervals. In order to determine whether nuclear ionization is important the great circle distance from each terminal and from the center of the interval between terminals to the burst point (prompt ionization) or to the debris center (delayed ionization) would be determined and compared to an effects radius. The effects radius would be a function of burst altitude (prompt ionization) or debris altitude (delayed ionization) and frequency. Since the nuclear ionization can move with time, the tests would be made at all calculation times and an interval spacing between vertical paths would only remain at the value chosen for the natural ionosphere if nuclear ionization was not important at any of the calculation times. An interval spacing of 2000 km for natural conditions and 500 km for disturbed conditions appears consistent with accuracy and computational time requirements. A smaller spacing for regions affected by surface or near-surface bursts may be required for some systems applications but generally ionospheric dependent propagation is not significantly affected by small ionization regions.

The altitude interval used to compute ionization for the vertical paths depends on propagation frequency. For ELF propagation, ionization calculations are required below about 200 km. For VLF and LF propagation ionization calculations are required below about 100 km. For HF propagation the altitude interval required depends on whether skywave geometries are determined from precomputed results for natural conditions or are found by ray tracing. If precomputed results are used, ionization calculations are only needed below about 120 km. Ray tracing would require ionization calculations below about 400 km.



34a. LOS propagation



34b. Ionospheric dependent propagation

Figure 34. Simplified ionospheric dependent propagation flow diagrams for LOS and ionospheric dependent propagation ionization models.

Several methods are used to select calculation times in communication codes. In the current WESCOM and WEDCOM codes the calculation times are selected from user input data. In HFNET calculations are made at update times determined by the code and then calculations at event times (user requested times or times when the codes determines that calculations are required) are found by interpolation. The use of user selected calculation times is the simplest method of time selection since it does not require update times or interpolation procedures. However, it requires that the user have some knowledge of significant times and reasonable time intervals between calculations. The use of code selected times allows determining times based on environment calculations. If an ionization file is prepared for code selected update times, it can be subsequently used to determine ionization at user selected calculation times. By saving the ionization file the user selected times could be changed in subsequent calculations.

A three-level option for selection of calculation times appears useful. The first option would be the use of user selected times as in the current WEDCOM code. The second option would be the use of code determined times between input start and stop times. The third option would be the use of the ionization file prepared for option 2 to determine ionization at user selected times.

## REFERENCES

1. Rutherford, R.R., *WEDCOM IV: A Fortran Code for the Calculation of ELF, VLF, and LF Propagation in a Nuclear Environment, Volume III*, DNA 4422T-3, General Electric-TEMPO, Santa Barbara, CA, November 1978.
2. Rutherford, R.R., and B. Gambill, *Balloon Gateway Communication Trade-Off Studies, VLF/LF/MF Computer Code Modifications*, GE80TMP-32, General Electric-TEMPO, Santa Barbara, CA, June 1980.
3. Feniger, E.J., and B. Gambill, private communications, SIMBAL: A Fortran Code for Evaluation of the Effects of Multiple Nuclear Weapons, Kaman Tempo, March 1980.
4. Barghausen, A.F., et al, *Predicting Long-Term Operational Parameters of High Frequency Sky-Wave Telecommunication Systems*, ERL 110-ITS-78, U.S. Department of Commerce (ESSA), Boulder, CO, May 1968.
5. Millington, G., "Ground-Wave Propagation Over an Inhomogeneous Smooth Earth," Institution of Electrical Engineers, London. *Proceedings Part 3*, 96, January 1949.
6. Johler, J.R., et al, "Phase of the Low Radiofrequency Ground Wave," *National Bureau of Standards Circular 573*, June 1956.
7. Gambill, B., and K. Schwartz, *Loran-C Signal Analysis-Propagation Model Evaluation*, General Electric-TEMPO, GE78TMP-51, July 1979.
8. Eckersley, P.R., *Proceedings of the Institute of Radio Engineers*, 18, 1930.
9. Rutherford, R.R., and B. Gambill, *Balloon Gateway Communication Studies, Analysis of LF Propagation with Parametric Ionospheric Profiles*, GE80TMP-38, General Electric-TEMPO, Santa Barbara, CA, August 1980.
10. Wait, J.R., "Diffractive Corrections to the Geometrical Optics of Low Frequency Propagation," *Electromagnetic Wave Propagation*, Edited by M. Deserant and J.M. Michiels, Academic Press, London and New York, 1960.
11. Wait, J.R., *Electromagnetic Waves in Stratified Media*, Pergamon Press, The MacMillan Company, New York, 1962.
12. Wait, J.R., and L.C. Walters, "Reflection of VLF Radio Waves from an Inhomogeneous Ionosphere: Part 1, Exponentially Varying Isotropic Model," *Journal of Research*, 67D, No 3, pp 361-367, National Bureau of Standards, January 1963.
13. Morfitt, D.G., and C.H. Shellman, *MODESRCH, An Improved Computer Program for Obtaining ELF/VLF/LF Mode Constants in an Earth-Ionosphere Waveguide*, Interim Report No. 77T, Naval Electronics Laboratory Center, San Diego, CA, October 1976.

14. Pappert, R.A., and W.F. Moler, "Propagation Theory and Calculations at Lower Extremely Low Frequencies (ELF)," *Trans IEEE, CCM-22*, pp 438-451.
15. Budden, J.C., "The Numerical Solution of Differential Equations Governing Reflection of Long Radio Waves from the Ionosphere," *Royal Society of London Proceeding Series A*, 227, pp 516-537.
16. Booker, H.G., *A Simplified Theory of ELF Propagation in the Earth-Ionosphere Transmission Line and its Worldwide Application*, University of California, San Diego, 31 March 1980.
17. Booker, H.G., and F. Lefeuvre, "The Relation Between Ionospheric Profiles and ELF Propagation in the Earth-Ionosphere Transmission Line," *J. Atmos. Terr. Phys.*, 39, pp 1277-1292.
18. Greifinger, C., and P. Greifinger, "Approximate Method for Determining ELF Eigenvalues in the Earth-Ionosphere Waveguide," *Radio Science* 13, pp 831-837.
19. Greifinger, C., and P. Greifinger, "On the Ionospheric Parameters which Govern High Latitude ELF Propagation in the Earth-Ionosphere Waveguide," *Radio Science* 14, pp 889-895.
20. Booker, H.G., private communication, University of California, San Diego, 22 July 1981.
21. Booker, H.G., "Fitting of Multi-Region Ionospheric Profiles of Electron Density by a Single Analytic Function of Height," *J. Atmos. Terr. Phys.*, 39, pp 619-623.
22. Greifinger, C., and P. Greifinger, *Extended Theory for Approximate ELF Propagation Constants in the Earth-Ionosphere Waveguide*, DNA 5561T, RDA-TR-110005-001, R&D Associates, Marina del Ray, CA, 1 September 1979.

## DISTRIBUTION LIST

### DEPARTMENT OF DEFENSE

Assistant to the Secretary of Defense  
Atomic Energy  
ATTN: Executive Assistant

Command & Control Tech Ctr  
ATTN: C-650  
ATTN: C-312, R. Mason  
ATTN: C-650, G. Jones  
3 cy ATTN: C-650, W. Heidig

Defense Communications Agency  
ATTN: J300 for Yen-Sun Fu  
ATTN: Code 230  
ATTN: Code 205

Defense Communications Engr Ctr  
ATTN: Code R410  
ATTN: Code R410, N. Jones  
ATTN: Code R123  
ATTN: CODE R410, R. Craighill

Defense Intelligence Agency  
ATTN: DT-1B  
ATTN: DB-4C, E. O'Farrell  
ATTN: DB, A. Wise  
ATTN: Dir  
ATTN: DC-7B

Defense Nuclear Agency  
ATTN: RAAE, P. Lunn  
ATTN: NATD  
ATTN: STNA  
ATTN: RAEE  
ATTN: NAFD  
3 cy ATTN: RAAE  
4 cy ATTN: TITL

Defense Tech Info Ctr  
12 cy ATTN: DD

Deputy Under Secretary of Defense  
Comm, Cmd, Cont & Intell  
ATTN: Dir of Intell Systems

Field Command  
Defense Nuclear Agency  
Lawrence Livermore Lab  
ATTN: FC-1

Field Command  
Defense Nuclear Agency  
ATTN: FCTT, G. Ganong  
ATTN: FCTT, W. Summa  
ATTN: FCPR

Interservice Nuclear Weapons School  
ATTN: TTV

Joint Strat Tgt Planning Staff  
ATTN: JLTW-2  
ATTN: JLA, Threat Applications Div

Joint Chiefs of Staff  
ATTN: C3S, Evaluation Ofc, HDOO  
ATTN: C3S

### DEPARTMENT OF DEFENSE (Continued)

National Security Agency  
ATTN: W-32, O. Bartlett  
ATTN: R-52, J. Skillman  
ATTN: B-3, F. Leonard

Under Secretary of Defense for Rsch & Engrg  
ATTN: Strategic & Space Sys (OS)  
ATTN: Strat & Theater Nuc Forces, B. Stephan

WWMCCS System Engrg Org  
ATTN: J. Hoff

### DEPARTMENT OF THE ARMY

Assistant Chief of Staff for Automation & Comm  
ATTN: DAMO-C4, P. Kenny

Atmospheric Sciences Lab  
ATTN: DELAS-EQ, F. Niles

BMD Advanced Technology Ctr  
ATTN: ATC-T, M. Capps  
ATTN: ATC-O, W. Davies  
ATTN: ATC-R, W. Dickinson  
ATTN: ATC-R, D. Russ

BMD Systems Command  
ATTN: BMDSC-HLE, R. Webb  
2 cy ATTN: BMDSC-HW

Deputy Chief of Staff for Ops & Plans  
ATTN: DAMO-RQC, C2 Div

Harry Diamond Labs  
ATTN: DELHD-NW-R, R. Williams  
2 cy ATTN: DELHD-NW-P

US Army Chemical School  
ATTN: ATZN-CM-CS

US Army Comm-Elec Engrg Instal Agency  
ATTN: CCC-CED-CCO, W. Neuendorf  
ATTN: CCC-EMEO-PED, G. Lane

US Army Communications Cmd  
ATTN: CC-OPS-WR, H. Wilson  
ATTN: CC-OPS-W

US Army Communications R&D Cmd  
ATTN: DRDCO-COM-RY, W. Kesselman

US Army Foreign Science & Tech Ctr  
ATTN: DRXST-SD

US Army Nuclear & Chemical Agency  
ATTN: Library

US Army Satellite Comm Agency  
ATTN: Document Control

US Army RADOC Sys Analysis Actvty  
ATTN: ATAA-TDC  
ATTN: ATAA-PL  
ATTN: ATAA-TCC, F. Payan, Jr



DEPARTMENT OF THE ARMY (Continued)

USA Missile Command  
ATTN: DRSMI-YSO, J. Gamble

US Army Materiel Dev & Readiness Cmd  
ATTN: DRCLDC, J. Bender

DEPARTMENT OF THE NAVY

Joint Cruise Missiles Project Ofc  
ATTN: JCMG-707

Naval Air Systems Command  
ATTN: PMA 271

Naval Electronic Systems Command  
ATTN: PME 106-13, T. Griffin  
ATTN: PME 117-2013, G. Burnhart  
ATTN: PME 117-211, B. Kruger  
ATTN: Code 501A  
ATTN: Code 3101, T. Hughes  
ATTN: PME 106-4, S. Kearney  
ATTN: PME 117-20

Naval Intelligence Support Ctr  
ATTN: NISC-50

Naval Ocean Systems Ctr  
ATTN: Code 5322, M. Paulson  
ATTN: Code 5323, J. Ferguson  
ATTN: Code 532

Naval Rsch Lab  
ATTN: Code 7500, B. Wald  
ATTN: Code 4780, S. Ossakow  
ATTN: Code 4720, J. Davis  
ATTN: Code 4780  
ATTN: Code 4700  
ATTN: Code 6700  
ATTN: Code 4187  
ATTN: Code 7950, J. Goodman

Naval Space Surveillance System  
ATTN: J. Burton

Naval Surface Weapons Ctr  
ATTN: Code F31

Naval Telecommunications Command  
ATTN: Code 341

Office of the Deputy Chief of Naval Ops  
ATTN: OP 981N  
ATTN: OP 941D  
ATTN: NOP 65, Strat Theater Nuc Warf Div

Office of Naval Rsch  
ATTN: Code 412, W. Condell  
ATTN: Code 414, G. Joiner

Strategic Systems Project Office  
ATTN: NSP-2722, F. Wimberly  
ATTN: NSP-2141  
ATTN: NSP-43

DEPARTMENT OF THE AIR FORCE

Aerospace Defense Command  
ATTN: DC, T. Long

DEPARTMENT OF THE AIR FORCE (Continued)

Air Force Geophysics Lab  
ATTN: ORP, R. Gardiner  
ATTN: ORP-1  
ATTN: L+B, J. Champion  
ATTN: CA, A. Stain  
ATTN: R. O'Neill  
ATTN: PHP  
ATTN: PHI, J. Buchan  
ATTN: R. Babcock

Air Force Tech Applications Ctr  
ATTN: TN

Air Force Weapons Lab  
ATTN: NYC  
ATTN: SUL  
ATTN: NTN

Air Force Wright Aeronautical Lab  
ATTN: W. Hunt  
ATTN: A. Johnson

Air University Library  
ATTN: AUL-158

Headquarters  
Air Weather Service, MAC  
ATTN: OWSR, R. Prohaska

Assistant Chief of Staff  
Studies & Analyses  
ATTN: AF/ASO, W. Fraus  
ATTN: AF/ASO, C. Rightmeyer

Ballistic Missile Office  
ATTN: ENSN, W. Wilson  
ATTN: SYC, Col Ewan

Air Logistics Command  
ATTN: OP-ALC/MM

Deputy Chief of Staff  
Rsch, Dev, & Acq  
ATTN: AFRDSS  
ATTN: AFRDSP  
ATTN: AFRDS, Space Sys & CD Dir

Deputy Chief of Staff  
Operations and Plans  
ATTN: AFXOXT  
ATTN: AFXOPS  
ATTN: AFXOXCD  
ATTN: AFXOXFD

Headquarters  
Electronic Systems Div/SCT-2  
ATTN: SCT-2, J. Clark

Headquarters  
Electronic Systems Div  
ATTN: OCT-4, J. Deas  
ATTN: YSM, J. Kobelski  
ATTN: YSEA

DEPARTMENT OF THE AIR FORCE (Continued)

Foreign Technology Div  
ATTN: TQTD, B. Ballard  
ATTN: NIIS, Library

Rome Air Dev Ctr  
ATTN: OCS, V. Coyne  
ATTN: TSLD

Rome Air Dev Ctr  
ATTN: EEP

Space Div  
ATTN: YGJB, W. Mercer  
ATTN: YKM, Maj Alexander  
ATTN: YKM, Capt Norton

Strategic Air Command  
ATTN: XPFS  
ATTN: DCX  
ATTN: ADWATE, B. BAUER  
ATTN: NRT  
ATTN: DCXT, T. Jorgensen

OTHER GOVERNMENT AGENCIES

Central Intelligence Agency  
ATTN: OSWR/NED  
ATTN: OSWR/SSD for, K. Feuerpfel

Department of Commerce  
National Bureau of Standards  
ATTN: Sec Ofc for R. Moore

Department of Commerce  
National Oceanic & Atmospheric Admin  
ATTN: R. Grubb

Institute for Telecommunications Sciences  
ATTN: A. Jean  
ATTN: W. Utlaut  
ATTN: L. Berry

DEPARTMENT OF ENERGY CONTRACTORS

EG&G, Inc  
ATTN: J. Colvin  
ATTN: D. Wright

University of California  
Lawrence Livermore National Lab  
ATTN: L-31, R. Hager  
ATTN: L-389, R. Ott  
ATTN: Tech Info Dept Library

Los Alamos National Lab  
ATTN: P. Keaton  
ATTN: C. Westervelt  
ATTN: R. Jeffries  
ATTN: T. Kunkle, ESS-5  
ATTN: D. Simons  
ATTN: MS 664, J. Zinn  
ATTN: MS 670, J. Hopkins  
ATTN: J. Wolcott

DEPARTMENT OF ENERGY CONTRACTORS (Continued)

Sandia National Lab  
ATTN: D. Dahlgren  
ATTN: D. Thornbrough  
ATTN: 3141  
ATTN: Org 4231, T. Wright  
ATTN: Space Project Div  
ATTN: Org 1250, W. Brown

Sandia National Labs, Livermore  
ATTN: T. Cook  
ATTN: B. Murphey

DEPARTMENT OF DEFENSE CONTRACTORS

Aerospace Corp  
ATTN: I. Garfunkel  
ATTN: D. Olsen  
ATTN: J. Straus  
ATTN: V. Josephson  
ATTN: T. Salmi  
ATTN: R. Slaughter

Analytical Systems Engrg Corp  
ATTN: Radio Sciences

Analytical Systems Engrg Corp  
ATTN: Security

GDM Corp  
ATTN: L. Jacobs  
ATTN: T. Neighbors

Berkley Rsch Associates, Inc  
ATTN: J. Workman  
ATTN: S. Brecht  
ATTN: C. Prettie

Boeing Aerospace Co, a Div of Boeing Co  
ATTN: MS/87-63, D. Clauson

Boeing Co  
ATTN: S. Tashird  
ATTN: G. Hall

Booz-Allen & Hamilton, Inc  
ATTN: B. Wilkinson

BR Communications  
ATTN: J. McLaughlin

University of California at San Diego  
ATTN: H. Looker

Charles Stark Draper Lab, Inc  
ATTN: D. Cox  
ATTN: J. Gilmore  
ATTN: A. Tetlow

Computer Sciences Corp  
ATTN: T. E. Roberts

Comat Lab  
ATTN: J. J. J. J.  
ATTN: J. J. J. J.

AD-A127 455

STATUS REPORT ON PREPARATION OF A REVISED LONGWAVE  
COMMUNICATION LINK VUL. (U) KAMAN TEMPO SANTA BARBARA  
CA R R RUTHERFORD ET AL. 01 OCT 81 KT-81-022(R)

2/2

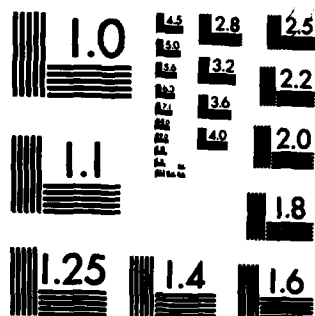
UNCLASSIFIED

DNA-5879T DNA001-80-C-0098

F/G 20/14

NL





DEPARTMENT OF DEFENSE CONTRACTORS (Continued)

Cornell University  
ATTN: M. Kelly  
ATTN: D. Farley, Jr

E-Systems, Inc  
ATTN: R. Berezdivin

Electrospace Systems, Inc  
ATTN: H. Logston  
ATTN: P. Phillips

ESL, Inc  
ATTN: E. Tsui  
ATTN: R. Ibaraki  
ATTN: R. Heckman  
ATTN: J. Marshall  
ATTN: J. Lehman

General Electric Co  
ATTN: C. Zierdt  
ATTN: A. Steinmayer

General Electric  
ATTN: F. Reibert

General Electric Co  
ATTN: G. Millman

General Rsch Corp  
ATTN: B. Bennett

Geocenters, Inc  
ATTN: E. Marram

Harris Corp  
ATTN: E. Knick

Horizons Technology, Inc  
ATTN: R. Kruger

HSS, Inc  
ATTN: D. Hansen

IBM Corp  
ATTN: H. Ulander

Institute for Defense Analyses  
ATTN: H. Gates  
ATTN: E. Bauer  
ATTN: H. Wolfhard  
ATTN: J. Aein

International Tel & Telegraph Corp  
ATTN: Technical Library

International Tel & Telegraph Corp  
ATTN: G. Wetmore

JAYCOR  
ATTN: J. Sperling

JAYCOR  
ATTN: J. Doncarlos

Kaman Sciences Corp  
ATTN: T. Stephens

DEPARTMENT OF DEFENSE CONTRACTORS (Continued)

Johns Hopkins University  
ATTN: J. Phillips  
ATTN: T. Evans  
ATTN: J. Newland  
ATTN: P. Komiske

Kaman Tempo  
ATTN: DASIAC  
ATTN: W. McNamara  
ATTN: K. Schwartz  
ATTN: J. Devore  
4 cy ATTN: W. Knapp  
4 cy ATTN: R. Rutherford

Litton Systems, Inc  
ATTN: B. Zimmer

Lockheed Missiles & Space Co, Inc  
ATTN: C. Old, Dept 68-21  
ATTN: D. Churchill, Dept 81-11  
ATTN: Dept 60-12

M.I.T. Lincoln Lab  
ATTN: D. Towle

Lockheed Missiles & Space Co., Inc  
ATTN: R. Sears  
ATTN: J. Kumer

MA/COM Linkabit Inc  
ATTN: A. Viterbi  
ATTN: I. Jacobs  
ATTN: H. Van Trees

Magnavox Govt & Indus Electronics Co  
ATTN: G. White

Martin Marietta Corp  
ATTN: R. Hefner

McDonnell Douglas Corp  
ATTN: Tech Library Svcs  
ATTN: R. Halprin  
ATTN: H. Spitzer  
ATTN: W. Olson

Meteor Communications Corp  
ATTN: R. Leader

Mission Research Corp  
ATTN: R. Bogusch  
ATTN: R. Bigoni  
ATTN: C. Lauer  
ATTN: F. Fajen  
ATTN: R. Kilb  
ATTN: S. Gutsche  
ATTN: R. Hendrick  
ATTN: G. McCartor  
ATTN: Tech Library  
ATTN: F. Guigliano

Mitre Corp  
ATTN: A. Kymmel  
ATTN: C. Callahan  
ATTN: MS J104, M. Dresp  
ATTN: G. Harding  
ATTN: B. Adams

DEPARTMENT OF DEFENSE CONTRACTORS (Continued)

Mitre Corp

ATTN: M. Horrocks  
ATTN: W. Hall  
ATTN: J. Wheeler  
ATTN: W. Foster

Pacific-Sierra Research Corp

ATTN: F. Thomas  
ATTN: E. Field, Jr  
ATTN: H. Brode, Chairman SAGE

Pennsylvania State University

ATTN: Ionospheric Rsch Lab

Photometrics, Inc

ATTN: I. Kofsky

Physical Dynamics, Inc

ATTN: E. Fremouw

Physical Rsch, Inc

ATTN: R. Deliberis

R & D Associates

ATTN: W. Karzas  
ATTN: W. Wright  
ATTN: C. Greifinger  
ATTN: R. Lelevier  
ATTN: F. Gilmore  
ATTN: B. Gabbard  
ATTN: H. Ory  
ATTN: R. Turco  
ATTN: M. Gantsweg

R & D Associates

ATTN: B. Yoon

Rand Corp

ATTN: E. Bedrozian  
ATTN: C. Crain

Riverside Rsch Institute

ATTN: V. Trapani

Rockwell International Corp

ATTN: S. Quilici

Santa Fe Corp

ATTN: D. Paolucci

Science Applications, Inc

ATTN: L. Linson  
ATTN: E. Straker  
ATTN: D. Hamlin  
ATTN: C. Smith

Rockwell International Corp

ATTN: R. Buckner

DEPARTMENT OF DEFENSE CONTRACTORS (Continued)

Science Applications, Inc

ATTN: SZ

Science Applications, Inc

ATTN: J. Cockayne

SRI International

ATTN: G. Price  
ATTN: R. Tsunoda  
ATTN: J. Vickrey  
ATTN: W. Chesnut  
ATTN: D. Neilson  
ATTN: J. Petrickes  
ATTN: R. Leadabrand  
ATTN: R. Livingston  
ATTN: M. Baron  
ATTN: A. Burns  
ATTN: C. Rino  
ATTN: W. Jaye  
ATTN: G. Smith  
ATTN: V. Gonzales  
ATTN: D. McDaniels

Stewart Radiance Lab

ATTN: J. Ulwich

Sylvania Systems Group

ATTN: R. Steinhoff

Strategic Systems Div

ATTN: J. Concordia  
ATTN: I. Kohlberg

Technology International Corp

ATTN: W. Boquist

Tri-Com, Inc

ATTN: D. Murray

TRW Electronics & Defense Sector

ATTN: D. Dee  
ATTN: R. Plebuch

Utah State University

ATTN: Sec Con Ofc for D. Burt  
ATTN: Sec Con Ofc for K. Baker,  
Dir Atmos & Space Sci  
ATTN: Sec Con Ofc for L. Jensen, Elec Eng Dept  
ATTN: Sec Con Ofc for a. Steed

Visidyne, Inc

ATTN: J. Carpenter  
ATTN: C. Humphrey  
ATTN: W. Reidy  
ATTN: O. Shepard

**END**

**FILMED**

**6-83**

**DTIC**